



AFRL-OSR-VA-TR-2013-0599

**MULTIDISCIPLINARY INVESTIGATION OF UNSTEADY
AERODYNAMICS AND FLIGHT DYNAMICS IN RAPIDLY
MANEUVERING MICRO AIR VEHICLES: THEORY, LABORATORY
AND FLIGHT EXPERIMENTS**

SERGEY SHKARAYEV

UNIVERSITY OF ARIZONA

**11/13/2013
Final Report**

DISTRIBUTION A: Distribution approved for public release.

**AIR FORCE RESEARCH LABORATORY
AF OFFICE OF SCIENTIFIC RESEARCH (AFOSR)/RSA
ARLINGTON, VIRGINIA 22203
AIR FORCE MATERIEL COMMAND**

REPORT DOCUMENTATION PAGE				Form Approved OMB No. 0704-0188	
<p>The public reporting burden for this collection of information is estimated to average 1 hour per response, including the time for reviewing instructions, searching existing data sources, gathering and maintaining the data needed, and completing and reviewing the collection of information. Send comments regarding this burden estimate or any other aspect of this collection of information, including suggestions for reducing the burden, to the Department of Defense, Executive Service Directorate (0704-0188). Respondents should be aware that notwithstanding any other provision of law, no person shall be subject to any penalty for failing to comply with a collection of information if it does not display a currently valid OMB control number.</p> <p>PLEASE DO NOT RETURN YOUR FORM TO THE ABOVE ORGANIZATION.</p>					
1. REPORT DATE (DD-MM-YYYY) 7-11-2013		2. REPORT TYPE Final		3. DATES COVERED (From - To) September 2010 - August 2013	
4. TITLE AND SUBTITLE Multidisciplinary Investigation of Unsteady Aerodynamics and Flight Dynamics in Rapidly Maneuvering Micro Air Vehicles: Theory, Laboratory and Flight Experiments				5a. CONTRACT NUMBER FA9550-10-1-0452	
				5b. GRANT NUMBER	
				5c. PROGRAM ELEMENT NUMBER	
				5d. PROJECT NUMBER	
6. AUTHOR(S) Shkarayev, Sergey				5e. TASK NUMBER	
				5f. WORK UNIT NUMBER	
7. PERFORMING ORGANIZATION NAME(S) AND ADDRESS(ES) University of Arizona 888 N Euclid Ave Tucson AZ 85719				8. PERFORMING ORGANIZATION REPORT NUMBER	
9. SPONSORING/MONITORING AGENCY NAME(S) AND ADDRESS(ES) Air Force Office of Scientific Research 875 N. Randolph St. Room 3112 Arlington VA 22203				10. SPONSOR/MONITOR'S ACRONYM(S) AFOSR	
				11. SPONSOR/MONITOR'S REPORT NUMBER(S)	
12. DISTRIBUTION/AVAILABILITY STATEMENT Distribution Unlimited					
13. SUPPLEMENTARY NOTES					
14. ABSTRACT The report summarizes wind tunnel studies of flapping wings of locusts and several artificial wings. The stroke-averaged lift and horizontal force are measured in a wind tunnel at an angle of attack varying from horizontal to hovering positions. It is found that for high angles of attack, flapping wings do not exhibit the typical abrupt stall seen with fixed wings. Based on high-speed video data, a theoretical analysis of the flapping wings is performed using the discrete vortex method. It is found that the inertial component is dominant in the normal force coefficient in the studied problem. A normal component of the acceleration of the wing's trailing edge is introduced as a kinematic parameter. The report also focuses on transition performance of fixed-wing aircraft with vertical takeoff and landing capabilities. Obtained results show that rapid-pitching efficiency curves converge on steady efficiency curves. From 30 to 70 degrees, efficiency is virtually independent of pitching-rate, throttle-setting, and elevator deflection.					
15. SUBJECT TERMS Unmanned Aerial Vehicles, Unsteady Aerodynamics, Flapping Wings, Wing-Propeller Interactions					
16. SECURITY CLASSIFICATION OF:			17. LIMITATION OF ABSTRACT UU	18. NUMBER OF PAGES 135	19a. NAME OF RESPONSIBLE PERSON Sergey Shkarayev
a. REPORT U	b. ABSTRACT U	c. THIS PAGE U			19b. TELEPHONE NUMBER (Include area code) (520) 954-0441

Reset

Standard Form 298 (Rev. 8/98)
Prescribed by ANSI Std. Z39.18
Adobe Professional 7.0

Table of Contents

1. Introduction.....	3
2. Modeling of Kinematics and Aerodynamics of Flapping Wings	8
2.1. Aerodynamics of Flapping Wings	11
2.2. Experimental Models and Methods	15
2.3. Kinematics Results and Discussions.....	21
2.4. Computational Modeling of Airflow around Flapping Wings	36
2.5. Summary and References to Chapter 2.....	58
3. Insect-Inspired Micro Air Vehciles	63
3.1. Aerodynamics of Flapping-Wing Micro Air Vehicles and Insects	65
3.2. Experimentation.....	75
3.3. Ornithopter Design and Specifications	89
3.4. Summary and References to Chapter 3.....	93
4. Longitudinal Aerodynamics of Rapidly-Pitching Fixed-Wing Micro Air Vehicles	99
4.1. Micro Air Vehicles with Vertical Takeoff and Landing Capabilities	101
4.2. Models and Experimental Apparatus.....	105
4.3. Steady Results.....	108
4.4. Unsteady Procedure and Processing	111
4.5. Unsteady Results.....	120
4.5.1. Wing Lift and Drag Coefficients	122
4.5.2. Wing Moment Coefficients.....	129
4.6. Summary and References to Chapter 4.....	132

1. Introduction

Unmanned aerial vehicles (UAVs) and, in particular, micro aerial vehicles (MAVs) will require extraordinary maneuvering capabilities that are impossible with traditional design methods. These high-rate maneuvers result in highly complex time-dependent topology of the airflow. Therefore, research studies of aerodynamics under high rate translations and rotations of wing-like structures are important and relevant to any vehicle configuration with either fixed, flapping, or rotary wings.

Major Research Activities and Findings

A multidisciplinary approach utilized in the present studies involved the development of experimental facilities and techniques and conducting laboratory experiments and flight tests. The low-speed wind tunnel was designed and constructed in the Department of Aerospace and Mechanical Engineering. The wind tunnel is a closed loop and has an open test section capable of airspeeds up to 20 m/s and is controlled with a variable frequency drive. A five-axis ST Robotics R-12 robotic arm, mounted in the test section, is capable of controlling the experimental subject for pitching maneuvers. Two high-speed video cameras (Phantom 9.1) were installed in the wind tunnel. A custom six-component micro balance was developed with a resolution of 2 mg. These facilities and techniques were applied to studies of unsteady aerodynamic effects in rapidly maneuvering fixed wings subjected to propeller slipstream, in wings of locusts and flapping-wing models.

In Chapter 2, data of a series of wind tunnel experiments on the 25-cm- and 74-cm-wingspan flapping models are discussed. The stroke-averaged lift and horizontal force were measured at an angle of attack that varied from 0 degrees (horizontal) to 90 degrees (hovering position). The flapping frequency was held constant and freestream velocity was varied with the advance ratio

range 0-1.2. It was found that for high angles of attack, flapping wings do not exhibit a typical abrupt stall seen with fixed wings. This feature in flapping wings allows a smooth transition from a level flight to hovering, and back.

Utilizing high-speed videography, data were obtained on the 25-cm model for time-varying flapping angles, pitching angle, and front spar and camber deformations. It was found that the pitching angle exhibits a significant second harmonic and lags the flapping angle. The pitching angle amplitude increases toward the wing's tip. This twisting tendency is analogous to the washout in conventional wings and propellers. Unlike continuous functions of a flapping angle, the pitching angle and spar deformation, the camber function alternates between two well-separated camber values as the membrane snaps. It suggests that the mechanics of membrane deformations during a flapping cycle is analogous to a buckling of a bistable structure from one stable equilibrium position to another.

The solution to the three-dimensional fluid dynamics problem is constructed using two-dimensional solutions obtained for several sections of the wing by the discrete vortex method. It was found that the inertial component is dominant in the normal force coefficient, and hence, the inertia of airflow accelerated by the moving airfoil section is the main mechanism in the production of aerodynamic force in the studied problem. Contributions of both circulatory and vortical components are small and negative. Based on these observations, a normal component of the acceleration of the wing's trailing edge taken with a negative sign is introduced as a kinematic parameter that is essential in flapping wings aerodynamics. This parameter is suitable when a membrane rotates about the leading edge spar. Analysis also shows that synchronization of normal acceleration and pitching angle is important for achieving maximum values of vertical force coefficients.

Chapter 3 presents an insect-inspired design of micro aerial vehicles. Locusts were selected as the basis for this study because they are the appropriate size, they fly efficiently, and they migrate long distances. The particular locust selected for experimentation in this study was *Schistocerca americana*. High-speed videography was used to kinematically point-track their wings while tethered in still air. Simultaneous thrust and lift forces were acquired using a 6-component microbalance. Hindwing retraction increases the proximity of the left-and-right hindwings at the top of the upstroke, enabling aerodynamic lift enhancement via the clap and fling mechanism.

The fully-deployed hindwings of *Schistocerca americana* were used as the basis for designing three artificial wings with approximately the same size, sweep, planform shape, and structure. Since chordwise deformation is critical to flapping-only thrust generation the three investigated artificial wings had varying chordwise stiffness and spanwise stiffness kept approximately constant. A relatively stiff leading-edge spar was used for artificial wing construction.

Aerodynamic forces were measured for three artificial wings using the flapping transmission installed on the microbalance. All wings generate a much smaller amount of lift than thrust, which is similar to what was observed for the live tethered locust. Results confirm that chordwise flexibility has a significant effect on the thrust-generating capability of flapping wings. Thrust performance improves significantly as chordwise-flexibility increases, but excessive chordwise-flexibility may diminish thrust at higher frequencies.

Wing-actuation and chordwise-stiffness studies informed the design of a radio-controlled ornithopter with a flapping transmission and a 14 cm wingspan. Specifically, membrane-batten wings were built with a relatively stiff leading-edge spar and radially-oriented membrane-

supporting spars. The wings flap at a frequency of 20-23 Hz during sustained flight at moderate throttle settings. The ornithopter has demonstrated an ability to withstand moderate winds; it has a mass of 8 grams, an endurance in excess of two minutes and a cruise speed of approximately 3 m/s.

The study described in Chapter 4 was conducted to improve the transition-performance of fixed-wing vertical takeoff-and-landing (VTOL) aircraft. Nose-up pitching delays stall and increases maximum lift coefficient, while nose-down pitching hastens stall and reduces maximum lift coefficient. The relationship between lift and pitching-rate seems simpler to empirical model when the slipstream is present. Generally, positive pitching seems to increase lift coefficient throughout the transition maneuver, while negative pitching reduces it. Both stall and lift-coefficient are affected by pitching regardless of throttle-setting or elevator deflection, but pitching effects are most salient when the throttle-setting is low (weak slipstream) and the pitching-rate is high (rapid-pitching).

The slipstream also seems to simplify empirical aerodynamic modeling for drag curves. It can be generally stated that higher pitching-rate (positive) results in higher drag over the tested domain. The response of lift and drag to rapid-pitching produces very interesting wing efficiency behavior. Rapid-pitching efficiency curves converge on steady efficiency curves near 30 degrees angle of attack. From 30 to 70 degrees efficiency is virtually independent of pitching-rate, throttle-setting and elevator deflection. At lower angle of attack (near 20 degrees) efficiency curves diverge.

Finally, free-flight tests of several MAVs were performed at the Wright-Patterson Air Force Base, in the Micro Air Vehicle Integration and Application Research Institute (μ AVIARI) laboratory in 2011-2012.

The results of the study presented in this report have been disseminated via a book chapter, 8 papers in archival journals, and 11 conference papers.

Training and Mentoring Provided by the Project

Research studies of the project and developments of UAV technology based on the results of the investigations were presented in three MS theses (Gunjan Mania, Garrett Lim, Lee Wilson). Postdoctoral research associate, Dr. Kumar, whom I was mentoring, was productively involved in this project.

This project also contributes to undergraduate research education through the University of Arizona Micro Air Vehicles Club (<http://clubs.asua.arizona.edu/~mavclub/>). The MAV Club is devoted to researching, designing, and fabricating micro air vehicles. Students showcase their progress and developments through competitions worldwide. In 2012, the UA club won a major award in the International Micro Air Vehicles Competition in Germany.

Outreach Activities

Local TV channel KVOA Tucson telecast an interview of the research group on February 23, 2011, that also featured the flapping pitching mechanism developed in this project. They telecast a brief program titled “Micro machines to help secure border” featuring aerial vehicles associated with this project.

An article describing the project and titled “UA Micro Aircraft is Inspired by Nature” was published in *The Green Valley News* on January 9, 2012.

2. Modeling of Kinematics and Aerodynamics of Flapping Wings

In this chapter, the high-speed videography is utilized in measuring kinematic and deformation parameters of the flapping wing. Using these data, a theoretical analysis of the underlying physics is performed using computational fluid dynamics simulations. This chapter is based on the article entitled “Experimental and Computational Modeling of the Kinematics and Aerodynamics of Membrane Flapping Wings,” by Shkarayev, S., Maniar, G., and Shekhovtsov, A. V. and accepted for publication in the Journal of Aircraft.

Nomenclature

A-E	=	marked points on flapping wing model
a	=	dimensionless normal component of the acceleration of the wing's trailing edge taken with negative sign
b	=	horizontal distance between hinges
C_n	=	normal force coefficient of 2D flat wing
C_p	=	pressure coefficient
ΔC_p	=	pressure differential coefficient
C_x	=	horizontal force coefficient of 2D wing section in xyz -frame
C_X	=	horizontal force coefficient of 3D wing
C_y	=	vertical force coefficient of 2D wing section in xyz -frame
C_Y	=	vertical force coefficient of 3D wing
c	=	chord length
d	=	vertical distance between hinges

e	=	length of connecting rod
f	=	flapping frequency
\mathbf{g}	=	density of vortex layer
H	=	joint between crank and connecting rod
h	=	camber
l	=	distance from pivot to marked point
l_a	=	length of wing arm
M	=	torque
m	=	number of strokes
n	=	motor speed
P	=	point on wing's trailing edge
Re	=	Reynolds number, $Re = V_C c / \nu$
\mathbf{r}	=	position vector
\mathbf{r}_0	=	position vector of discrete vortex
S	=	wing surface
s	=	length of crank
T	=	full stroke period
T_D	=	downstroke period
$\overline{T_D}$	=	downstroke duration, $\overline{T_D} = T_D / T$
t	=	time
U	=	flow velocity
\mathbf{V}	=	freestream velocity vector

V_c	=	characteristic velocity
X	=	horizontal component of stroke-averaged aerodynamic force
Y	=	vertical component of stroke-averaged aerodynamic force
xyz	=	ground-fixed coordinate system
$x_{\phi_j} y_{\phi_j} z_{\phi_j}$	=	coordinate system rotating with front spar
α	=	angle between undisturbed relative velocity of air and chordline of 2D airfoil section
α_w	=	angle of attack of wing (defined as angle between wind tunnel flow direction and flapping axis of wing)
β_j	=	pitching angle, defined as angle between chordline and $x_{\phi_j} y_{\phi_j}$ - plane
Φ	=	flapping amplitude
ϕ_j	=	flapping angle
Γ_0	=	circulation of discrete vortex at the moment of its arising
γ	=	angle between section line and spar
ν	=	kinematic viscosity
ρ	=	air density
σ	=	vortex layer
ω	=	angular frequency
ξ	=	coordinate axis along chord line

2.1. Aerodynamics of Flapping Wings

Flapping-wing Micro Air Vehicles (MAVs) have the unique low-speed flight capabilities necessary to be effective in restrictive operational environments. The University of Arizona has developed a family of electric-motor-powered, radio-controlled vehicles with membrane flapping wings sizing from 15 to 25 cm. With a flapping frequency of 25-30 Hz, they can sustain flight for more than 3 min at a speed from 1 m/sec to 5 m/sec.

The aerodynamics of membrane flapping wings is complex and inherently affected by variations in wing geometry. On the other hand, kinematics and deformations defining a wing's geometry are affected by aerodynamic and inertia forces. Kinematic parameters of flapping wings include flapping angle, pitching angle, spars, and camber deformations. Variations in flapping wing kinematics and their aerodynamic consequences are investigated in the present study.

Modern high-speed, high-resolution video cameras, lasers, and motion measuring systems have been used extensively to investigate the kinematics of flapping wings in live creatures and mechanical models. There are distinct differences among the techniques, their hardware components, reconstruction of algorithms, and accuracy. In this introduction, we analyze how these methods and techniques are applied to studies of flapping wing deformations.

A method utilizing patterns of laser lines projected onto a flying object has been developed [2.1, 2.2]. Images of distorted patterns are recorded by a high-speed camera, and the wing's kinematic parameters are reconstructed from these images.

This method was applied to measuring the flapping angle, pitching angle, and wing deformations in tethered bumblebees simulating a hovering flight [2.1]. An uncertainty of 0.6

mm was reported, corresponding to an accuracy of 2%. The amplitudes of the flapping angle and the pitching angle were about 120° and 180° , respectively.

In another study [2.2], free-flying dragonflies were recorded by the projected lines method and utilizing natural landmarks on the insects' wings. A number of parameters were measured: body trajectory and attitude (yaw, roll, and pitch angles), flapping wing kinematics (flapping angle, pitching angle, and camber deformations). Two flights were analyzed: a forward flight and a turn in the horizontal plane. During the turn, the body also rolled toward the direction of the maneuver, with forewings moving asymmetrically. Amplitudes of both flapping and pitching angle decreased for inner forewings and increased for outer forewings. In contrast to the forward flight, during the turn the camber deformations of forewings remained positive during the beating cycle. No spanwise twist deformations were determined in [2.1, 2.2].

Methods of high-speed video recording and photogrammetric reconstructions are widely used for problems related to flapping flight [2.3-2.6]. They are known as direct linear transformation methods (DLT) and are based on the central perspective projections. Some details of the methods follow.

Experimental hardware in these methods includes two or more high-speed video cameras and a computer. Camera calibration is performed using a set of 3D coordinates, providing relationships between orientation parameters of an image plane and an object space. Prior to the recording, markers are placed on the object. Natural features of the object can also be used for this purpose. After images are recorded, markers are tracked and digitized in order to determine their positions in 2D image planes. Using these data jointly with calibration parameters and applying central perspective projection equations, 3D coordinates of markers and relevant geometrical quantities about the object are obtained.

In studies [2.5, 2.6], the DLT method was modified with a bundle adjustment procedure, resulting in a very high accuracy of measurements. The method was applied to investigations the kinematics of flapping wings in tethered locusts and freely-flying hoverflies. More than 100 markers per wing were reconstructed. The mean value of the measurement error was 0.11 mm for the locusts and 0.03 mm for the hoverflies.

These studies [2.5, 2.6] found that twist and camber deformations play an important part in the motion of flapping wings and are attributed to elastic deformations of the wing structure. The amplitude of the twist in the hindwings and forewings of locusts was about 40° and 30° , respectively. Except for a short period of time on the upstroke, the hindwings showed a positive camber, with a maximum of 10%. Forewings were positively cambered during the entire stroke. In hoverflies, the camber remained positive, reaching a maximum value of 12%.

The aerodynamic consequences of the twist and camber deformations [2.5, 2.6] were analyzed in [2.7] using computational fluid dynamics simulations with the FluentTM software. The results of these simulations show better aerodynamic power efficiency in flapping wings with time-varying camber and twist. Implications of these results are important for designing micro aerial vehicles, suggesting aeroelastic tailoring to the flapping wing structure.

There have been several studies of the aerodynamics of mechanical models of flapping wings. Ho et al. [2.8] used a single degree-of-freedom rotation mechanism to flap membrane wings made with different batten reinforcements. They found that thrust production heavily depends on stiffener patterns.

Singh and Chopra [2.9] developed a flapping wing device with articulated flapping and pitching rotations in the wing base. They showed that wings with larger pitch variations showed better thrust production, concluding that the flexibility of the wing plays a key role in the

aerodynamic performance of flapping wings. An aeroelastic analysis method was developed and applied to experiments. Computations confirmed the force peak at the beginning of each half-stroke observed in the experiments, and the peak was attributed to non-circulatory forces.

One particularly interesting project was undertaken by Wu et al. [2.10, 2.11]. They developed a digital image correlation method for tracking the motion of membrane flapping wings. The wing shape data were acquired using low-speed stereo cameras triggered by a strobe light. A force-and-torque load cell was used to measure instantaneous forces produced by the flapping action of the wings. This method was applied [2.11] to study the kinematics and aerodynamics in wings with four reinforcement layouts. A strong correlation was found between the thrust and parameters of the wing-tip deformation phase loops.

In our previous studies [2.12-2.14], a series of wind tunnel experiments was conducted on a 25-cm flapping wing model. The stroke-averaged lift and horizontal force was measured at an angle of attack that varied from 0 (horizontal) to 90° (hovering position). The flapping frequency was held constant and freestream velocity was varied with the advance ratio range of 0-1.2.

At no-freestream conditions, the thrust coefficient changed nonlinearly with flapping frequency, showing a maximum in its function. With a freestream present at high angles of attack, the flapping wings did not exhibit the typical abrupt stall seen with fixed wings. Furthermore, with the freestream normal to the flapping axis, the vertical force component was greater than the force generated at no-freestream conditions. The results suggested that additional investigations were in order to explain these effects.

In the present study, a multidisciplinary study of the kinematics and aerodynamics of membrane flapping wings is presented. The developed approach is comprised of high-speed videography, aerodynamic force measurements, and computational fluid dynamics simulations.

The effects of flapping frequency and freestream velocity on time variations of kinematic parameters, deformations, and aerodynamic forces in flapping wings are investigated. Computational modeling is performed to uncover significant features in aerodynamic forces and airflow structure. Correlations between kinematic and aerodynamic parameters are found and discussed.

2.2. Experimental Models and Methods

The experimental setup includes a 25-cm membrane battened wing (Fig. 1), mounting rib, and a flapping transmission with motor. A schematic of the wing is shown in Fig. 2. Its structure consists of a front spar, 4 battens, and a membrane. The membrane is 0.015-mm Mylar bonded to the spar and to the battens with rubber cement. Pultruded carbon rods are used: T315-4 of diameter 0.8 mm for the front spar. Battens are made of 0.5-mm-diameter steel wires. Battens are not rigidly fixed to the front spar, allowing pitching deformations of the membrane with battens during a flapping cycle. Geometrical and mass specifications of the wing model are presented in Table 1.

Black ink marks (2 mm in diameter) are evenly placed on the wing's surface along 4 sections of the half-wing (Sections 1-4). There are 5 marked points per section, as can be seen in Fig. 1. Marked point A is at the pivot of the wing, point B is at the hinge attaching the wing to the connecting rod (see also Fig. 4), and point C is at the wing tip. Points E_1 and E_3 are at intersections of the batten and spar lines. Marked points 2-5 are evenly spaced along each section, with point 5 on the trailing edge.

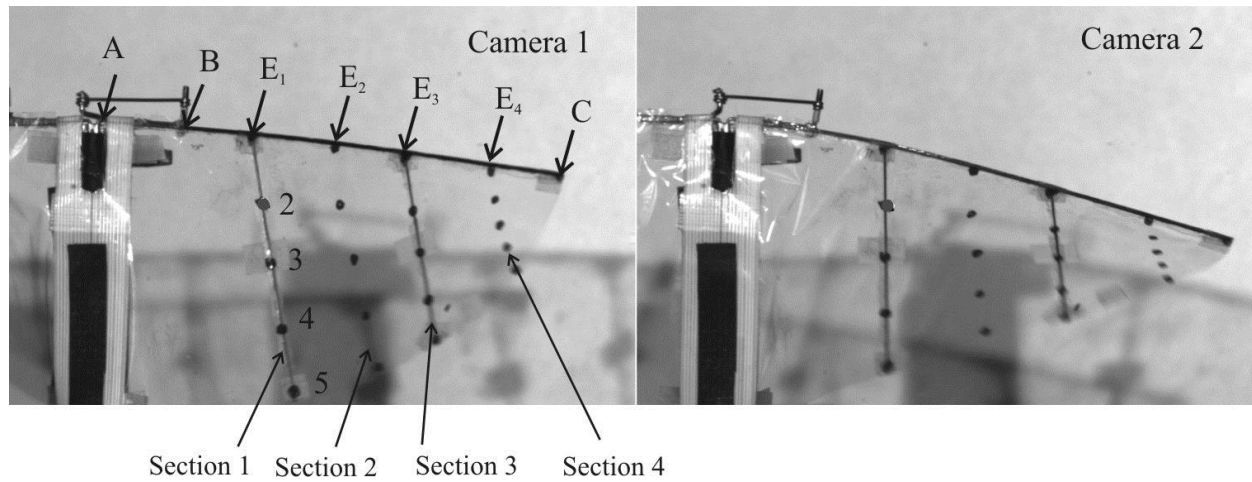


Fig. 1 Photos of wing taken by two cameras.

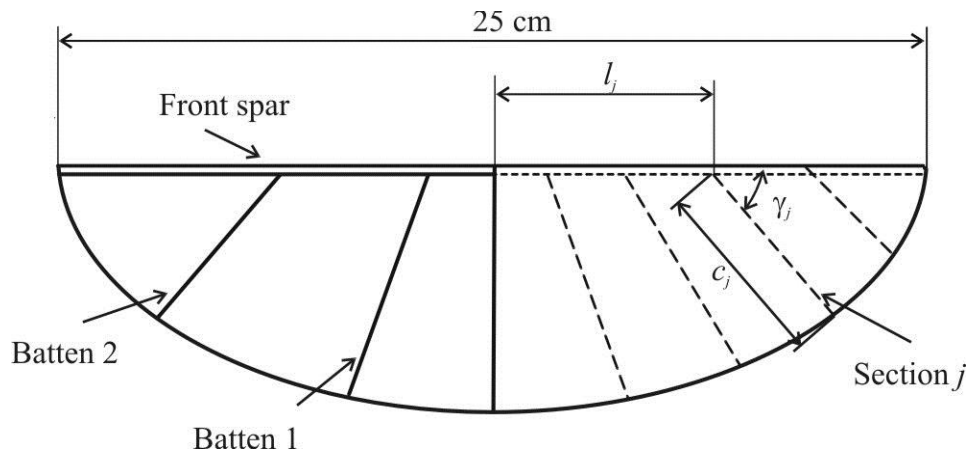
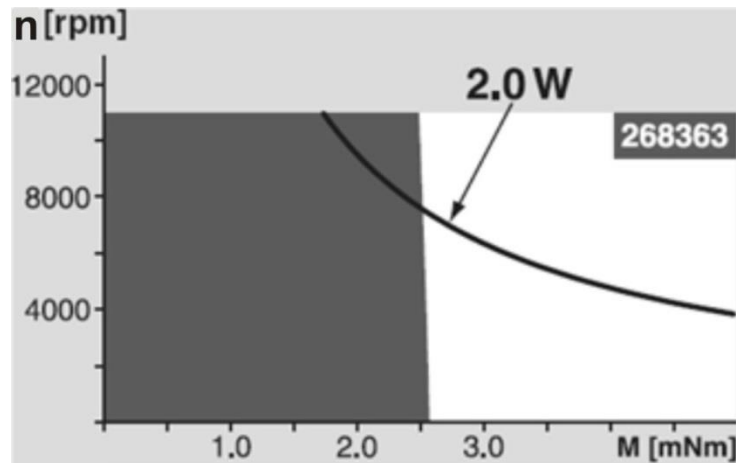


Fig. 2 Membrane flapping wing schematics.

Table 1 Specifications of flapping wing model.

Wingspan, cm	25
Wing area, cm ²	137
Aspect ratio	4.5
Root chord, $l_0 \times c_0 \times \gamma_0$, cm×cm×deg	0.0×7.0×90
Section 1, $l_1 \times c_1 \times \gamma_1$, cm×cm×deg	3.8×6.5×75
Section 2, $l_2 \times c_2 \times \gamma_2$, cm×cm×deg	5.7×5.9×75
Section 3, $l_3 \times c_3 \times \gamma_3$, cm×cm×deg	8.0×4.8×60
Section 4, $l_4 \times c_4 \times \gamma_4$, cm×cm×deg	10×2.6×60
Wingtip deflection, cm/g	0.18
Mass, g	1.15

The initial rotation of a flapping wing is generated by a motor via the custom-designed flapping transmission. A Maxon RE-13 electric motor [2.15] is connected to the transmission through an 8:1 gearbox. Figure 3 is an operating range plot for this motor in terms of speed, n , and torque, M . It can be seen that for a constant power input, the torque on the shaft decreases as n increases.

**Fig. 3 Operating range plot for Maxon RE-13. Adopted from [2.15].**

The wings were tested at a constant flapping frequency. Their motion was recorded by two video cameras (Phantom v7.3 Vision Research) set in front of the model at the distance of 1.3 m. The cameras were synchronized via Visual Image Correlation Snap software (v2.9, Correlated Solutions). This software was also used for acquiring images of moving wings and storing image files in the computer. Images were acquired at a recording frequency (frame rate) of 800-2500 Hz, and the exposure time was set between 300-1000 μ s, based on the requirements of the experiments. Two 250-watt lamps (North Star Lighting) were used to ensure that sufficient lighting was provided to the area being photographed. Acquired image files were compiled into videos using Windows Movie MakerTM software.

Camera calibration was performed using a specially designed calibration plate. The V-shaped plate consists of two planes inclined at 60°, and 36 dots were precisely placed on the plate. Calibration of cameras and tracking of the markers and digitizing their locations were performed using the software [2.4].

High-speed videography was conducted at the University of Florida REEF facility. The REEF wind tunnel is an open-loop, open-section tunnel capable of airspeeds up to 20 m/s. More details of the facility can be found in a paper by Albertani and Babcock [2.16].

A plane four-bar linkage is used as a transmission to convert a uniform continuous rotation of the motor into harmonic oscillations of the wing arm and, consequently, of the wing. This transmission consists of a double crank, OH, connecting rods, HB, and wing arms, AB (Fig. 4). Dimensions of the components are $s=8.5$, $e=32$, $l_a=20$, $b=1$, and $d=25$ (all in mm).

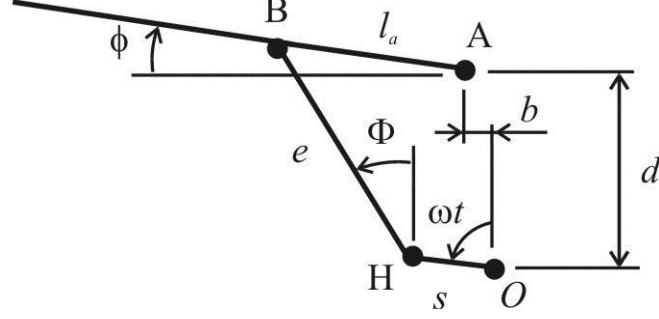
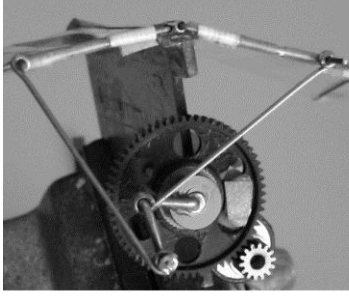


Fig. 4 Flapping transmission.

A position analysis of the four-bar linkage is presented for the constant angular frequency of the crank, $\omega = 2\pi f$, where f is the flapping frequency. Neglecting deformations of the linkage components and gravity effects, and assuming perfect revolute joints, the constraint equations are cast as

$$\begin{aligned} s \sin(\omega t) + e \sin \Phi &= l_a \cos \phi + b \\ s \cos(\omega t) + e \cos \Phi &= l_a \sin \phi + d \end{aligned} \quad (1)$$

and solved numerically, using a Newton-Raphson method and MatlabTM. Numerical results for the flapping angle, ϕ , are presented and discussed in Section IV.

Motion of the flapping wing includes articulated rotations of its base, as well as elastic deformations in the membrane (skin) and rotations and deformations of stiffeners (battens and spars). Since the aerodynamic center of pressure, center of mass, and shear center do not typically coincide in these wings, inertial, elastic, and aerodynamic forces cause wings to bend (spanwise) and twist (chordwise bending).

Conventions used for aerodynamic forces, angles, and deformations are illustrated in Fig. 5. The orientation of a flapping wing model with respect to a freestream is described by the angle of attack of the flapping wing, α_w , which is defined as the angle between the flapping axis (y_{ϕ} -

axis in Fig. 5) and the freestream direction (\mathbf{V} -vector in Fig. 5). The $x_{\phi_j}y_{\phi_j}z_{\phi_j}$ coordinate system is rotating with the wing about the flapping axis, y_{ϕ_j} , with the x_{ϕ_j} -axis passing through the point E_j of the leading edge. Thus, the flapping angle, ϕ_j , is the angle between the x and x_{ϕ_j} axes. It is positive if seen anticlockwise rotation from the tip of the y -axis. The pitching angle, β_j , is between the segment E_jP_j (Sections 1-4) and its projection $E_jP'_j$ onto $x_{\phi_j}y_{\phi_j}$ -plane. The pitching angle is defined positive if viewed anticlockwise rotation from the tip of the x_{ϕ_j} -axis.

In order to investigate camber deformations, out-of-plane deformations of marked points along Sections 1-4 are analyzed (Fig. 1). The ξ -axis is introduced along the chordline of the Section E_jP_j with the point E_j of the leading edge as the origin (Fig. 5). The camber, h , for the marked point k is defined as a distance between this point and the ξ -axis. The camber, h , is positive when $z_{\phi}(k) > z_{\phi}(K)$.

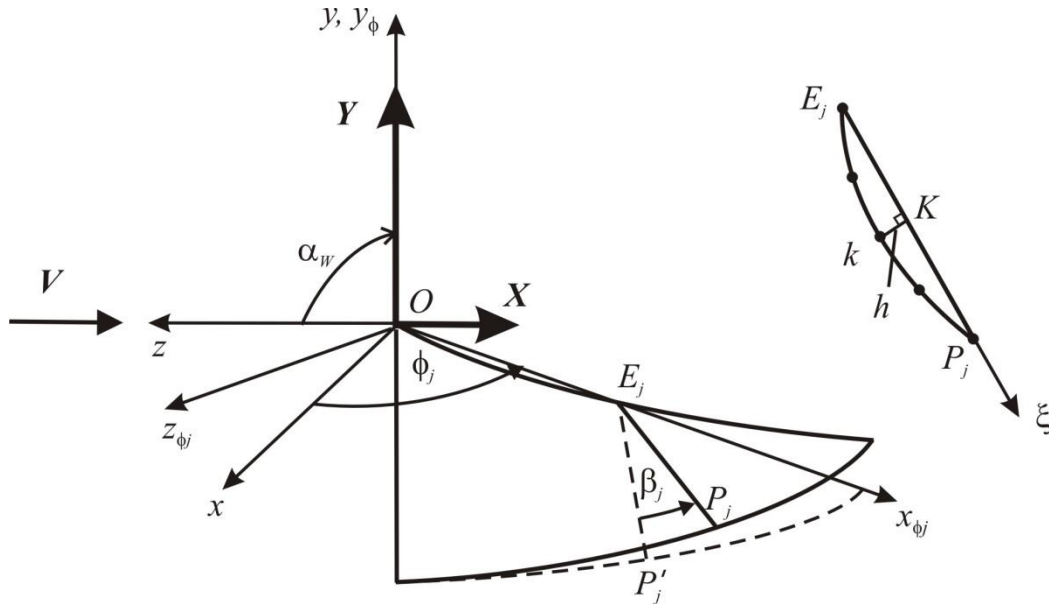


Fig. 5 Conventions for aerodynamic forces, flapping angle, pitching angle, and camber.

Experimental data for angles, displacements, and deformations are approximated using truncated Fourier's series as

$$F(t) = F_0 + \sum_{n=1}^k A_n \cos(n\omega t + \delta_n) \quad (2)$$

Fourier series approximations are constructed using degree of 3 for the flapping angle and marked points displacements, and degree of 6 for the pitching angle.

The terms upstroke and downstroke refer to increased and decreased wing motion in the direction of the flapping angle, respectively. The downstroke duration, $\overline{T_D}$, is defined as the ratio of the downstroke period, T_D , over the full wingbeat period, $T = 1/f$.

2.3. Kinematics Results and Discussions

In order to investigate the accuracy of photogrammetric measurements, a simple model of the front spar without a skin and battens was cut of 1.56 mm diameter carbon rod. The rod was attached to the flapping transmission and ran at a constant flapping frequency of 10 Hz. High-speed recordings were taken at the rate of 1,000 frames per second with no freestream. Using collected data, distances from the root A to points B, C₁-C₄, and E were computed for each frame in the stroke. Nominal values of distances are in the range 20 to 120 mm. The video system is very stable in its reporting of time varying positions. The averaged over time and distances standard deviation of measurement of linear coordinates is 0.26 mm. This measure shows a high spatial and temporal resolution of the method.

A series of tests were conducted on the 25-cm flapping wing at no-freestream conditions. The part of the front spar between points A and B is stiffened with a Z-shaped arm made of steel

wire. It has a high bending stiffness and, therefore, is utilized for the purpose of determining the flapping angle at the root of the wing, ϕ .

Kinematical changes in flexible flapping wings with no-freestream are analyzed for discrete frequencies of 10, 15, and 22 Hz. Data points and Fourier approximations for the flapping angle and the pitching angle for Section 1 at 22 Hz are presented in Figs. 6 and 7, respectively. The curves follow the trend of the experimental data well and the residuals appear to be randomly distributed.

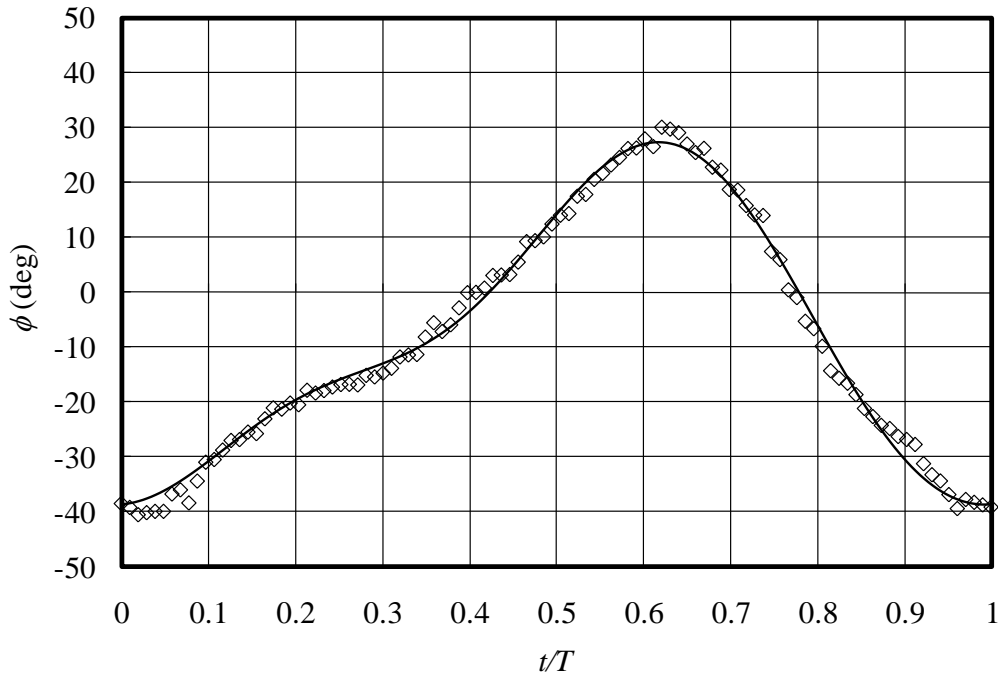


Fig. 6 Flapping angle variation through stroke ($f = 22\text{Hz}$ and $V = 0$).

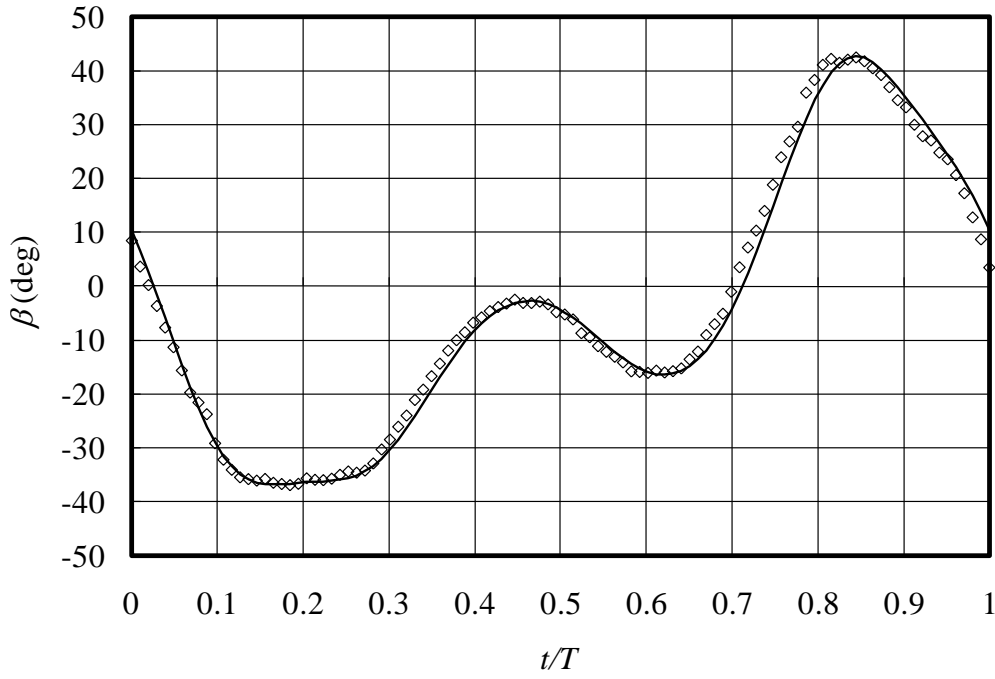


Fig. 7 Pitching angle variation of Section 1 through stroke ($f = 22$ Hz and $V = 0$).

Figure 8 compares numerical results and experimental data for flapping angle versus time. The amplitude of the flapping angle from the solutions of Eqs. (1) is found to be 66° and its maximum occurs at $t/T = 0.58$. These results are representative of perfect revolute joints and do not change with frequency. In experiments, the amplitude of the flapping angle varies as 68° , 71° , and 66° at flapping frequencies of 10, 15, and 22 Hz, respectively. Differences in numerical and experimental flapping amplitudes can be explained by deformations and imperfections in the transmission mechanism. With frequency increase, the maximum flapping angle shifts to the right from $t/T = 0.5$ at $f = 10$ Hz to $t/T = 0.63$ at $f = 22$ Hz. At $f = 22$, Hz the downstroke duration is $\overline{T}_D = 0.37$.

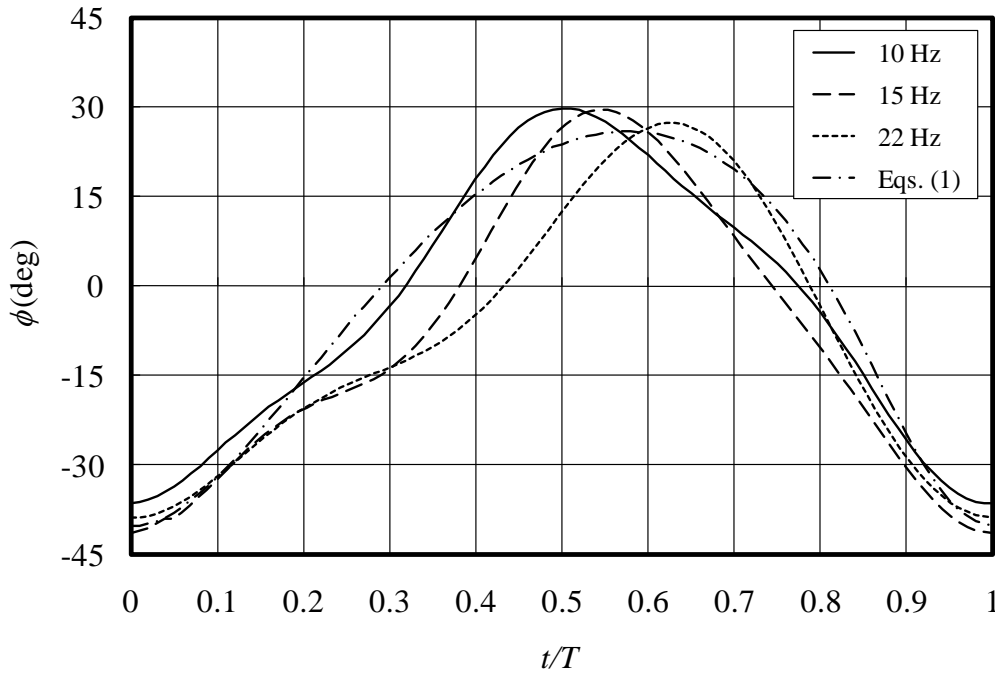


Fig. 8 Time variations of flapping angle for various flapping frequencies ($V = 0$).

Figures 9-11 compare pitching angles for Sections 1-4 at various flapping frequencies. The pitching angles exhibit a significant second harmonic. The amplitudes of the second harmonic are 0.6-0.7 of those of the first harmonic.

Curves for all sections converge near t/T , corresponding approximately to the minima and maxima of the flapping angles. The slopes are highest near these points, suggesting high rotational rates. The inner section (Section 1) has lower pitching angle amplitude than the outer section. The amplitude increases with an increase in the flapping frequency. For Section 3, the amplitudes of the pitching angle are 82° , 109° , and 160° at 10, 15, and 22 Hz, respectively.

The pitching angle lags the flapping angle. The magnitude of the phase lag increases with an increase in flapping frequency and it is greater for the part of the wing closest to the root.

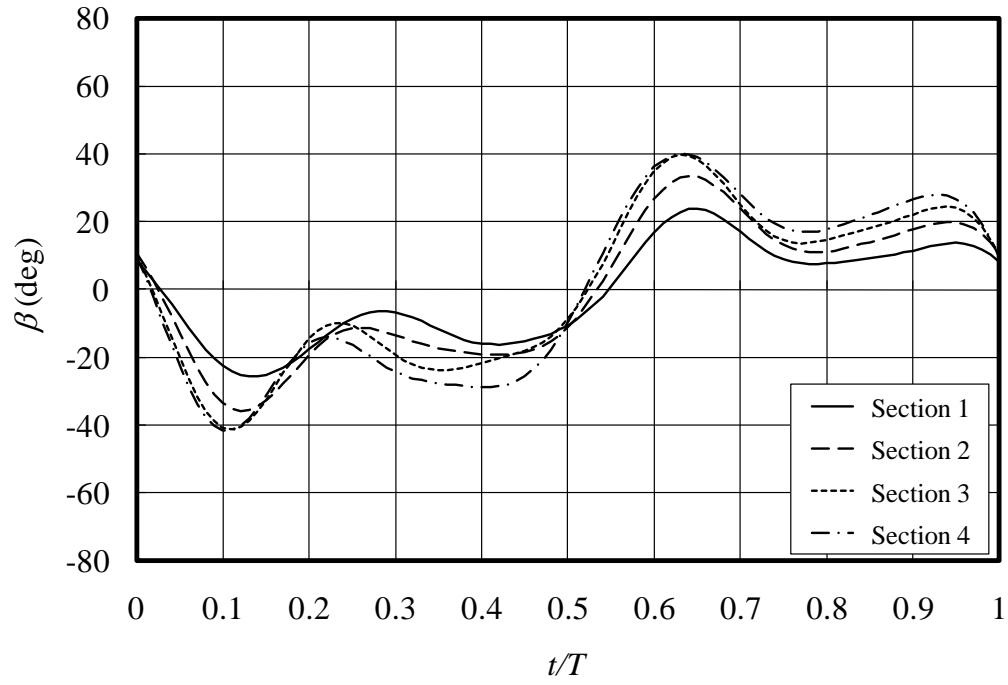


Fig. 9 Time variation of pitching angle at a frequency of 10 Hz.

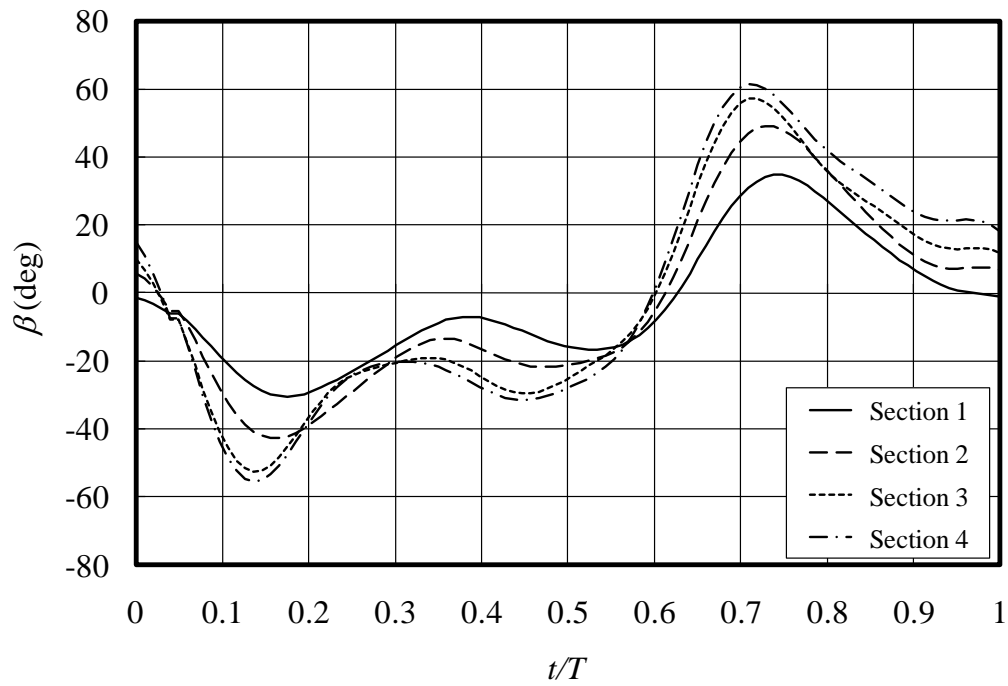


Fig. 10 Time variation of pitching angle at a frequency of 15 Hz.

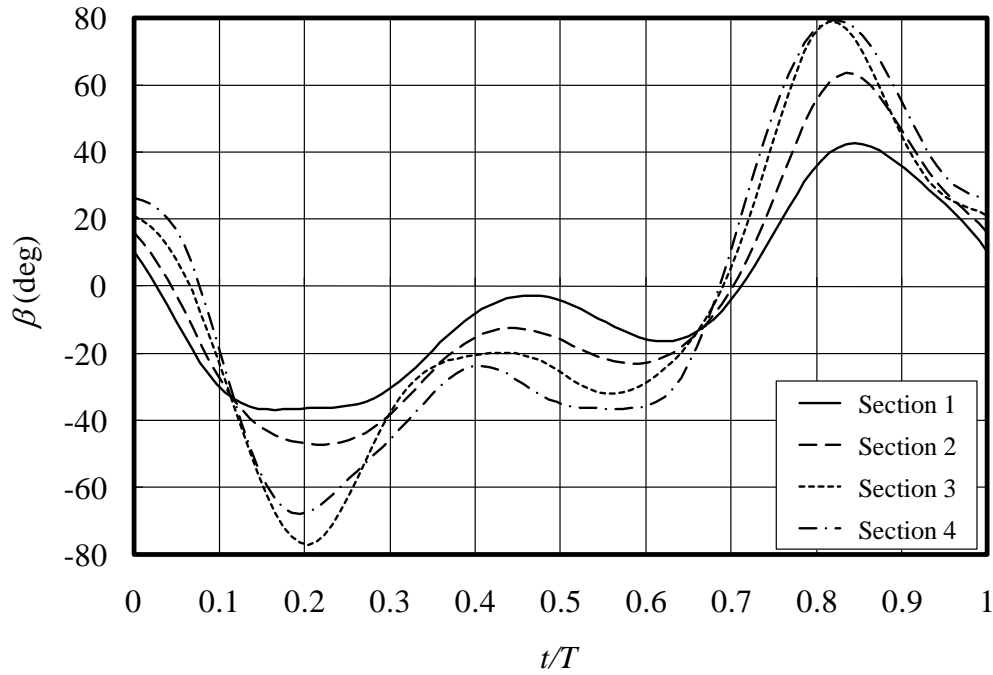


Fig. 11 Time variation of pitching angle at a frequency of 22 Hz.

The spanwise distributions of the pitching angle at different times are presented in Figs. 12 and 13 for the upstroke and downstroke, respectively. Data are obtained at a frequency of 22 Hz. The wing twists outward along the span (magnitude of the pitching angle increases from the root to the tip). This twisting tendency is analogous to the washout in conventional wings and propellers. Spanwise variations of the pitching angle are approximated by linear functions, as shown in Figs. 12 and 13. These approximations are found to be valid with the regression coefficient of $R^2 > 0.82$, with exception of $t/T = 0.1$ and 0.7 , where $R^2 < 0.35$. The proposed linear approximation for the pitching angle will significantly reduce otherwise tedious experimental data post-processing.

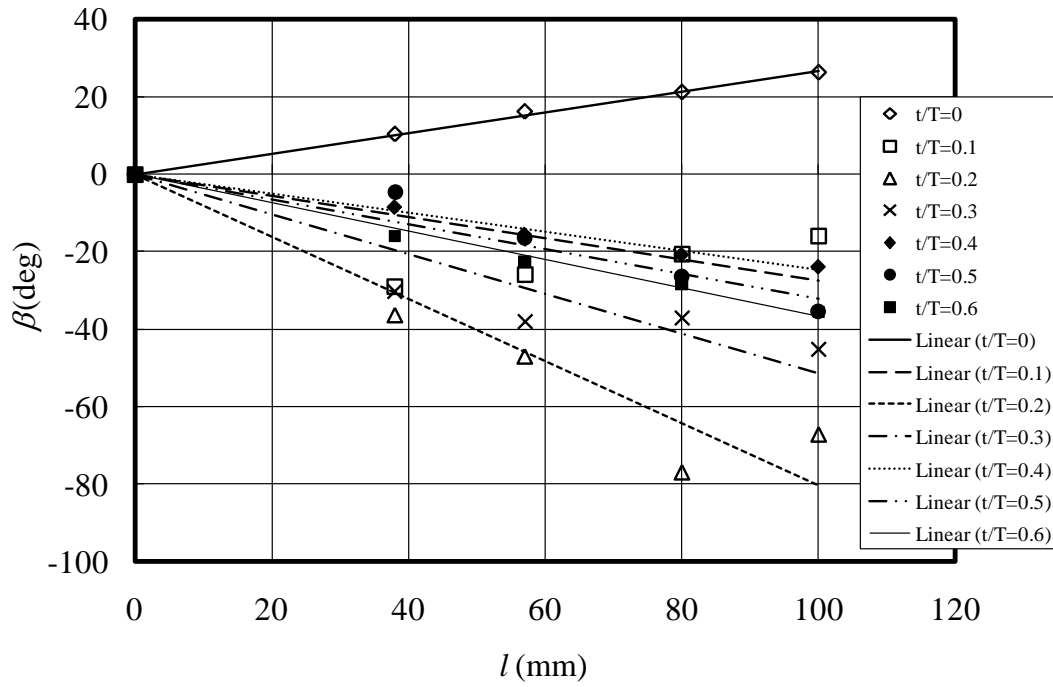


Fig. 12 Spanwise variation of pitching angle on upstroke ($f = 22$ Hz).

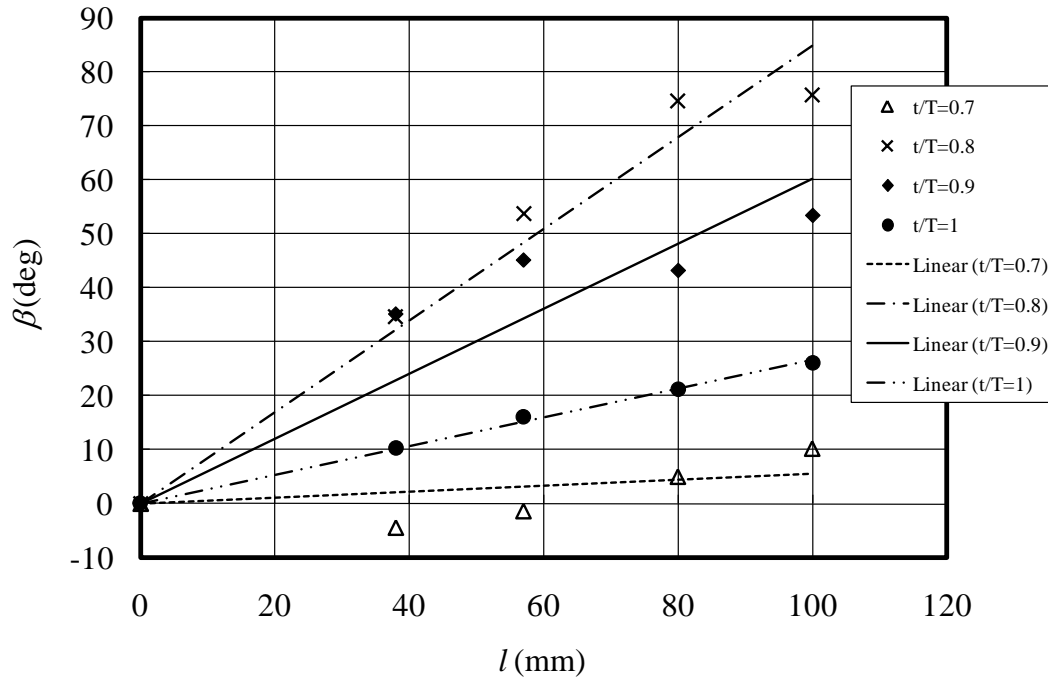


Fig. 13 Spanwise variation of pitching angle on downstroke ($f = 22$ Hz).

Deformations of the front spar out of the wing's plane (z_ϕ -direction) are illustrated in Figs. 14 and 15 for the upstroke and downstroke, respectively. The change in the wing's concavity occurs within 4 milliseconds of the beginning of the upstroke at $t/T=0-0.1$. After that, the spar has a noticeable downward bend, which is maintained throughout the remainder of the upstroke. The next change in concavity occurs at $t/T=0.6-0.7$. For the rest of the downstroke, there is an upward bend. Maximum z_ϕ -deformations of the spar at the wing tip are 0.3 and 0.42 of the wing's length (half of the wingspan) on the upstroke and downstroke, respectively.

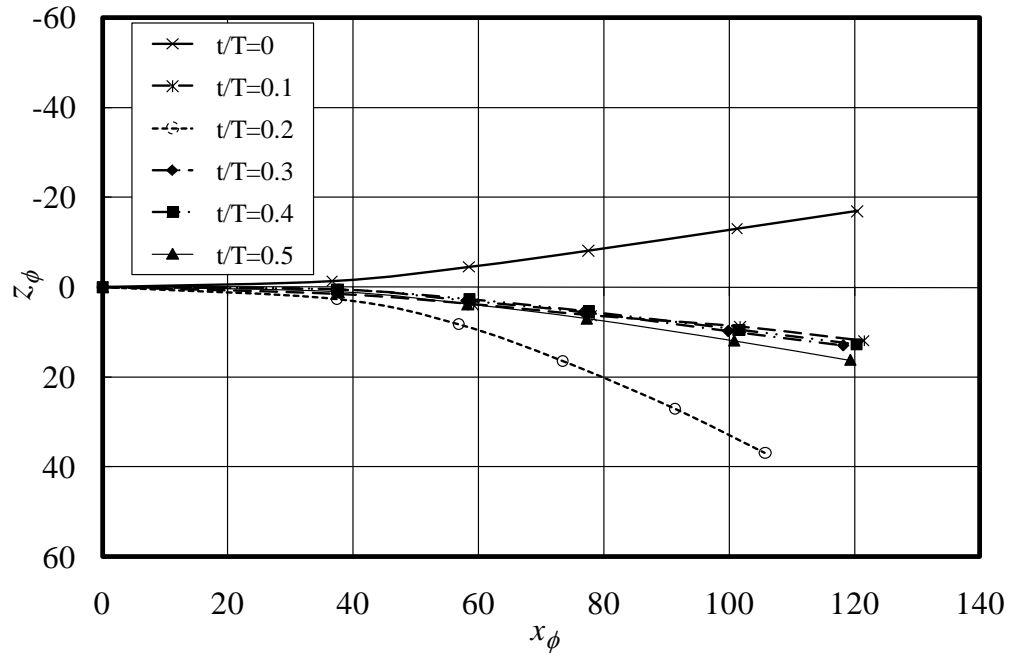


Fig. 14 Spar deformations on upstroke ($f = 22$ Hz).

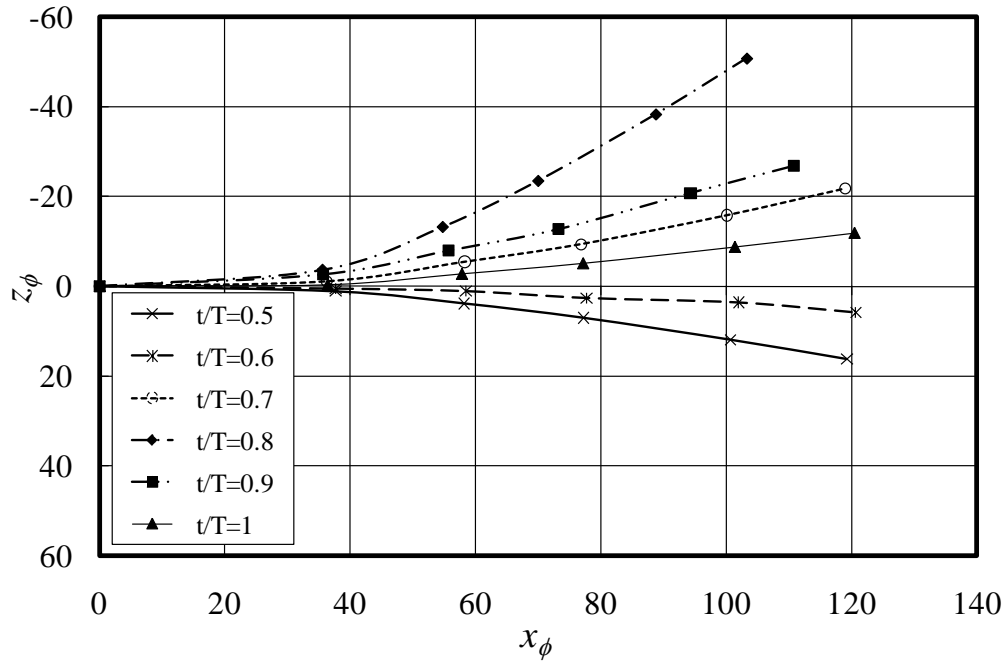


Fig. 15 Spar deformations on downstroke ($f = 22$ Hz).

The spar deforms differently in the wing's plane (y_ϕ -direction). It bends downward, so that $y_\phi < 0$ during the entire stroke. Because the membrane does not support a compressive load, it does not constrain the spar's downward motion, but limits its upward motion. The maximum downward deformation is 0.33 of the wing's length.

Out-of-plane camber deformations are investigated in the present study. Figure 16 shows a time variation of the camber, h/c , at point 2 of Section 2 at $f = 15$ Hz. It can be seen that the positive camber ranges from 2.3% to 3.3% and the negative from -4% to -2.4%. [Remember that Sections 1 and 3 lie on top of battens (Fig. 1), which are rather stiff.] As expected, average cambers for point 2 of Sections 1 and 3 are much smaller: in the range from 0.7% to -0.8%. Thus, the part of the membrane motion between Sections 1 and 3 is constrained by adjacent battens and the front spar.

The variation of the pitching angle, β , with time is also presented in Fig. 16 for the same Section 2. Unlike the continuous function of the pitching angle, the camber function alternates between two well-separated camber values as the membrane snaps. It suggests that the mechanics of membrane deformations during a flapping cycle is analogous to a buckling of a bistable structure from one stable equilibrium position to another.

Figures 17 and 18 show the time-varying deformations of the membrane along Section 2. Clearly, the extrema of the function h/c occur at a distance of 25-35% of the chord from the leading edge. The camber line takes both arc- and S-shapes. An airfoil with a positive camber during the upstroke and a negative one on the downstroke scoops up air, which may improve the wing's aerodynamic performance. With flapping frequency increases up to 22 Hz, the maximum camber increases up to 7%. Overall, positive and negative cambers are distributed almost evenly during a half-stroke, and therefore, their aerodynamic consequences are not clear.

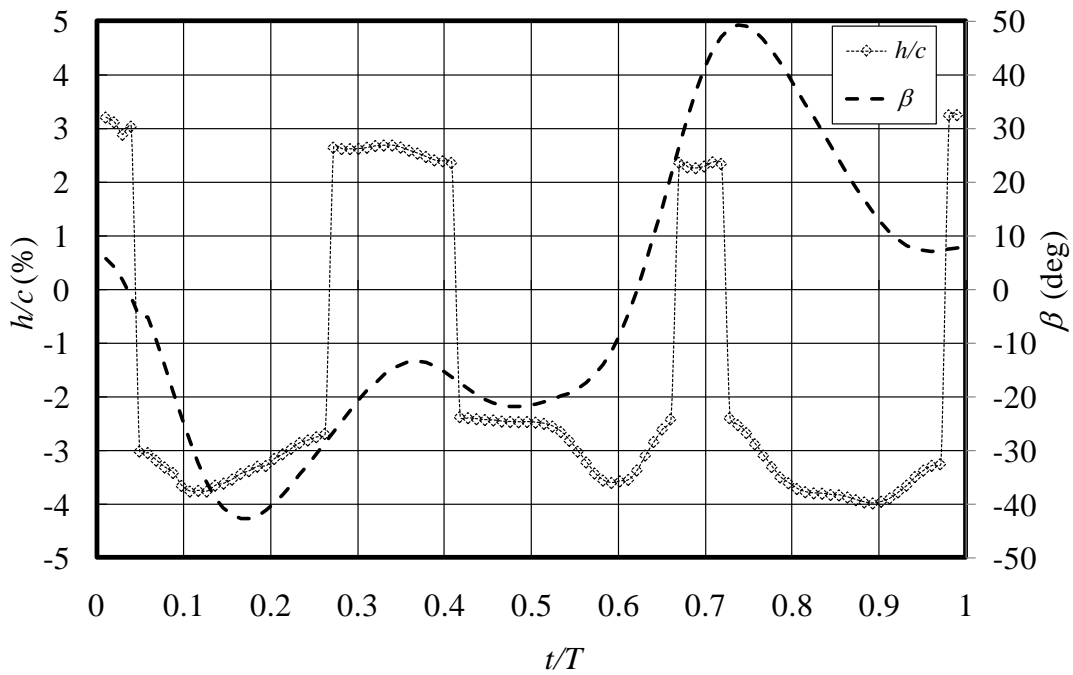


Fig. 16 Time variation of camber in point 2 in Section 2 ($f = 15$ Hz).

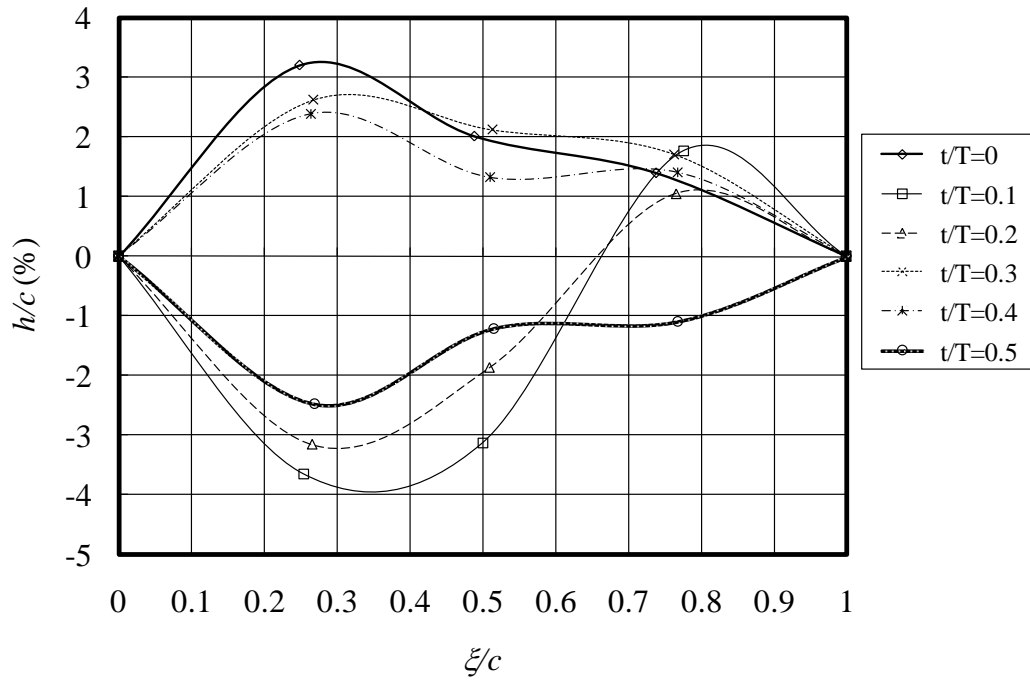


Fig. 17 Camber deformations along Section 2 during upstroke ($f = 15$ Hz).

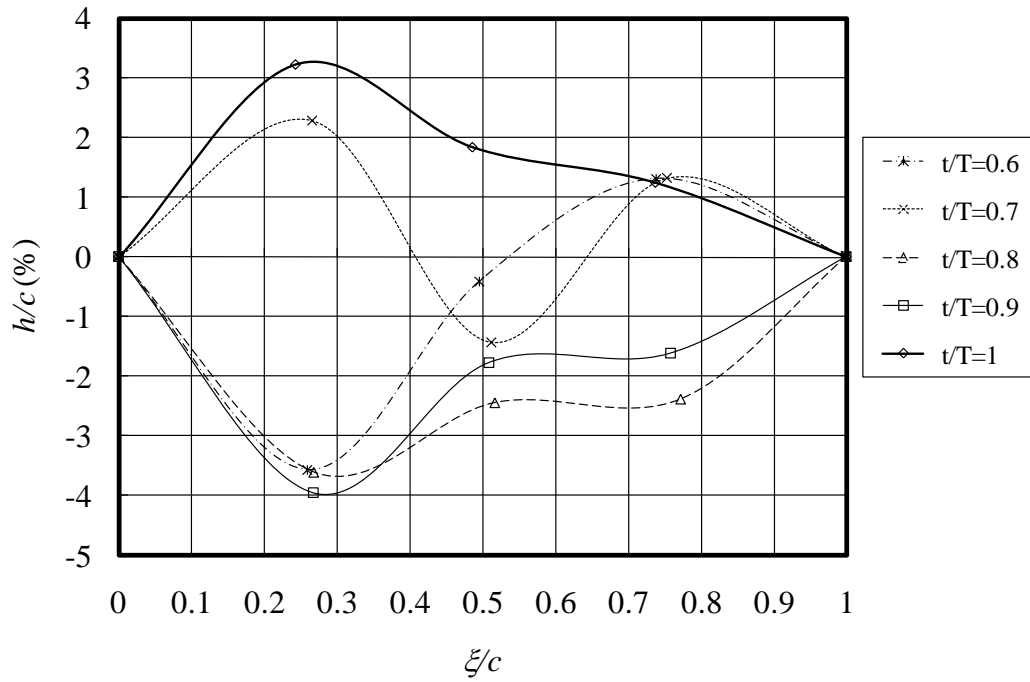


Fig. 18 Camber deformations along Section 2 during downstroke ($f = 15$ Hz).

High-speed videography was conducted in the wind tunnel with the test model installed normal to the airflow direction. Or else, the flapping axis was at 90° to the wind tunnel flow direction, as shown in Fig. 5. Two values of the freestream velocity were tested: 5.5 and 8.3 m/s. Figure 19 presents time variations of the flapping angle at $f = 22$ Hz for three values of freestream velocity. The amplitude of the flapping angle varies as 66° , 67° , and 64° at speed of 0, 5.5 and 8.3 m/s, respectively. Noticeably, with an increase in speed, the maximum of the flapping angle shifts to the left. This changes the downstroke duration $\overline{T_d}$ from 0.37 at $v = 0$ to 0.52 and 0.61 at velocities of 5.5 and 8.3 m/s, respectively. The increase of the downstroke duration plays an important role in enhancing lift performance of the flapping wing apparatus. During upstroke (with the wind), the freestream speed is subtracted from the flapping speed, while on the downstroke (against the wind), the freestream speed is added to the flapping speed. Thus, a greater magnitude of the horizontal component of the stroke-averaged aerodynamic force, x , is expected on the downstroke. With this force increase the electric motor's torque, M , increases and, from Fig. 4, it follows that the angular velocity n decreases on the downstroke. This passive mechanism of the downstroke duration increase was realized with the particular electric motor used. Interestingly, in locusts, the average downstroke duration (about 0.57) is greater than the upstroke duration [2.9]. It is theorized that some kind of passive control of the stroke duration may be in use by animals as well.

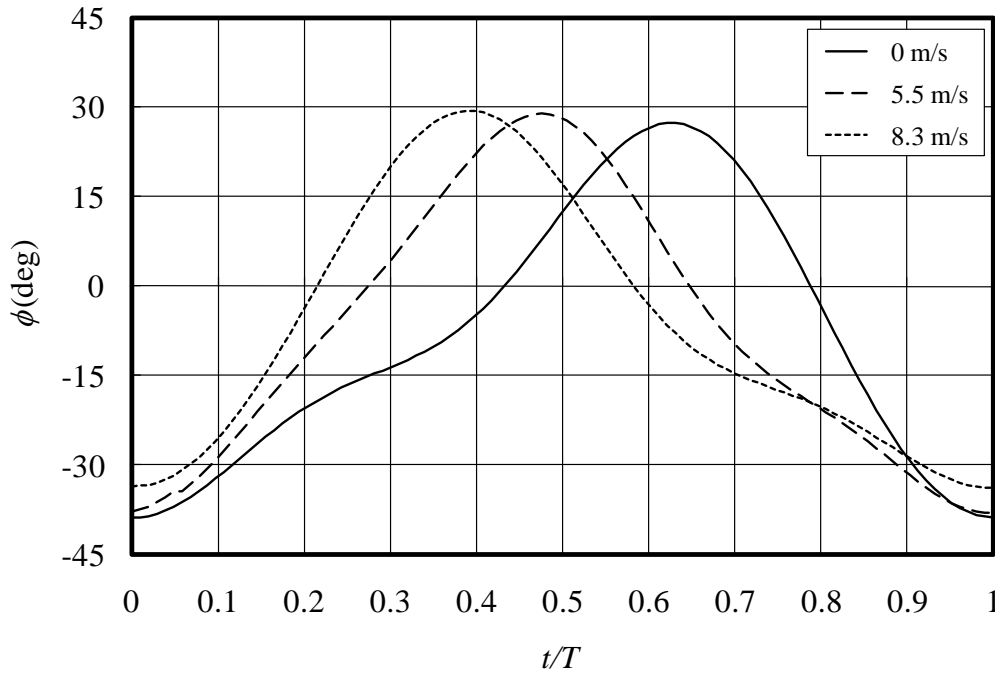


Fig. 19 Time variation of flapping angle for three wind speeds ($f = 22$ Hz).

The pitching angle changes dramatically with a freestream velocity increase from 0 to 5.5 and 8.3 m/s, as seen from Figs. 11, 20, and 21. The maximum values of the pitching angle in the presence of a freestream are slightly smaller than that at zero velocity, but the absolute value of the minimum and, consequently, the amplitude decrease dramatically with an increase in speed. The pitching angle amplitudes for Section 3 decrease from 160° ($V = 0$) to 112° ($V = 5.5$ and 8.3 m/s). As with no-freestream condition, the inner section has lower pitching angle amplitude than the outer section. Approximately linear variations of the pitching angle outward of the wing are confirmed for the nonzero freestream velocity.

With an increase in freestream velocity, the position of β_{\min} relative to the position of ϕ_{\min} ($t/T = 0$) shifts to the right to $t/T = 0.3$. Meanwhile, β_{\max} shifts to the left, maintaining the same relative position to ϕ_{\max} . The kinematics on the upstroke features a shorter duration, overall smaller pitching angle magnitudes, and a smaller relative speed of airflow. On the downstroke, a

longer duration is combined with a greater relative speed. From these observations, a better aerodynamic performance during downstroke is predicted.

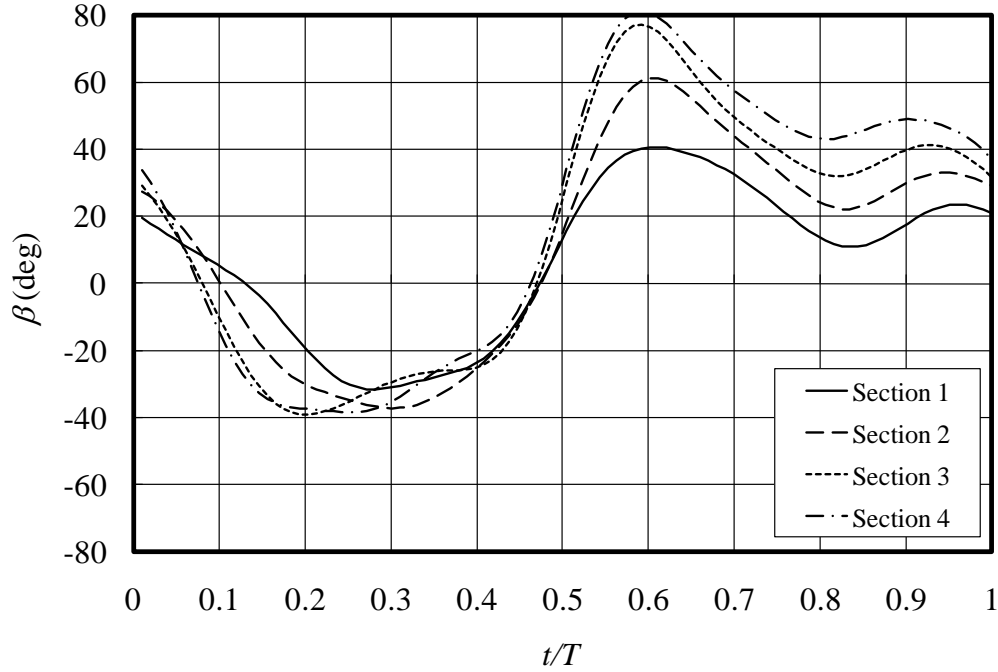


Fig. 20 Time variation of pitching angle ($f = 22$ Hz, $V = 5.5$ m/s).

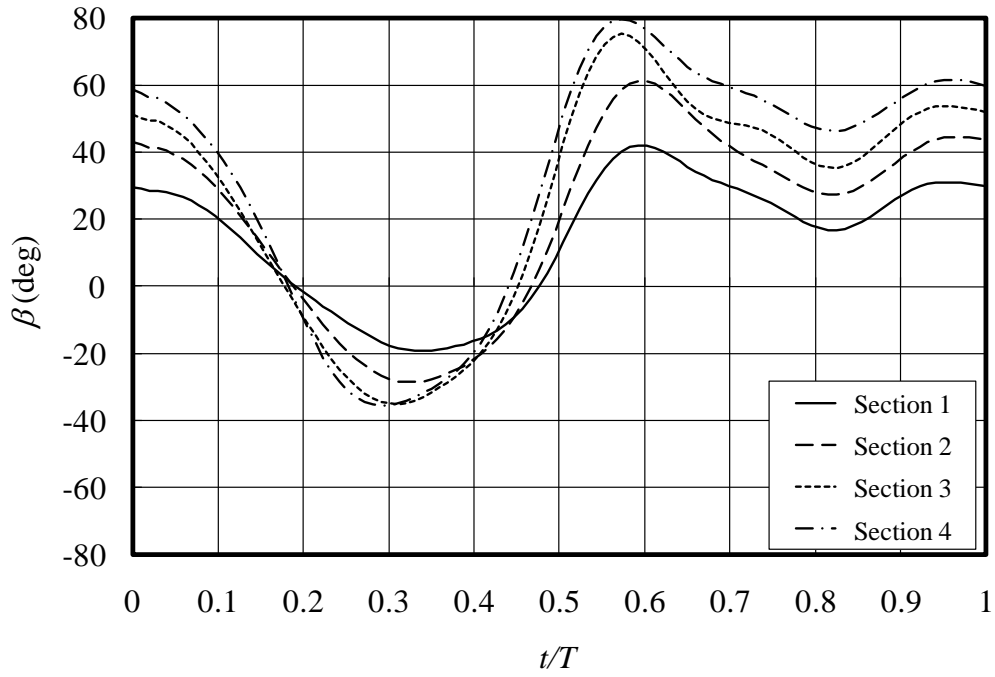


Fig. 21 Time variation of pitching angle ($f = 22$ Hz, $V = 8.3$ m/s).

Effects of the freestream on the front spar deformations at a flapping frequency of 22 Hz can be seen in Figs. 22 and 23. Distinctly from the no-freestream conditions, the spar bends in the direction of the airflow over the entire downstroke. The maximum z_ϕ -deformation of the wing tip is more than 0.4 of the wing's length.

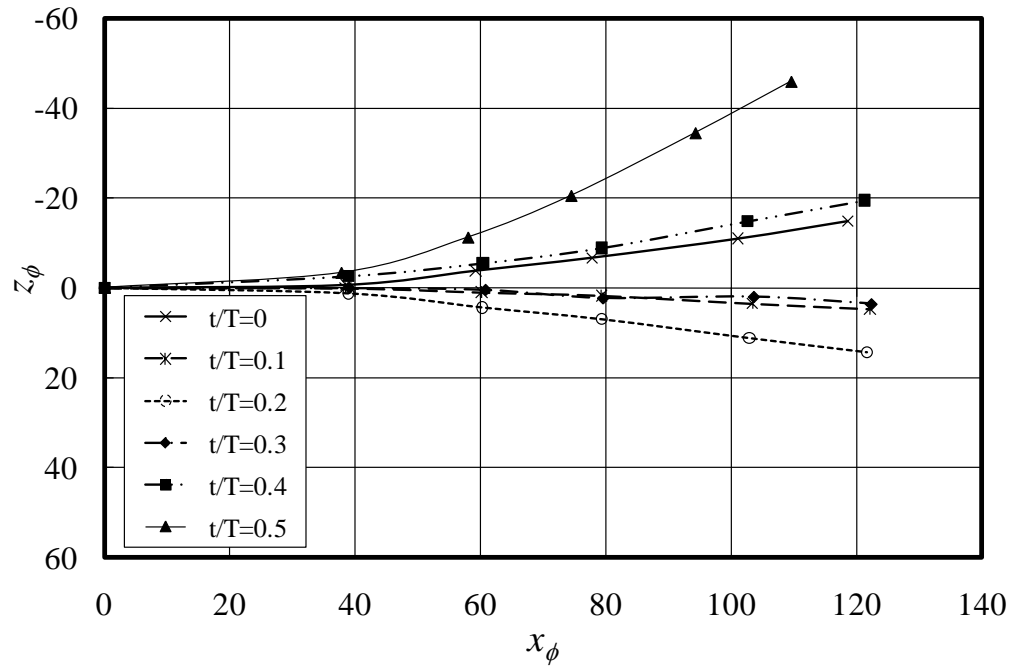


Fig. 22 Spar deformations during upstroke ($f = 22$ Hz, $V = 8.3$ m/s).

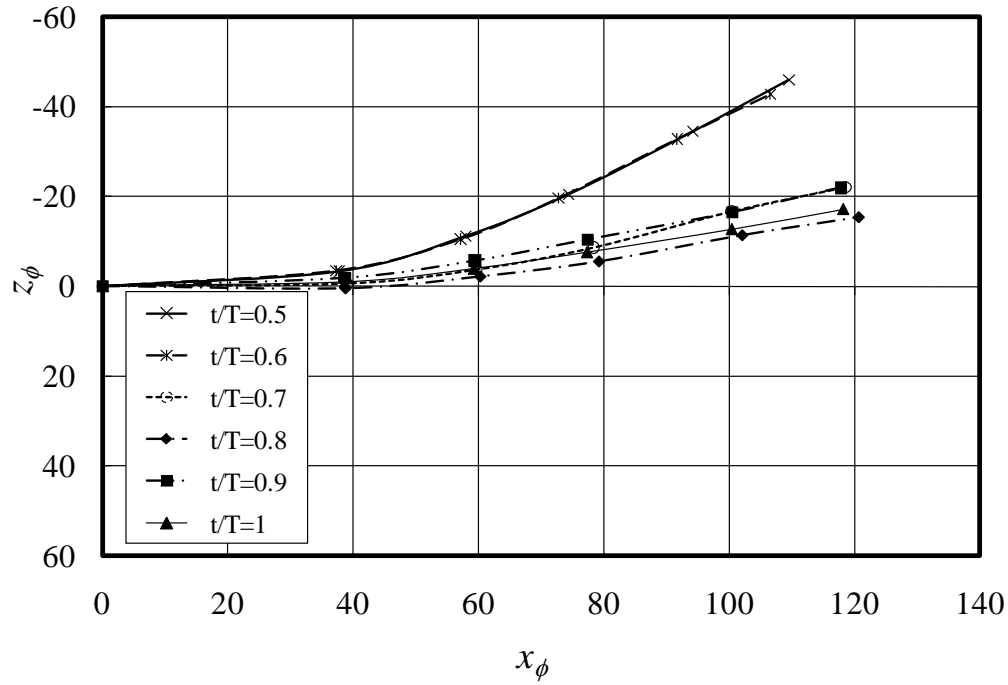


Fig. 23 Spar deformations during downstroke ($f = 22$ Hz, $V = 8.3$ m/s).

A comparison of results for kinematic parameters and deformations with and without a freestream suggests strong interactions of airflow and the structure of flapping wings in the presence of the freestream, influencing flapping angles, pitching angles, and deformations of the front spar, which is out of the wing's plane. Noticeably, camber deformations and deformations of the front spar in the wing's plane are affected by a freestream only slightly.

2.4. Computational Modeling of Airflow around Flapping Wings

Experimental kinematic data are utilized in the computational modeling of airflow around flapping wings. The problem is treated as a quasi-three-dimensional fluid dynamics problem. The solution to this problem is derived using two-dimensional solutions for a number of sections obtained by the Lagrange's Method of Discrete Vortices (MDV) [2.17], improved for non-stationary problems [2.18] and generalized for a viscous vortical medium (IMDV) [2.19, 2.20].

In the proposed approach, the validation process is split in two parts: (1) validation of the IMDV for solving two-dimensional problems and (2) validation of quasi-three-dimensional approach proposed in the present study. The latter is performed in Sections V.C and D by way of comparison against experimental data for the three-dimensional membrane flapping wing [2.13, 2.14].

The two-dimensional IMDV was validated by comparing with available experimental data for a number of stationary and non-stationary problems. Results and discussions of validation of the IMDV are presented in [2.20] and are briefly summarized here. In particular, a problem of a stationary flat plate normal to the airflow was investigated. Numerical results for mean drag coefficients are close to the approximation formula proposed by Ellington [2.21] and relevant experimental data obtained by Dickinson and Gotz data [2.21] for the range of Reynolds numbers appropriate to insect flight (the difference does not exceed 8%).

Simultaneous measurements of time-dependent lift and drag and flow visualization around a flat plate moving in a viscous medium at $Re = 192$ with constant acceleration from rest to given constant velocity at a given angle of attack were conducted by Dickinson and Gotz [2.22]. These experiments were simulated by the IMDV as well. Numerical time histories for drag and lift coefficients [2.20] were found to be in a satisfactory agreement with experimental data [2.22]. Simulated flow patterns around an airfoil and Karman vortex street correlated well with images of experimental flow visualization videos.

A sinusoidal flapping and pitching motion of a flat wing in a still medium was studied in [2.23] experimentally and using two-dimensional numerical analysis. IMDV two-dimensional simulations of instantaneous lift and drag conducted in [2.20] agreed well with experiments for all considered kinematic pattern modes.

Consider a 3D problem of airflow around a pair of membrane flapping wings. Simplifying assumptions concerning the airflow and wing properties follow. Medium D , is continuous, incompressible, and weightless. There are no vortices in any point D at the initial instant of time. The wings are assumed impenetrable and infinitely thin. Aerodynamic interferences between wings are ignored, thus the motion of one wing, S , in the medium D , is analyzed.

The solution to this 3D fluid dynamics problem is constructed using separate 2D solutions. In the current approach, the spanwise flow and following wing tip effects are neglected. The wing is divided into n panels of area $S_j (j=1, n)$ (see Fig. 24). A quadrilateral panel, $A_j B_j C_j D_j$, is represented by a straight airfoil section, j . It is assumed that particles of air move along this section.

Assume that the distance between points on leading and trailing edges remains unchanged, $c_j = \text{const}$. Deformations of the wing's components during flapping cause a rotation of each airfoil section roughly in the plane, which is approximately perpendicular to the plane $z_{\phi_j} = 0$. Therefore, the mapping of a 3D motion of each airfoil section j on a plane is prescribed by a plunging motion of the leading edge point, E_j , as $q_j(t) = l_j \phi_j(t)$ and by rotational motion about this point of the straight airfoil section with the pitching angle $\beta_j(t)$, which is defined positive if viewed anticlockwise rotation from the tip of the x_{ϕ_j} -axis and approximately equal to the angle between the current position of a section and its projection onto a plane $z_{\phi_j} = 0$.

Then, the angle of attack of a section is defined as the angle between an undisturbed relative velocity of the air in a neighborhood of the leading edge and a chordline of the 2D section:

$$\alpha = \begin{cases} -\pi/2 + \beta, & \dot{q} < V \\ \pi/2 + \beta, & \dot{q} > V \end{cases} \quad (3)$$

The positive angle of attack corresponds to the counter clockwise rotation of the chord about its leading edge towards the free stream direction.

This procedure reduces a 3D problem to a set of 2D ones. Two-dimensional problems are solved for n sections. The total aerodynamic force acting on the flapping wing is obtained by adding all the forces acting upon the panels. The formulated 2D problem has been solved by the IMDV [2.17-2.20].

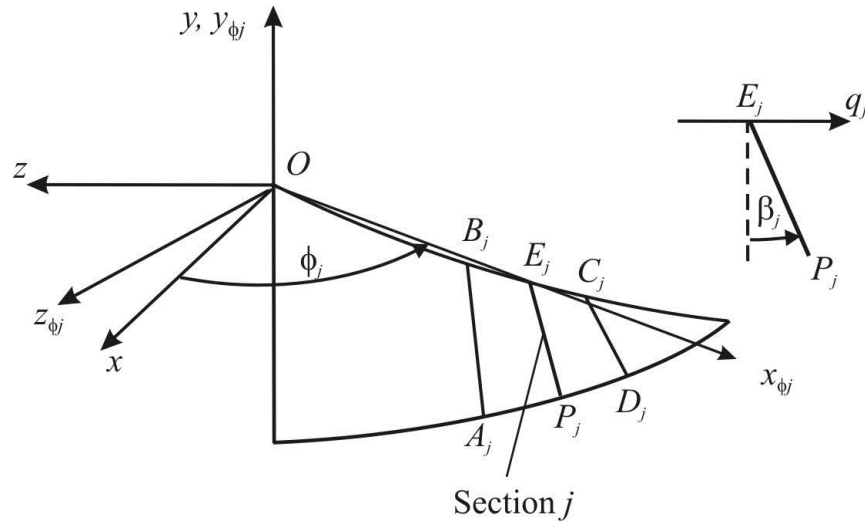


Fig. 24 Representative section and its 2D kinematical model.

The aerodynamic forces are nondimensionalized by the chord length, c_j , and the characteristic velocity $V_C = \sqrt{V^2 + (2R\dot{\Phi})^2}$. By applying an analog of the Cauchy–Lagrange integral for the viscous vortical incompressible medium [2.19] to the lower and upper surfaces of the wing section, a pressure differential coefficient at point $\mathbf{r} \in S$ was derived in [2.20] as

$$\Delta C_p(\mathbf{r}, t) = 2 \left[\mathbf{g} \times \mathbf{n} \cdot \left(\mathbf{U} - \frac{\partial \mathbf{r}}{\partial t} \right) + \frac{\partial'}{\partial t} \left(\int_{\sigma_1}^r + \int_{r_1}^r \Gamma_0 dr_0 \right) \right] \quad (4)$$

Here, the position vector, \mathbf{r}_1 , corresponds to the wing's edge point, where shedding of the vortex σ_1 occurs, and a prime denotes differentiation in the frame of reference moving with the wing. The circulation, Γ_0 , is positively defined when it is in the clockwise direction. Other parameters of this equation are defined in *Nomenclature*.

The pressure differential coefficient comprises circulatory, vortical, and inertial components [2.24]:

$$\Delta C_p(\mathbf{r}, t) = \Delta C_{pc}(\mathbf{r}, t) + \Delta C_{pv}(\mathbf{r}, t) + \Delta C_{pi}(\mathbf{r}, t) \quad (5)$$

given by

$$\Delta C_{pc}(\mathbf{r}, t) = 2 \mathbf{g} \times \mathbf{n} \cdot \left(\mathbf{V} + \hat{\mathbf{U}} - \frac{\partial \mathbf{r}}{\partial t} \right) \quad (6)$$

$$\Delta C_{pv}(\mathbf{r}, t) = 2 \mathbf{g} \times \mathbf{n} \cdot \tilde{\mathbf{U}} \quad (7)$$

$$\Delta C_{pi}(\mathbf{r}, t) = 2 \frac{\partial'}{\partial t} \left(\int_{\sigma_1}^r \Gamma_0 dr_0 \right) \quad (8)$$

where $\hat{\mathbf{U}}$ is a velocity induced by a vortex layer replacing the wing surface and $\tilde{\mathbf{U}}$ is a velocity induced by a vortex shedding from the sharp wing edges.

Then, the normal force coefficient for a 2D section is found by integrating Eq. (5):

$$C_n(t) = \int_S \Delta C_p(\mathbf{r}, t) ds \quad (9)$$

Similarly, circulatory $C_{nc}(t)$, vortical $C_{nv}(t)$, and inertial $C_{ni}(t)$ components of the normal force coefficient are derived by integrating Eqs. (6-8).

The decomposition of the normal force coefficient has a clear physical substantiation. The circulatory component is analogous to a quasi-stationary lift force per a Kutta-Joukowski formula and is determined by an instantaneous velocity circulation around a path enclosing the

wing (without accounting for shed vortices). The vortical (induced) component is determined by the magnitude of the vorticity and its distribution around the wing. The inertial component is a nonstationary one and depends on the rate of change of added masses.

Vertical and horizontal components of the normal force coefficient in the xyz coordinate system are expressed as

$$C_y(t) = C_n(t) \sin \beta(t) \quad (10)$$

$$C_x(t) = C_n(t) \cos \beta(t) \cos \phi(t) \quad (11)$$

Integrating these coefficients over m flapping cycles gives stroke-averaged aerodynamic coefficients for the j -th section:

$$C_{nj} = \frac{1}{mT} \int_{kT}^{T(k+m)} C_n(t) dt \quad (12)$$

$$C_{xj} = \frac{1}{mT} \int_{kT}^{T(k+m)} C_x(t) dt \quad (13)$$

$$C_{yj} = \frac{1}{mT} \int_{kT}^{T(k+m)} C_y(t) dt \quad (14)$$

Corresponding aerodynamic coefficients for the entire j -th panel and of the j -th section are assumed to be equal. Aerodynamic forces on the j -th panel are derived by multiplying aerodynamic coefficients for the j -th panel by the area of the panel ΔS_j and dynamic pressure. Then, the total aerodynamic force on the 3D wing is found as a sum of forces acting upon all panels, and hence, wing aerodynamic coefficients are

$$C_X = \frac{1}{S} \sum_{j=0}^n C_{xj} \Delta S_j \quad (15)$$

$$C_Y = \frac{1}{S} \sum_{j=0}^n C_{yj} \Delta S_j \quad (16)$$

where $S = \sum_{j=0}^n \Delta S_{ij}$.

Computational modeling of a viscous vortical flow field around the 25-cm flapping membrane batted wings and calculations of aerodynamic force coefficients have been carried out using the IMDV [2.18-2.20]. Values of parameters utilized in computations are $n = 4$, $k = 1$, and $m = 17$. Following the proposed approach to the solution of the 3D problem, the wing is divided into 5 panels indexed from 0 to 4. Their corresponding areas are 22.1, 15.6, 13, 11, and 6.1 cm^2 . Kinematic data are available for the four sections used in the experiments (Fig. 2). The panel and section having index $j = 0$ are introduced coincident with the root chord. Since the wing was fixed at the root, the vertical force coefficient $C_{y0} = 0$. Values of the local Reynolds number at no-freestream are presented in Table 2 for the coefficient of kinematic viscosity $\nu = 1.68 \cdot 10^{-5} \text{ m}^2 / \text{s}$.

Table 2 Local Reynolds number at no-freestream.

$f, \text{ Hz}$	Re_j			
	Section	Section	Section	Section
	1	2	3	4
10	$1.2 \cdot 10^4$	$1.1 \cdot 10^4$	$9 \cdot 10^3$	$5 \cdot 10^3$
15	$1.8 \cdot 10^4$	$1.6 \cdot 10^4$	$1.3 \cdot 10^4$	$7.4 \cdot 10^3$
22	$2.7 \cdot 10^4$	$2.4 \cdot 10^4$	$2 \cdot 10^4$	$1.1 \cdot 10^4$

Numerical results for the vertical force coefficients C_{yj} at four sections ($j = 1, 4$) and for the entire wing C_y under conditions at no-freestream are shown in Table 3. In the previous study

[2.13], the stroke-averaged forces were measured on 25-cm wing model and corresponding force coefficients are also presented in Table 3.

It is noteworthy that significant scatter is inherent to experiments on flapping wings. Therefore, the mean force coefficients and uncertainty intervals corresponding to 90% confidence were determined in [2.13]. The uncertainty intervals as fractions of mean values are 13.5%, 5.9% and 3.4% for flapping frequencies of 10, 15, and 22 Hz, respectively.

Differences between mean experimental values and numerical results are also presented in Table 3. At $f = 15$ Hz the difference and uncertainty interval are rather small values. For $f = 10$ and 22 Hz, the values of uncertainties are smaller than differences of means and this fact allows comparison of mean experimental and theoretical results. It can be seen that theoretical and experimental mean results for the wing are in satisfactory agreement.

Table 3 Numerical and experimental values of stroke-averaged vertical force coefficients without freestream.

Frequency	Numerical					Experimental [13]	Difference
Hz	C_{y1}	C_{y2}	C_{y3}	C_{y4}	C_Y	C_Y	%
10	0.370	0.764	1.175	1.062	0.518	0.694	25.4
15	0.506	1.038	1.546	1.408	0.693	0.703	1.4
22	0.533	1.024	1.798	1.317	0.729	0.556	-31.1

Numerical results for the time-varying normal force coefficient $C_n(t)$ and its inertial component $C_{ni}(t)$ for Section 2 are presented in Fig. 25. These results correspond to the first

flapping stroke, therefore all force coefficients start at zero. The ratio of the stroke-averaged coefficients is $C_{ni2}/C_{n2} = 1.13$, while the contributions of both C_{nc2} and C_{nv2} are small and negative. Evidently, the inertial component is dominant in the normal force coefficient, and hence, the inertia of airflow accelerated by the moving airfoil section is the main mechanism in the production of aerodynamic force in the studied problem.

In vortical flows, instant added masses depend on the body's form and acceleration (on instant acceleration vector), as well as on intensity and location of vortices around an accelerating body. The stationary effect of local pressure reduction induced by a rotating fluid in a vortex may be small or even negative. If the effect of induced pressure is negative and the circulatory part is small or negative, then the contribution of the inertial part may exceed 100% (see Fig. 25).

Note that aerodynamic forces created by fluid inertia act in a direction normal to the wing surface. Also, per Eq. (8), the inertial component is characterized by a rate of change of the circulation, which is a circulation of the acceleration of moving air. Based on these considerations and in accordance with Newton's third law a new parameter is introduced for the flow analysis - a normal acceleration of the wing trailing edge taken with negative sign as

$$a = -\ddot{\beta} - \dot{q} \cos \beta \quad (17)$$

Its physical meaning is a normal component of the relative acceleration of undisturbed air in the neighborhood of the wing's trailing edge. Note that this parameter is suitable when a membrane rotates about the leading edge spar. All parameters in Eq. (17) are presented in nondimensional form. The proposed acceleration parameter is valid for the case of section's rotational axis coincident with the leading edge of the wing.

Time variation of the acceleration, a , and its components are also presented in Fig. 25. Plots show overall agreement in trends of accelerations and force coefficients. There is also a phase lag between them. The existence of the phase lag in the normal force coefficients is explained by the inertia of masses of air delaying the generation of forces on the wing.

No correlations are observed between normal force coefficients and the angle of attack, α . This was expected, because numerical simulations showed that flow separates from the sharp edges over the entire stroke and for all frequencies studied. It supports the conclusion that generation of aerodynamic forces on the studied wing cannot be explained by the circulation mechanism.

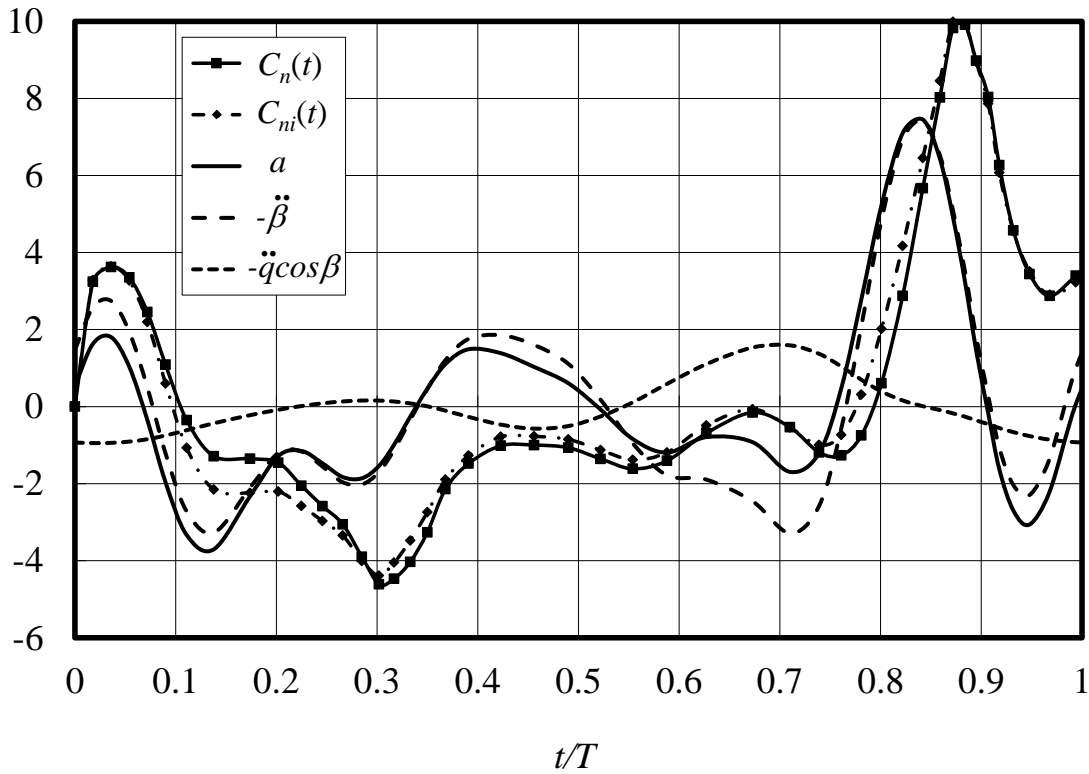


Fig. 25 Time variations of normal force coefficient, normal acceleration, and components (Section 2, $f = 22$ Hz).

Consider time variations of the vertical force coefficient, C_{y2} , and acceleration, a , jointly with the pitching angle, β , for Section 2. Importance of the synchronization of parameters a and β for achieving maxima in C_y follows from an analysis of Eqs. (8-10). From Fig. 26, it is seen that each extremum of C_{y2} is preceded by the extremum in a . Not as strong a relationship can be observed between β and C_{y2} (Figs. 9 and 26). Also, correlations are observed between absolute values of these parameters in transients.

With an increase in flapping frequency, the first significant extremum of the acceleration decreases by about 2 times and shifts to the left (Figs. 27 and 28). At $f = 22$ Hz, there is another smaller peak in a , causing time delays in the following extrema of a , C_{y2} , and β (Figs. 28 and 11). Then, a and β are further desynchronized resulting in two extrema in a for each extremum in β . These kinematical changes result in about a 40% decrease in the maximum of C_{y2} at $f = 22$ Hz compared to $f = 15$ Hz.

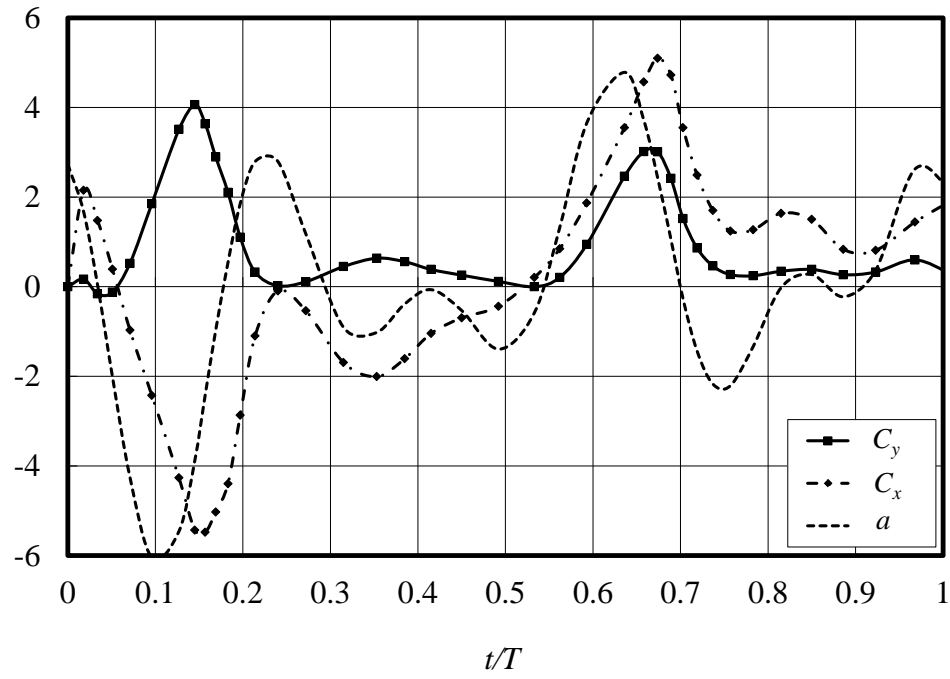


Fig. 26 Time variation of force coefficients and normal acceleration (Section 2, $f = 10$ Hz).

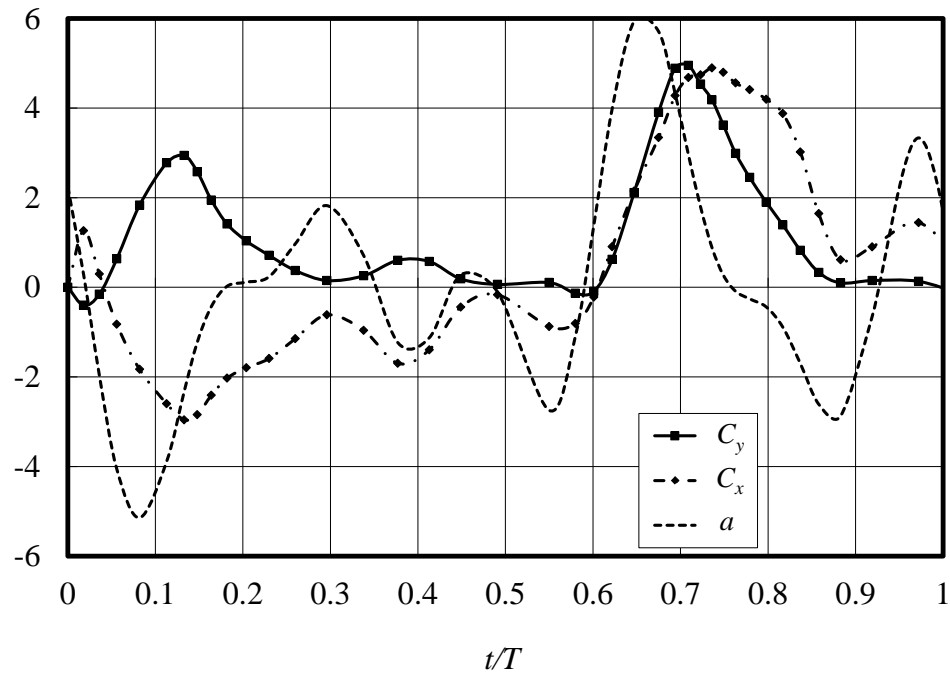


Fig. 27 Time variation of force coefficients and normal acceleration (Section 2, $f = 15$ Hz).

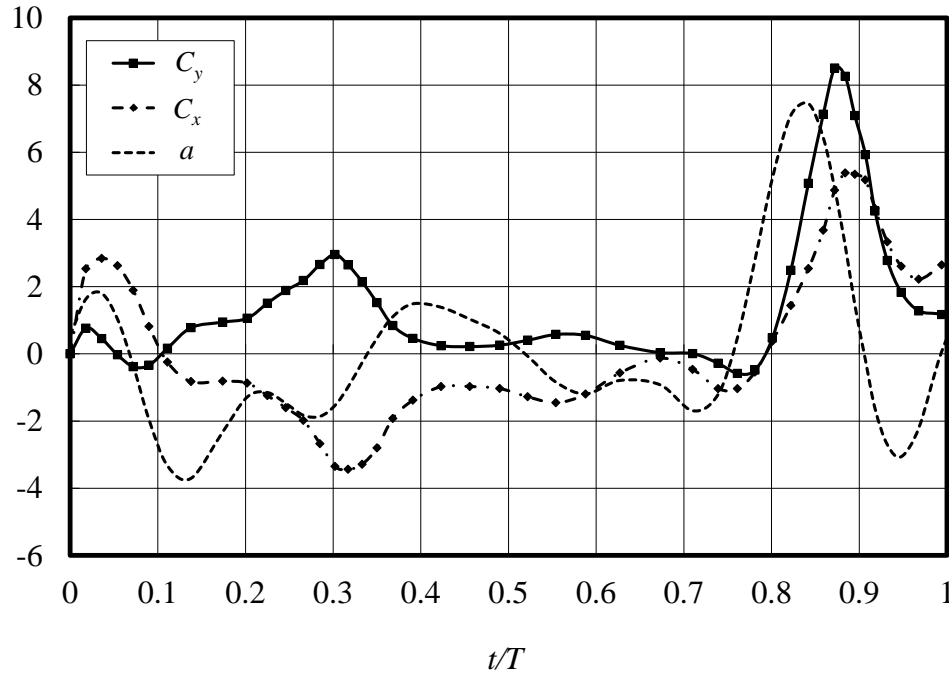


Fig. 28 Time variation of force coefficients and normal acceleration (Section 2, $f = 22$ Hz).

Flow features around Section 2 at $f = 22$ Hz are illustrated in Fig. 29 using velocity vector fields, streamlines, and equal pressure coefficient lines. The streamlines were computed with a step of 0.05 and equal pressure coefficient lines are computed with a step of 0.25. Resultant force vectors downscaled by a factor of 2 are shown applied to the center of pressure.

The visualizations show that computations carried out in the present study are physically correct. It is seen that velocity and pressure boundary conditions are satisfied. Specifically, the zero streamline and zero pressure coefficient line approach infinity. At the wing crossing, absolute velocity vectors and pressure coefficients exhibit a jump discontinuity, while streamlines are continues, but not differentiable across the wing. Moreover, all three visualizations correlate well with each other.

It is seen that during wing motion the air flows around its edges into the zone behind the wing forming vortices that trail the wing. However, no correlations observed between vortices

attached to the wing and aerodynamic loads. In fact, at $t/T = 3/4$ there are almost no vortices by the wing, while aerodynamic forces are reaching maxima (Fig. 25, 28). In contrast, by a quarter of the stroke later, at about $t/T = 1$, vortical motion is very intense, but normal forces decrease by a factor of 2. It confirms a prevailing influence of the added mass mechanism in aerodynamic force production and, hence, the major contribution of the inertial component in force coefficients.

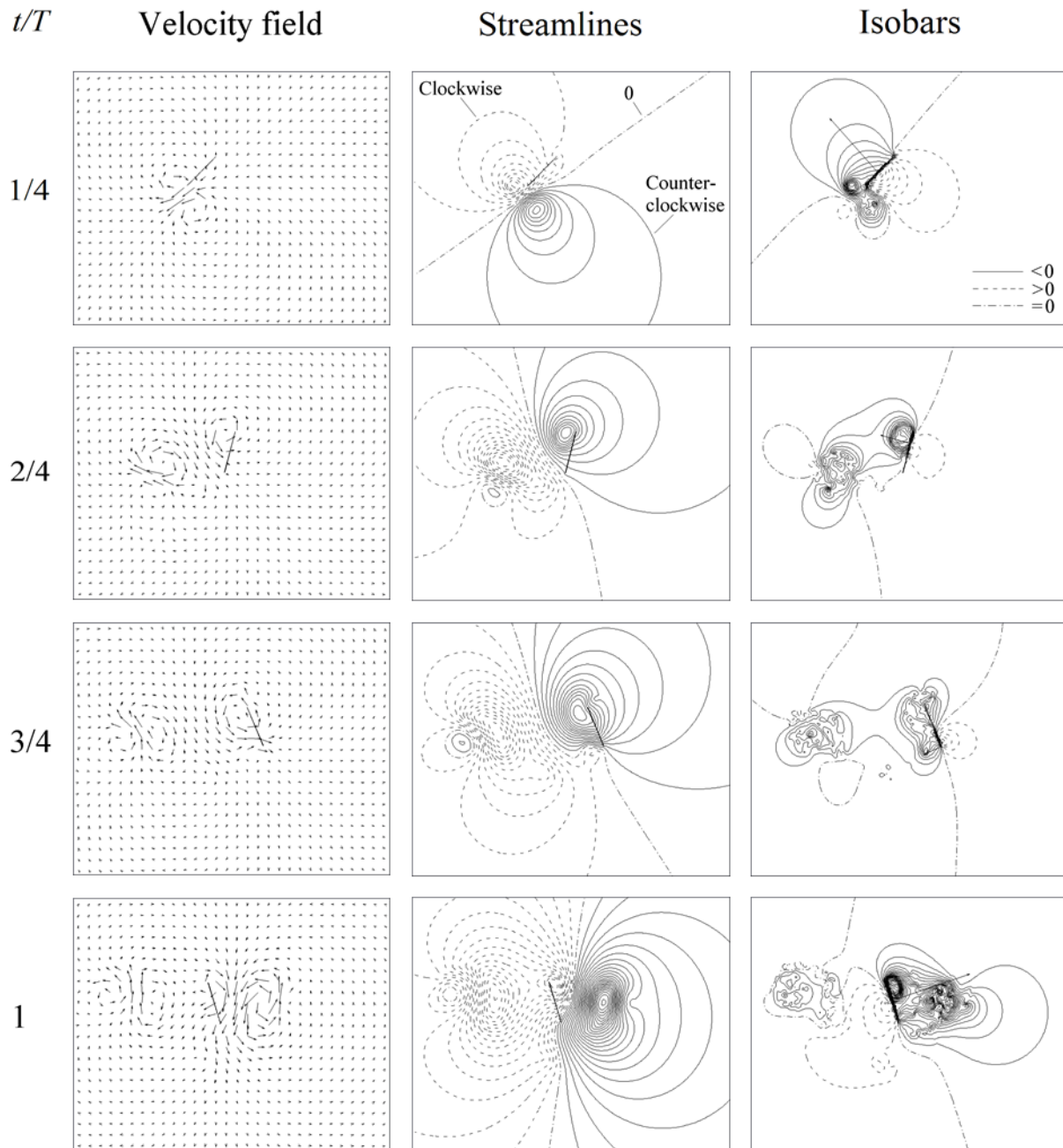


Fig. 29 Velocity fields, streamlines, and equal pressure coefficient lines (Section 2, $f = 22$ Hz).

Computational modeling of airflow around the flapping wings in the presence of a freestream has been conducted at $f = 22$ Hz for the wing installed normal at 90° to the freestream. This position of the wing serves as a model of flights at very high angles of attack or transition flights from level to hover and back. Because of this position of the wing, it is assumed that $C_{x0} = C_{x1}$ and $C_{y0} = 0$. Effects of a freestream on aerodynamics are presented for $V = 5.5$ and 8.3 m/s. Reynolds number values for conditions studied are presented in Table 4.

Table 4 Local Reynolds number in freestream at $f = 22$ Hz.

V , m/s	Re_j			
	Section	Section	Section	Section
	1	2	3	4
5.5	$2.1 \cdot 10^4$	$1.9 \cdot 10^4$	$1.6 \cdot 10^4$	$8.6 \cdot 10^3$
8.3	$3.2 \cdot 10^4$	$2.9 \cdot 10^4$	$2.3 \cdot 10^4$	$1.3 \cdot 10^4$

Results of calculations of force coefficients C_{xi} and C_{yi} for 2D sections and C_x and C_y for the entire 3D wing are given in Tables 5 and 6. In the previous study [2.14], the stroke-averaged forces Y and X on the wing model were measured in the wind tunnel. Their values and force coefficients determined as $C_y = Y / (0.5 \rho V_c^2 S)$ and $C_x = X / (0.5 \rho V_c^2 S)$ are presented in Tables 5 and 6, respectively. Note that these force coefficients were given incorrectly in [2.25]. Similarly to no-wind conditions, the scatter was noticeable in wind tunnel experiments. Corresponding to 90% confidence level uncertainty intervals for vertical and horizontal force coefficients are estimated as (7.0%, 5.8%) and (9.9%, 9.7%) at $V = 5.5$ and 8.3 m/s, respectively.

Stroke-averaged experimental force coefficients are presented in Tables 5 and 6 along with their differences from numerical results. Overall, experimental and numerical results for the wing agree well. Experimental values of force coefficients are greater than corresponding numerical by 10.3% on average. With speed increased from 5.5 m/s to 8.3 m/s, numerical value of C_y decreases and of C_x increases following trends observed in experiments. Normal force coefficients and accelerations are presented in Figs. 30 and 31 for speeds of 5.5 and 8.3 m/s, respectively. Strong correlations exist for the normal force coefficient with normal accelerations and pitching angle. Clearly, the inertial component dominates normal force. Similar results were obtained in the case with no-freestream.

Without a freestream, the amplitude of the angle of attack is always $\alpha_{\max} - \alpha_{\min} = 180^\circ$. However, there are distinctive features in the relative velocity of an undisturbed flow development in the case of a freestream. On the downstroke, the wing rotates against the wind, while on the upstroke the wing rotates into the wind and the angle of attack may exceed 90° for Sections 3 and 4 ($\alpha_{\max} = 130^\circ$ at $V = 5.5$ m/s for Section 3). At the beginning of the upstroke, the wing's membrane deflects at the pitching angle of about 40° clockwise, and the airflow pushes the wing from behind. With further flapping speed increase, the relative velocity of undisturbed flow reverses the direction. However, it does not happen to Sections 1 and 2, for which the airflow pushes the wing from behind for the entire upstroke.

Table 5 Numerical and experimental values of vertical force coefficients at $f = 22$ Hz.

Velocity	Numerical					Experimental [2.14]		Difference
m/s	C_{y1}	C_{y2}	C_{y3}	C_{y4}	C_Y	Y , N	C_Y	%
5.5	0.446	0.849	1.116	0.989	0.535	0.365	0.622	14.0
8.3	0.447	0.713	0.906	0.790	0.458	0.431	0.490	6.6

Table 6 Numerical and experimental values of horizontal force coefficients at $f = 22$ Hz.

Velocity	Numerical					Experimental [2.14]		Difference
m/s	C_{x1}	C_{x2}	C_{x3}	C_{x4}	C_X	X , N	C_X	%
5.5	0.661	0.658	0.652	0.355	0.631	0.431	0.734	14.1
8.3	0.934	0.850	0.764	0.414	0.844	0.792	0.901	6.4

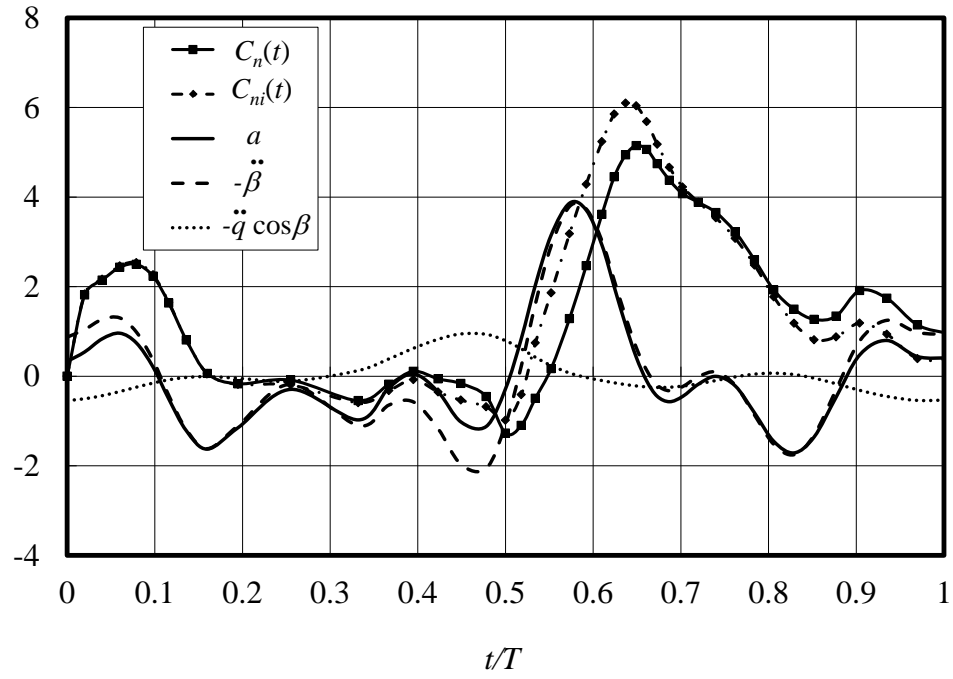


Fig. 30 Time variations of normal force coefficient, normal acceleration, and their components (Section 2, $f = 22$ Hz, $V = 5.5$ m/s).

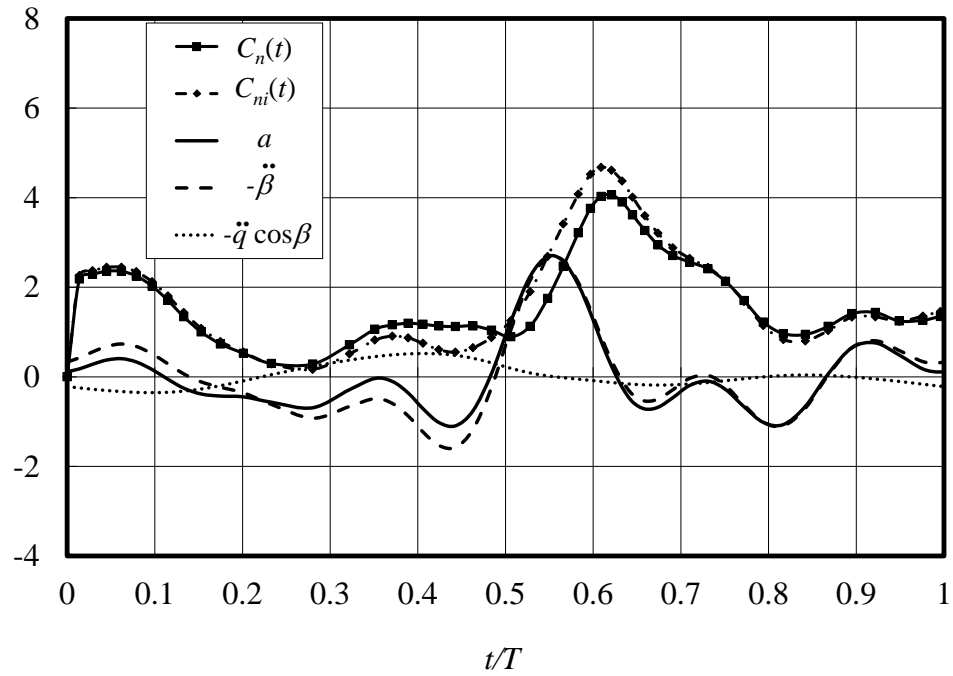


Fig. 31 Time variations of normal force coefficient, normal acceleration, and their components (Section 2, $f = 22$ Hz, $V = 8.3$ m/s).

As revealed in IV.B, in the presence of a freestream the modulus of the global minimum of the pitching angle significantly decreases (Figs. 11, 20, and 21). This results in a rather small vertical component and a higher horizontal component of the force coefficient on the upstroke (Figs. 28, 32, and 33). Similar to the case of no-freestream, no correlations of aerodynamic coefficients with angle of attack, α , are found.

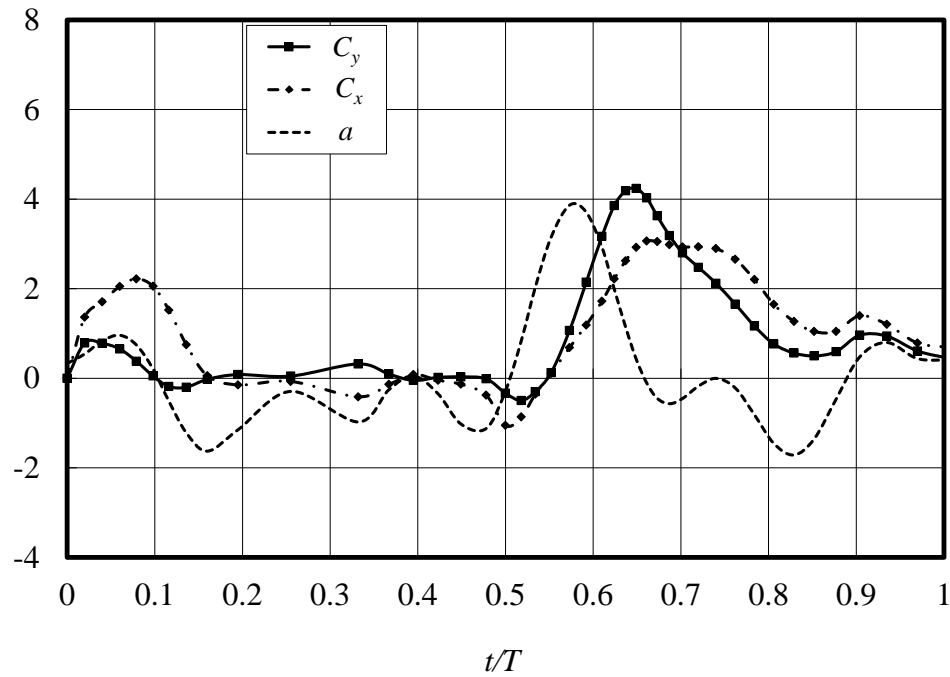


Fig. 32 Time variation of force coefficients and normal acceleration (Section 2, $f = 22$ Hz, $V = 5.5$ m/s).

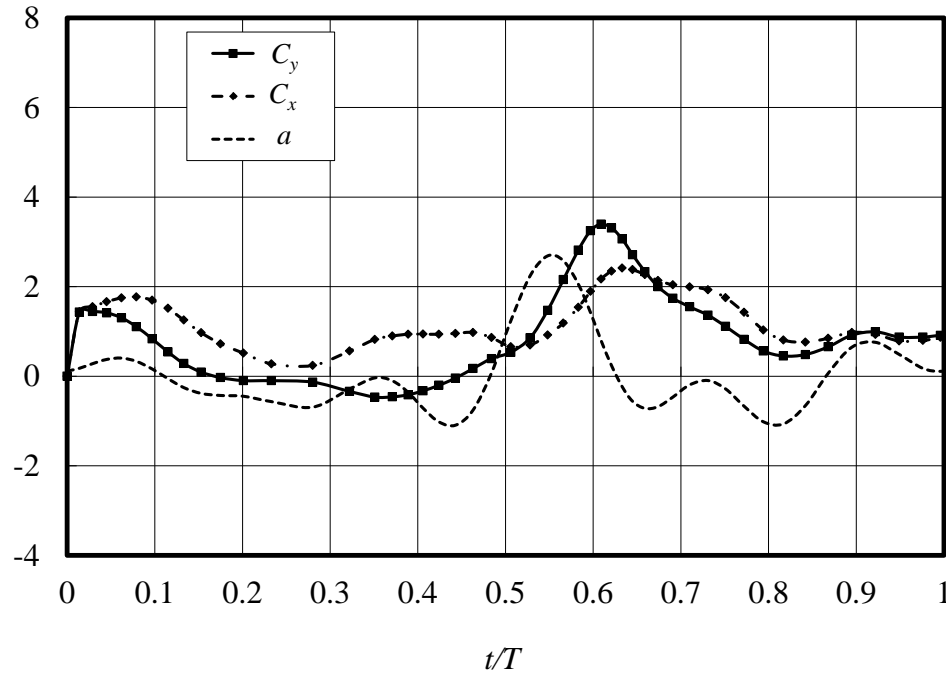


Fig. 33 Time variation of force coefficients and acceleration (Section 2, $V=8.3$ m/s).

Figure 34 shows computer visualizations of velocity fields, streamlines, and equal pressure coefficient lines for Section 2 at $V = 8.3$ m/s and $f = 22$ Hz. The streamlines were computed with a step of 0.1 and equal pressure coefficient lines are computed with a step of 0.25. Resultant force vectors downscaled by a factor of 2 are shown applied to the center of pressure. The intensity of vortices is higher than in no free stream case. Note also that wing oscillations are essentially non-symmetrical.

Similarly to the no free stream case, velocity and pressure boundary conditions are satisfied at infinity (equal to zero) and at the wing crossing (attaining discontinuities). A strong correlation exists between intensity of vortices and gradients of negative pressure coefficients and their corresponding locations.

The main feature of the flow structure in this case is a Karman vortex street corresponding to the appearance of the mean horizontal force (drag force). Results of computer visualizations

confirm the development of more intense vortices when the wing is against the wind ($t/T = 0.4 - 1$) than into the wind (Fig. 34).

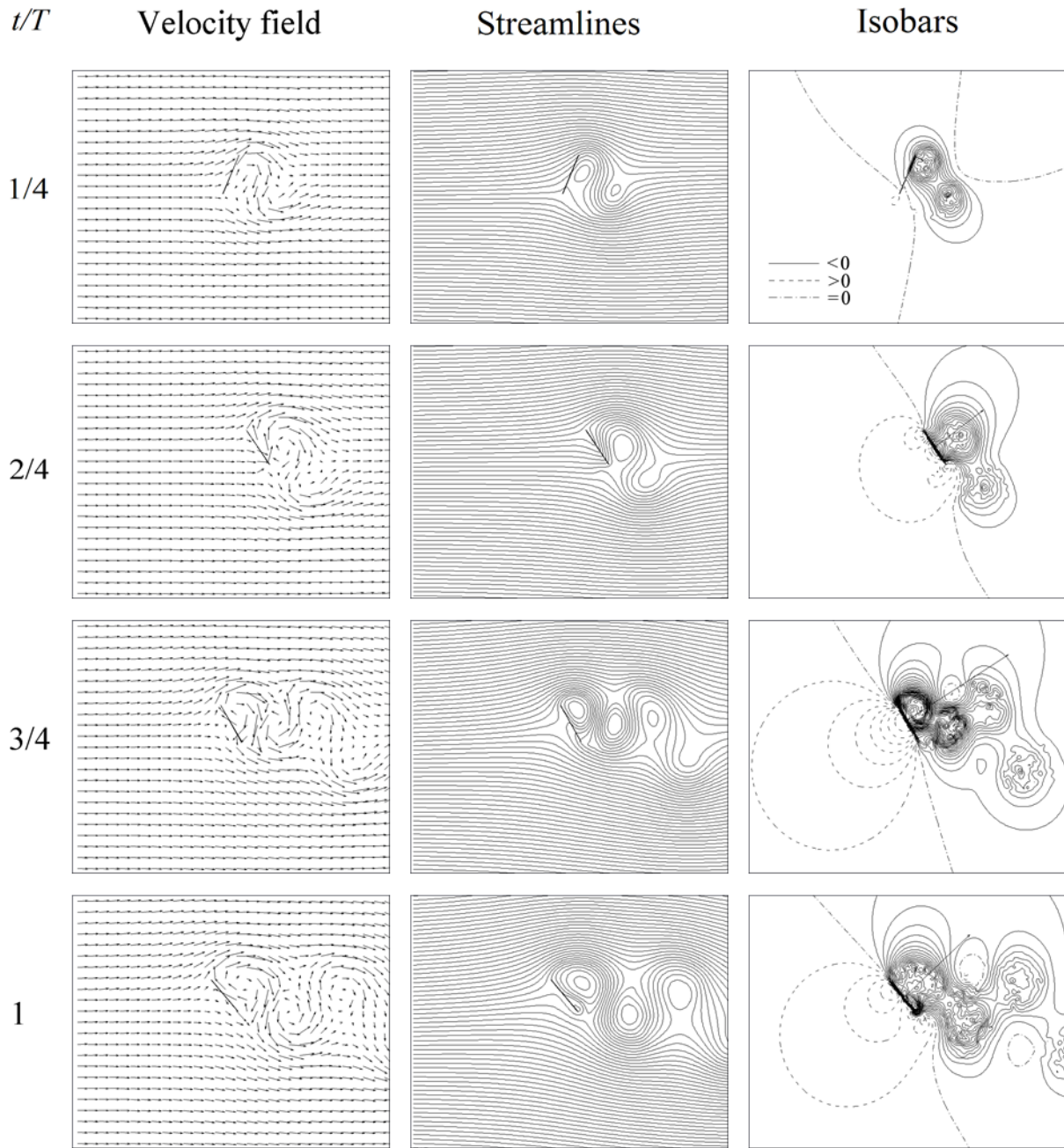


Fig. 34 Velocity fields, streamlines, and equal pressure coefficient (Section 2, $f = 22$ Hz, $V = 8.3$ m/s).

2.5. Summary and References to Chapter 2

Utilizing high-speed videography, data were obtained for time-varying flapping angles, pitching angle, and front spar and camber deformations. The standard deviation of the measurement of linear coordinates averaged over time and distance is 0.26 mm, which confirms a high spatial and temporal resolution of the videography method. Analytical results for the flapping angle in the wing base are representative of perfect revolute joints and do not change with frequency. In experiments, however, the amplitude of the flapping angle and half-stroke duration vary by about 10-15% due to deformations and imperfections in the transmission mechanism.

It was found that the pitching angle exhibits a significant second harmonic and lags the flapping angle. The magnitude of the phase lag increases with an increase in flapping frequency and it is greater for the part of the wing closest to the root. The pitching angle amplitude increases toward the wing's tip. This twisting tendency is analogous to the washout in conventional wings and propellers. The maximum values of pitching angle in the presence of a freestream are slightly smaller than those at zero velocity, but modulus of the minimum values and, consequently, pitching angle amplitudes decrease significantly with an increase in speed.

Maximum deformation of the wing tip out of the wing's plane is about 0.4 of the wing's length. Because the membrane does not support a compressive load, it does not constrain the spar's displacements into the membrane, but the membrane limits the spar's opposite motion. Unlike continuous functions of a flapping angle, the pitching angle and spar deformation, the camber function alternates between two well-separated camber values as the membrane snaps. It suggests that the mechanics of membrane deformations during a flapping cycle is analogous to a

buckling of a bistable structure from one stable equilibrium position to another. Overall, positive and negative cambers are distributed almost evenly during a half-stroke.

Detailed analysis of the underlying physics of airflow around a flapping wing is also provided based on computational fluid dynamics simulations. Numerical and experimental results are in good agreement for the stroke-averaged force coefficients. The average difference in stroke-averaged force coefficients between numerical and experimental values is about 14%. Numerical and experimental values of vertical force coefficients follow the same trends with an increase in freestream speed.

It was found that the inertial component is dominant in the normal force coefficient, and hence, the inertia of airflow accelerated by the moving airfoil section is the main mechanism in the production of aerodynamic force in the studied problem. Contributions of both circulatory and vortical components are small and negative. Based on these observations, a normal component of the acceleration of the wing's trailing edge taken with a negative sign is introduced as a kinematic parameter that is essential in flapping wings aerodynamics. This parameter is suitable when a membrane rotates about the leading edge spar. Results show a satisfactory agreement in trends of the acceleration and force coefficients. They also reveal phase shifts between them. No correlations are observed between normal force coefficients and the angle of attack. This supports the conclusion that generation of aerodynamic forces on the studied wing cannot be explained by the circulation mechanism. Analysis also shows that synchronization of normal acceleration and pitching angle is important for achieving maximum values of vertical force coefficients.

References

- [2.1] Zeng, L., Hao, Q. and Kawachi, K., “A Scanning Projected Line Method for Measuring a Beating Bumblebee Wing,” *Optics Communications*, Vol. 183, 2000, pp. 37-43.
- [2.2] Wang, H., Zeng, L., Liu, H., and Yin, C., “Measuring Wing Kinematics, Flight Trajectory and Body Attitude During Forward Flight and Turning Maneuvers in Dragonflies,” *The Journal of Experimental Biology*, Vol. 206, 2003, pp. 745-757.
- [2.3] Liu, T. and Burner, A., Photogrammetry Toolbox Reference Manual, NASA/CR-2007-000000, 2007.
- [2.4] Hedrick, T. L., “Software Techniques for Two- and Three-dimensional Kinematic Measurements of Biological and Biomimetic Systems,” *Bioinspiration & Biomimetics*, Vol. 3, 034001, 2008.
- [2.5] Walker, S., Thomas, A., and Taylor, G., “Photogrammetric Reconstruction of High-resolution Surface Topographies and Deformable Wing Kinematics of Tethered Locusts and Free-flying Hoverflies,” *Journal of the Royal Society Interface*, Vol. 6, No 33, 2009, pp. 351-366.
- [2.6] Walker, S., Thomas, A., and Taylor, G., “Deformable Wing Kinematics in the Desert Locust: How and Why do Camber, Twist and Topography Vary Through the Stroke?,” *Journal of the Royal Society Interface*, Vol. 6, No. 38, 2009, pp. 735-747.
- [2.7] Young, J., Walker, S., Bompfrey, R., Taylor, G., and Thomas, A., “Details of Insect Wing Design and Deformation Enhance Aerodynamic Function and Flight Efficiency,” *Science*, Vol. 325, No. 18, 2009, pp. 1549-1552.

- [2.8] Ho, S., Nassef, H., Pornsinsirak, N., Tai, Y., and Ho, C., “Unsteady Aerodynamics and Flow Control for Flapping Wing Flyers,” *Progress in Aerospace Sciences*, Vol. 39, No. 8, 2003, pp. 635–681. doi:10.1016/j.paerosci.2003.04.001.
- [2.9] Singh, B., and Chopra, I., “Insect-based Hover-capable Flapping Wings for Micro Air Vehicles: Experiments and Analysis,” *AIAA Journal*, Vol. 46, No. 9, 2008, pp. 2115–2124. doi:10.2514/1.28192
- [2.10] Wu, P., Stanford, B., Bowman, W., Schwartz, A., and Ifju, P., “Digital Image Correlation Techniques for Full-field Displacement Measurements of Micro Air Vehicle Flapping Wings,” *Experimental Techniques*, November/December 2009, pp. 53-58.
- [2.11] Wu, P., Ifju, P., and Stanford, B., “Flapping Wing Structural Deformation and Thrust Correlation Study with Flexible Membrane Wings,” *AIAA Journal*, November/December 2009, pp. 53-58.
- [2.12] Shkarayev, S., and Silin, D., “Aerodynamics of Flapping-Wing Micro Air Vehicles,” AIAA Paper 2009-878, January 2009.
- [2.13] Shkarayev, S., and Silin, D., “Applications of Actuator Disk Theory to Membrane Flapping Wings,” *AIAA Journal*, Vol. 48, No. 10, 2010, pp. 227-2234.
- [2.14] Shkarayev, S., Silin, D., Abate, G., and Albertani, R., “Aerodynamics of Cambered Membrane Flapping Wings,” AIAA Paper 2010-58, January 2010.
- [2.15] Maxon DC Motors, Product Catalog 06/07, Maxon Precision Motors, Inc., 101 Waldron Road, Fall River, MA 02820; website: maxonmotorusa.com.
- [2.16] Albertani, R., and Babcock, J., “Analysis of Wind Tunnel Unsteady Aerodynamic Data of Flexible Micro Air Vehicle Wings,” AIAA Paper 2008-6249, August 2008.

- [2.17] Belotserkovsky, S. M., and Lifanov, I. K., *Method of Discrete Vortices*, CRS Press, Boca Raton, FL, 1993, 452 p.
- [2.18] Dovgiy S. A., and Shekhovtsov A. V. “An Improved Vortex Lattice Method for Nonstationary Problems,” *J of Math. Sciences*, Vol. 104, No. 6, 2001, pp. 1615-1627.
- [2.19] Shekhovtsov, A.V., “A Method for Evaluation of an Unsteady Pressure Field in a Mixed Potential-Vortical Domain Adjacent to the Rotating Wing,” *International Journal of Fluid Mechanics Research*, Vol. 29, No 1, 2002, pp. 111-123.
- [2.20] Dovgiy, S. A., and Shekhovtsov A. V., “Approbation of the IMDV for a Class of Problems about Oscillations of a Wing in a Viscous Medium with a Restricted Solution on Edges,” *Bulletin of Kharkiv National University*, No 863, 2009, pp. 111-128 [in Russian].
- [2.21] Ellington, C. P., “Aerodynamics and the origin of flight,” *Advances in Insect Physiology*, vol. 23, pp. 171–210, 1991.
- [2.22] Dickinson, M. H. and Gotz, K. G. ,“Unsteady aerodynamic performance of model wings at low Reynolds number,” *The Journal of Experimental Biology*, vol. 174, pp. 45–64, 1993.
- [2.23] Wang Z.J., Birch J.M., and Dickinson M.H., “Unsteady forces and flows in low Reynolds number hovering flight: two-dimensional computations vs robotic wing experiments,” *The Journal of Experimental Biology*, vol. 207, p. 449–460, 2004.
- [2.24] Shekhovtsov, A.V., “Inertial-Vortical Principle of Animal Flight,” *BIONA-Report 12*, edited by W. Nachtigall and A. Wisser, Stuttgart, Jena, Lubeck, 1998, pp. 307-316.
- [2.25] Shkarayev, S., Maniar, G., and Shekhovtsov, A.V., “Experimental and Computational Modeling of the Kinematics and Aerodynamics of Membrane Flapping Wings,” 50th AIAA Aerospace Sciences Meeting Including the New Horizons Forum and Aerospace Exposition, January 9-12, 2012, Nashville, TN, AIAA 2012-1208, 45 p.

3. Insect-Inspired Micro Air Vehicles

In this chapter, three sets of artificial wings are designed, constructed and tested. Locust wing kinematics are quantified and used to design two different transmissions: one strictly flapping and the other a combination of active pitching and flapping. Force data are acquired for the locust and artificial wings; stroke-averaged results are discussed. A 14-cm wingspan radio-controlled ornithopter is designed and built using some considered concepts. This chapter is based on the manuscript entitled “Insect-Inspired Micro Air Vehicles,” by Kumar, R., Randall, R., Silin, D., and Shkarayev, S. This manuscript was accepted for publication as a book chapter in the Handbook of Biomimetics and Bioinspiration, 2013.

Nomenclature

AR	= aspect ratio $AR = b^2/S$ or $AR = 4R^2/S$, depending on assumptions
b	= wingspan (tip-to-tip)
c_i	= a unitless constant, $i = 1, 2$
d	= diameter
E	= modulus of elasticity
f	= flapping/wingbeat frequency (cycles/sec)
g	= acceleration of gravity
J	= flapping-wing advance ratio, $J = V/(2\Phi fR)$
L	= wing-generated lift
L_R	= relative lift (lift as a proportion of body weight)
m	= mass
M_R	= metabolic rate
R	= length of a wing from root-to-tip

S	=	planform area of wings (combined)
t	=	thickness
T	=	wing-generated thrust
V	=	freestream velocity
V_{Pmin}	=	minimum power velocity
Γ	=	flapping-wing dihedral angle, $\Gamma = (\varphi_{max} + \varphi_{min})/2$, φ_{min} is typically negative
ε_u	=	ultimate tensile strain
θ	=	locust hindwing deployment angle
τ	=	instantaneous time divided by flapping cycle period
τ_F	=	applied torque to “fan out” a locust hindwing
ρ	=	density of air or a solid, depending on context
σ_u	=	ultimate tensile stress
Φ	=	peak-to-peak wingbeat amplitude
sub max	=	maximum
sub min	=	minimum

3.1. Aerodynamics of Flapping-Wing Micro Air Vehicles and Insects

Micro air vehicle (MAV) is a term applied to small aircraft with wingspans between approximately 10 and 30 cm; the official Defense Advanced Research Projects Agency (DARPA) size restriction is 15 cm or less [3.1]. MAVs may utilize fixed, rotary, or flapping wings. Flapping-wing aircraft are called ornithopters, and may be informally referred to as “birds”. There are many existing flapping-wing aircraft designs of varying scale from the human-powered “Snowbird” with a wingspan of 32 meters [3.2] down to the “Delfly Micro” with a wingspan of just 10 centimeters [3.3]. This paper will focus on the lower-end of the spectrum, around 10-15 cm.

There are practical reasons to investigate the design of small flapping-wings. For example, flapping-wings are relatively gust-tolerant [3.4], and small ornithopters are stealthy because they share the same mode-of-flight as natural fliers, allowing them to be disguised as birds or insects. Flapping-wing MAVs can be used as sensor platforms carrying cameras, chemical sensors or anything that is sufficiently small and lightweight. Relative to full-sized aircraft small ornithopters have low visual signatures, high maneuverability and low-cost manufacturing, maintenance, and storage. At present, the smallest mission-capable ornithopters are hummingbird-sized and some are hover-capable [3.5], which enables effective operation in cluttered environments and even indoors. Stealthy “low-and-slow” flight capability makes ornithopters ideal for discreet target-tracking and for some military intelligence, surveillance and reconnaissance missions, in addition to various law enforcement and civilian applications.

There are many reasons why it makes sense to look to biological fliers for ornithopter design inspiration. Leonardo da Vinci was perhaps the first human to dabble in ornithopter design, about 500 years ago [3.6], but nature has been iteratively designing flapping-wing fliers since insects

first evolved flight about 350 million years ago [3.7]. Skillful flight can be survival-advantageous to an animal so there exists a plethora of remarkable flapping-wing animals of various taxa which, relative to human-designed ornithopters of a similar scale, possess incredible maneuverability, range, endurance and flight speed [3.8-3.10].

The 10-15cm wingspan range is occupied by many accomplished fliers, including birds, bats and insects. Birds have wingspans as low as 6.5 cm (*Mellisuga helenae*), bats have wingspans as low as 15 cm (*Craseonycteris thonglongyai*), and insects have wingspans up to 30 cm (*Thysania agrippina*). Insects provide a particularly appealing biological basis for practical ornithopter design because insect flight muscles are situated only within their bodies and at the base of their wings [3.11], while flight muscles for birds and bats are distributed more broadly, increasing the complexity of wing-actuation and enabling motion about wrists and elbows [3.1]. Accordingly, insect-inspiration is likely to result in relatively simple ornithopter wing and wing-actuation designs.

There is a large body of existing research on the locust *Schistocerca gregaria* due to its potential to swarm and devastate agricultural crops [3.13-3.18]. This study focuses on *Schistocerca americana* (Fig. 1), which is closely related and morphologically similar to *Schistocerca gregaria*.



Fig. 1. *Schistocerca americana*

During swarm migration *Schistocerca gregaria* has an average airspeed of 3.8 – 4.3 m/s, a flight duration between 9 and 20 hours and a range of up to 200 km/day [3.13]. During flight insect metabolic rate increases 50-100 fold [3.19]. Weis-Fogh found in [3.20] that locust metabolic rate increases almost linearly from 41 kcal/kg/hr at 50% relative lift to 110 kcal/kg/hr at 170% relative lift. Accordingly, the metabolic rate may be expressed as:

$$M_R \cong (66.9 \cdot L_R + 14.25) \frac{\text{watt}}{\text{kg}} \quad (1)$$

Relative lift, L_R , is lift as a proportion of body weight and it may range from 50% to 170% (0.5 – 1.7). Equation 1 predicts that a cruising 2.1 gram locust should use energy at a rate of approximately 0.17 watts.¹

Locusts have two sets of wings: fore and hind. Forewings are relatively tough; during terrestrial locomotion they provide a protective covering for the more delicate folded-in hindwings. Forewings are flapped less vigorously than hindwings and their kinematics have greater variation between individuals [3.22]. Forewings are slightly longer, but hindwings have significantly greater planform area and play a more significant role in aerodynamic force production, accounting for approximately three-quarters of total lift and thrust [3.18]. Hindwings are, therefore, of greater interest for biologically-inspired design. Hindwings have multiple veins running throughout with longer veins running radially from the root of each wing toward its periphery (Fig 1). The space between veins is occupied by a transparent membrane.

Wing-extended pre-strain causes hindwings to naturally fold-in when relaxed and so they must be actively pulled-open to fan-out by applying torque about the wing-base. This torque is directly related to hindwing deployment angle; from previously published data [3.23] a bilinear estimate of applied lagging torque (in Nm) versus deployment angle (in deg) has been formulated by the present authors and is given in Equation 2 (corresponding wing-size was not specified).

$$\tau_F \approx \begin{cases} 1.6 \times 10^{-6} \theta & 0 \leq \theta \leq 50 \text{ deg} \\ 1.3 \times 10^{-5} \theta - 5.7 \times 10^{-4} & 50 \leq \theta \leq 80 \text{ deg} \end{cases} \quad (2)$$

¹ Recent work [3.21] on *Locusta migratoria* found that mass-specific metabolic rate during tethered flight is $1032 \pm 69 \mu\text{molO}_2/(\text{g} \cdot \text{h})$ (with mean max lift $95 \pm 8\%$ of body weight). Assuming standard temperature and pressure and $4.7 \pm 0.4 \text{ kcal}$ released per liter of O_2 $M_R = 126.1 \pm 12.5 \text{ watt/kg}$. Equation 1 predicts $77.8 \pm 19.6 \text{ watt/kg}$ for *Schistocera gregaria* at $L_R = 0.95 \pm 0.08$.

Hindwing shape is governed by interaction between aerodynamic, inertial [3.2] and elastic forces [3.24]. Wing deformation may play a significant role in insect wing actuation. Paraphrasing Raney and Slominski [3.26] referring to Dudley [3.27], wing deformation is sensed by dome-shaped organs concentrated near the wing base, called *campaniform sensillae*. These organs generate neuromuscular stimulus at wing oscillation frequency, which is essential for saving energy.

For insect wings, Combes and Daniel [3.28] found that spanwise flexural stiffness is 1-2 orders of magnitude larger than chordwise flexural stiffness. From the cross-section of a locust hindwing vein depicted in Fig. 3 of Ref. 3.29 the present authors have estimated vein outer width to be approximately 140 microns and vein outer height to be approximately 300 microns with an average wall-thickness of approximately 9 microns. Smith et al. [3.30] found that the mean thickness of the membrane material in the remigium (anterior hindwing region) is $3.7 \pm 1.2 \mu\text{m}$ and for the anal fan (proximal posterior hindwing region) it is approximately $1.7 \pm 0.9 \mu\text{m}$.

Locust hindwing membrane consists of ultra-thin insect cuticle and its material properties have been experimentally determined [3.30]. At 75% relative humidity the mean modulus of elasticity for the remigium is $9.9 \pm 3.5 \text{ GPa}$ while for the anal fan it is $3.7 \pm 2.7 \text{ GPa}$. Ultimate tensile stresses and strains were not explicitly stated in Ref. 3.30 but one may infer from presented data that the remigium membrane can withstand stresses of at least 35 MPa and strains of at least 0.0033 while vannus membrane can withstand stresses of at least 50 MPa and strains of at least 0.0068. Data was presented for one membrane specimen that was tested for humidity-

effects determination. The specimen did not fail up to a stress of 100 MPa [3.30]. Poisson's ratio has not, to the authors knowledge, been determined for locust hindwing membranes.²

Many natural fliers are capable of multi-mode locomotion (flying, walking, crawling, swimming, hopping, jumping, climbing, etc.) and may fold-up or wrap-up their wings when not in use, like birds and bats. Similarly, most flying insects (the Neoptera) flex their wings laterally against their abdomens during periods of rest and terrestrial locomotion [3.27]. For some ornithopters a wing-folding mechanism and integration of an additional means of locomotion may be worthy of consideration.

Natural fliers use stored chemical energy to power flight muscles while MAVs typically use lithium-polymer (Li-Po) batteries for the same purpose. Unfortunately, as Michelson and Naqvi note [3.32], "The energy density of the best battery technologies currently available still cannot match that which is locked chemically in various compounds such as sugars." Accordingly, modern ornithopter designers might consider novel approaches to energy storage. At least one group of contemporary designers has used chemically-fuelled (high-concentration hydrogen peroxide) motors that do not involve combustion (the Reciprocating Chemical Muscle, U.S. Patent No. 6,446,909).

Wing design is another important area of interest. Nature suggests that ornithopter left and right wings should be symmetric and should connect to the fuselage only near the root of their leading-edge spars, which allows root airfoils to pitch independent of the body. Nature also

² The membrane of a beetle's hindwing has been tested and Poisson's ratio was between 0.63-0.73 in the chordwise direction and 0.33-0.39 in the spanwise direction [3.31].

suggests a membrane-batten design, with a stiff leading edge spar in addition to radially-oriented stiffening elements, as observed in locusts.³

The wing kinematics of locusts can be referenced to infer appropriate kinematics for ornithopters of a similar scale. During “normal flight” locusts tend to move their wings with a high degree of symmetry, which includes flapping, pitching, and lagging. These rotations affect pronation, supination, membrane tension, etc. In addition to the aforementioned rotations, locust wing kinematics also involve significant deformation due to inertial and aeroelastic effects. Nevertheless, it is possible to approximate complex wing kinematics using a simple system composed of a single motor and transmission mechanism [3.33-3.36]. To facilitate iterative experimental optimization one may consider designing wings for easy wing-root hinge-swapping, which may enable experimental “fine-tuning” of a particular wing design for one or more flapping-systems.

Experiments conducted on flexible wings have shown that maximum thrust is achieved when flapping and pitching motions are in phase and maximum thrust-to-power ratio occurs when pitching lags flapping by 90 degrees [3.37]. For maximum thrust-to-power ratio the ratio of wing-bending natural-frequency to wing-torsional natural-frequency should be slightly less than two and the ratio of flapping frequency to wing-pitching natural-frequency should be approximately 0.5 [3.37].

For many insects gentle maneuvers are primarily controlled by tilting the stroke plane.⁷ Such control mechanisms may be useful, and are relatively easy to implement with inclusion of an empennage featuring control surfaces similar to those of conventional fixed-wing aircraft (e.g. an elevator and rudder) [3.38]. More aggressive maneuvering is common for natural flapping-

³ A membrane-batten wing design is also observed in hummingbirds, whose primary quills radiate outward from the shoulder region of their wings [3.11].

wing fliers, but is largely enabled by independent control of two-to-four wings and dramatic asymmetry in wing kinematics. Because insects do not generally have ‘tails’ it is instructive to consider tailless control, a feature that has been implemented on an existing free-flight ornithopter [3.5], and the entomopter [3.9].

Ornithopter size is often specified in terms of wingspan, b . Liu and Moschetta [3.40] derived an empirical relationship between wingspan and mass based on eight different ornithopters with spans from about 10 to 120 cm. This relationship (with mass in kilograms and wingspan in meters) is given in Equation 3. Wing area is estimated given an assumed aspect ratio, where aspect ratio is treated as an independent variable [3.4].

$$m \approx 0.240 \cdot b^{1.84} \quad S = b^2 / AR \quad (3)$$

Pennycuik [3.42] has derived scaling relationships for flapping frequency and minimum power speed (Equation 4).⁴

$$f = c_1 \frac{m^{1/3} g^{1/2}}{b \cdot S^{1/4} \rho^{1/3}} \quad V_{P_{\min}} = c_2 \frac{m^{1/2} g^{1/2}}{b \cdot \rho^{1/2}} \quad (4)$$

To estimate cruise power consumption one may scale the power consumption of existing ornithopters according to mass or use Equation 1 after adjusting for the greater relative power consumption of artificial fliers (based on the Nano Hummingbird [3.5] a relative efficiency factor of approximately two may be appropriate).

Ellington [3.7] found that the maximum straight-and-level airspeed (dash speed) for flapping-wing fliers is limited by advance ratio, as with propellers, and that maximum advance ratio is approximately one. Accordingly, an upper-limit to dash speed may be given by:

$$V_{\max} \approx 2R \cdot \Phi_{\max} f_{\max} \quad (5)$$

⁴ Values for c_1 and c_2 are unitless and have been estimated as $c_1 \approx 1.08$ and $c_2 \approx 0.88$ using scattered data for 32 bird species [3.42].

Maximum climbing rate can be estimated using known dash speed and known stroke-averaged maximum lift coefficient, which may be estimated using data taken from natural or artificial wings of a similar scale and design. Note that structural dynamics do not scale in the same manner as fluid dynamics [3.24].

A traditional method of producing membrane-batten flapping wings is to use a carbon rod for the leading edge spar, carbon rods or music wire for ribs, and Mylar[®] for the membrane. Components are joined using rubber cement, epoxy and/or wound Kevlar thread with a drop of cyanoacrylate glue. Properties for membrane-appropriate materials are provided in Table 1 (Shrilk is a new material inspired by insect cuticle) [3.45].

Table 1. Membrane material summary [3.30, 3.43, 3.44, 3.45]

	Locust Wing Membrane ¹	Mylar ²	Shrilk ³
t (μm)	0.8 – 4.9 remi ~ 3.7 fan ~ 1.7	≥ 2	-
ρ (kg/m^3)	~ 1200 (1100 - 1400)	1400	1460
E (GPa)	0.3 – 18.7 remi ~ 9.9 fan ~ 3.7	3.8	-
σ_u (MPa)	> 100 remi > 35 fan > 50	MD 186 TD 234	dry ~ 119 wet ~ 3.5
ε_u	remi > 0.003 fan > 0.007	MD 1.10 TD 0.80	dry ~ 0.04 wet ~ 0.23

¹ At ~ 75% relative humidity of surrounding air

² Mylar values based on 12 μm thickness data [3.43]

MD = Machine Direction, TD = transverse direction

³ Shrilk values based on 1:2 ratio of chitosan and fibroin

Table 2 provides tabulated properties for common materials that serve similar structural roles to locust wing veins, at least for traditionally-constructed ornithopters. To the authors knowledge there is no reliable material property data that has been published for locust wing veins.

Table 2. Vein material summary [3.44, 3.46-3.48]

	Carbon Rod ²	Music Wire ³	Kevlar Thread ⁴
d (μm)	≥ 250	≥ 130	≥ 150
ρ (kg/m^3)	1500	7850	1440
E (GPa)	tensile 141 comp 138	210	83
σ_u (MPa)	tensile 2410 comp 1930	1590-2750 (yield)	3600
ε_u	0.017	-	-

¹ Veins are tapered and amorphous; approx. diameter value is highly variable

² Graphlite, quoted properties for 67% fiber volume

³ ASTM A228

⁴ Kevlar 29 resin-impregnated strand (filament diameter 12 μm , 1000 total filaments – total strand diameter $\sim 670 \mu\text{m}$). Properties for other fiber/matrix compositions published elsewhere.

Some non-traditional wing construction methods rely on CAD models that may be generated using techniques like white light interferometry [3.49] and x-ray microtomography [3.50], as well as embedding and sectioning. From CAD models it is possible to fabricate features of a natural wing in minute detail, which may be done using a variety of processes including: electric discharge machining, laser micromachining [3.49, 3.50], micro CNC, various MEMS microfabrication techniques [3.51,3.52], and rapid-prototyping techniques including: multi-jet modeling, stereolithography and selective laser sintering. For complex high-resolution wing models we recommend embedding and sectioning to inform wing design with micro-CNC

fabrication of a mold or template to be used for wing construction. This combination provides high resolution, a wide array of material selection options, and relative cost-effectiveness.

3.2. Experimentation

It is observable that natural flapping-wing fliers outperform existing ornithopters by nearly every metric, but nature works within different constraints. As a result several questions are raised, including how one should best-pursue small ornithopter design, whether or not biomimicry is a worthwhile pursuit, how dependent wing kinematics are on active-actuation versus passive deformation, whether sophisticated wing actuation or sophisticated wings should be the design priority, etc. This study will present experimental data that should contribute to answering such questions.

The desert locust, *Schistocerca gregaria* is a potentially harmful pest not native to the United States and it is subject to import restrictions [3.53]. Therefore, the locust *Schistocerca americana* was used for the biological experimentation performed in this study. An adult locust was selected from a group of locusts shipped from Houston, Texas by our collaborators at Baylor College of Medicine. The locust's mass, body length and hindwing-span are 2.42 grams, 50.0 mm, and 131.2 mm, respectively. This locust was used for kinematic and force studies.

In addition to the locust, three artificial wings were also used as experimental subjects. The artificial wings were designed to approximate the size, sweep, planform shape, and structure of fully-deployed locust hindwings. To produce the wings a *Schistocerca americana* hindwing was pulled-forward until fully-deployed and then glued-open at its root. The wing was speckled with an array of dots whose coordinates were determined with the help of a custom 99-point calibration plate. Using the coordinates a CAD surface model of the wing was created and simplified, from which a paper template was produced and used to construct all artificial wings

(Fig. 2). Consequently, all wings are uniform in planform shape, size, stiffening-element angles, and sweep angles. All artificial wings have approximately the same spanwise leading-edge stiffness, but intentionally varying chordwise stiffness.

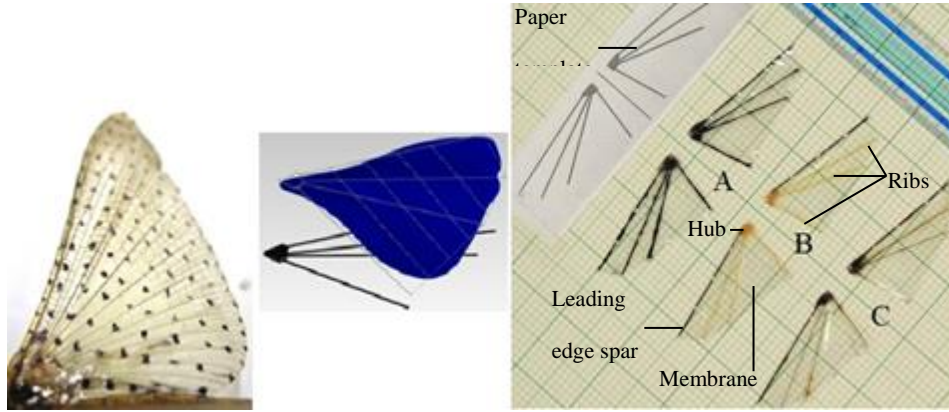


Fig. 2. Wing design: locust wing (left), CAD model (middle), artificial wings (right);

A. Rigid B. Semi-Rigid C. Semi-Flexible

All of the leading-edge spars are carbon fiber rods of constant 250 micron diameter. Membranes are made from a 5 micron thick sheet of Mylar[®]. Each artificial wing has a hub at its leading-edge root with three ribs radiating outward from each hub (Fig. 2, right). Ribs are glued to both the membrane and the hub, effectively providing a radial array of cantilever beams. Materials were varied to alter chordwise stiffness, as described by Table 3. Masses are given in milligrams as single-wing mean values (averaged between left and right wings).

Table 3. Artificial wing information

Art. Wing	Hub	Adhesive	Ribs (dia.)	Mass (mg)
Rigid	Balsa Wood	Speaker Cement	Carbon Rod (250 μ m)	40.3
Semi- Rigid	Balsa Wood	Epoxy	Kevlar Thread (150 μ m)	31.2
Semi-Flexible	Fiberglass	Rubber Cement	Music Wire (130 μ m)	33.6

Speaker cement was used to glue ribs to hubs and to glue hubs to membranes for Wings A and B. All Kevlar[®] thread was immersed in rubbing alcohol and thoroughly cleaned to remove the factory coating prior to epoxy or rubber cement application. Table 4 compares nominal geometric parameter values between the artificial and natural wings used in this study.

Table 4. Locust and artificial wing geometric parameters

Parameter	Artificial	Locust
Wing Length (mm)	49	45.8
Max chord length (mm)	24	22.8
Planform Area (cm ²)	15.8	16.2
Aspect Ratio ($4R^2/S$)	6.1	5.2

To enable kinematic point-tracking using high-speed cameras, markers consisting of white spots with concentric black dots were added to the locust's hindwings. Markers were placed at the leading and trailing edges of each wing, including the wingtips, as depicted in Figure 3.



Fig. 3. Preparation for kinematic point-tracking

The artificial wing experimental setup is shown in Fig. 4; it consists of two Phantom v9.1 high-speed video cameras, two halogen floodlights, a six-component microbalance, two

transmissions, a National Instruments data-acquisition system with LabVIEW, and a laser tachometer (not shown).

The two Phantom v9.1 cameras acquired video at 2000 frames per second to obtain approximately 130 images per flapping cycle at a resolution of 800×600 pixels. To match video and force data a manual trigger was setup, which initiated video recording while simultaneously sending a square-wave pulse to the seventh channel of the data acquisition system. There is effectively no delay between the manifestation of the pulse in the force data and the first captured frame of video (negligible delay was verified onsite using an LED wired to the trigger).

A custom calibration plate was designed and constructed for video point-tracking. The calibration plate was modeled using Solidworks; it was created using a 3D printer with 15 micron layering. The calibration plate spanned the volume of all flapping wings.

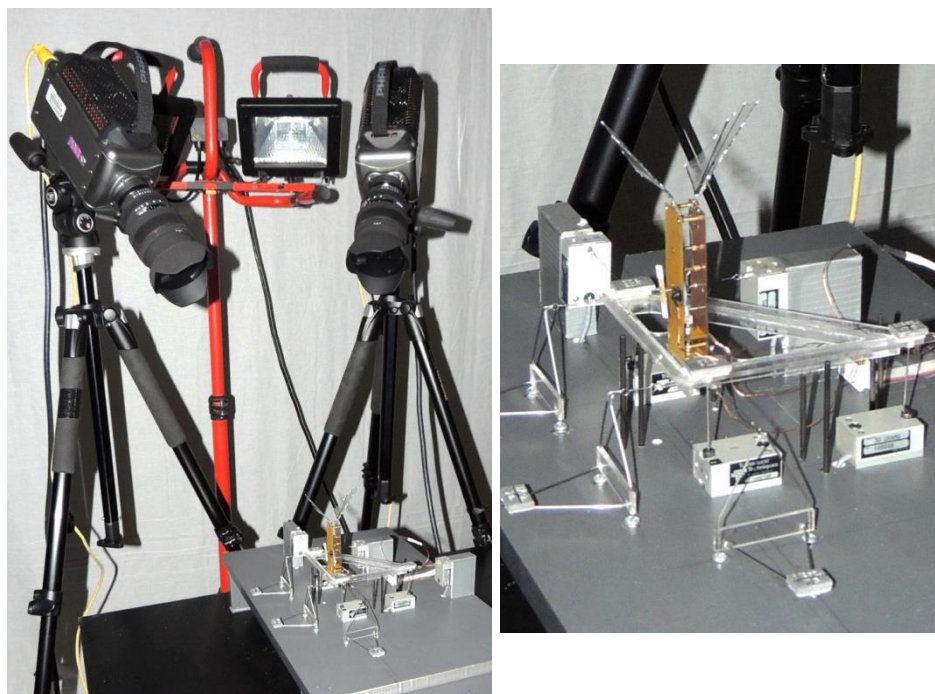


Fig. 4. Experimental setup.

A sensitive, custom-built 6-component microbalance has been used in the study (see Fig. 4). It consists of a platform that rests on three load cells, which measure lift. Three additional load

cells are connected to the platform to measure thrust and side force. The load cells (Transducer Techniques, Model GSO-30) are capable of measuring forces as small as two milligrams.

To calibrate the microbalance each cell was loaded with a series of known weights. A 6x6 calibration matrix was generated and then checked by applying various loads at various locations and in different directions.

Two wing-actuating transmissions were designed and constructed in-house. They convert a uniform continuous rotation of the electric motor into harmonic oscillations of the wing arms and, consequently, of the wings. The transmission consists of a crank, connecting rods, hinges, and wing arms (Fig. 5). The first transmission is a strictly-flapping transmission with a no-load flapping-amplitude of 85 degrees. The second transmission has approximately the same no-load flapping amplitude, but it combines active flapping with active pitching. Its no-load pitching amplitude is approximately 60 degrees (± 30 deg).

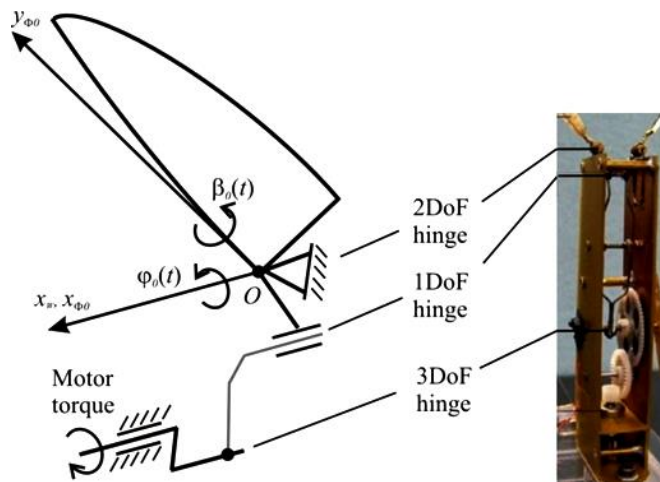


Fig. 5. Schematic of flapping-pitching transmission.

Each artificial wing was carefully attached to the transmissions using CA glue, such that rest wing pitching-angles were approximately zero and design sweep-angle was approximately preserved (7.7 deg). For locust experimentation the locust had to be temporarily tethered to a sting mounted to the balance, without harming the locust. To achieve this, the locust was gently

held with multiple layers of ultra-soft tissue such that its legs were restrained and its ventral pterothorax exposed. Next, a rectangular rare-earth micromagnet ($6 \times 3 \times 1$ mm) was fixed to the locust using cyanoacrylate glue, as depicted in Figure 6.



Fig. 6. Magnet attached to the plastron of the pterothorax

Laboratory temperature, pressure and density were measured to be 25.6°C , 94325 Pa, and 1.10 kg/m^3 , respectively. Tested wings were flapped at between 10 and 26 Hz, in increments of 2 Hz. Five test runs were performed for each condition and balance signal data was recorded for 25 seconds per test run at a sampling rate of 1000 Hz. Force data were stroke-averaged and left unfiltered. Uncertainty analysis was performed on five sets according to the Students t-distribution chart (four degrees of freedom and a certainty level of 95%).

The reference frame, B , for tracking point-coordinates is referred to as the body-fixed reference frame $x_B y_B z_B$. The body-fixed reference frame used in this study has an origin O , which is attached to the pivot point of a wing. The x_B -axis is parallel to the longitudinal axis of the body and directed forward; the y_B -axis is normal to the plane of symmetry and rightward; the z_B -axis is normal to the lateral plane and downward (Fig. 7).

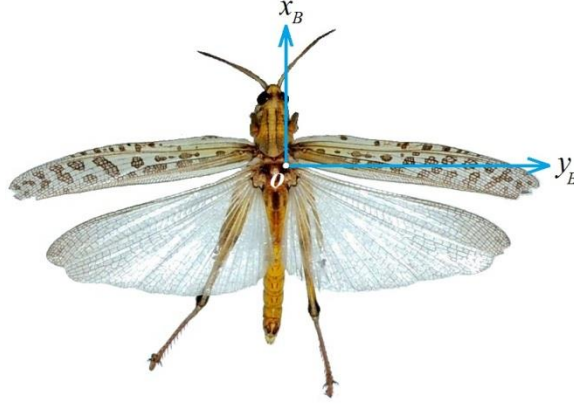


Fig. 7. Body-fixed reference frame

All kinematic parameters can be calculated from the coordinates of the tracked points, as described by Lim et al. [3.54]. The motion of a flapping wing is primarily referenced with respect to the flapping plane $y_W z_W$, depicted as a light grey plane in Figure 8 (left). The flapping plane may also be referred to as the stroke plane and it is defined by three points in the body-fixed frame: the pivot point of the wing, O , the highest point of the wingtip's trajectory, H_W , and the lowest point of the wingtip's trajectory, L_W . The x_W -axis is perpendicular to the stroke plane. The y_W -axis is the intersection of the stroke plane and the lateral plane, $x_B y_B$.

The transformation from the body-fixed coordinate system, B , to the flapping coordinate system, W , is obtained by the sequence of two rotations: (1) about the y_B -axis by the angle of inclination, Θ , and (2) about the z_B -axis by the angle of sweep, Λ . Thus, the angle of inclination is the angle between the z_B -axis and the z_W -axis; it is defined as positive counterclockwise about the y_B -axis. The sweep angle is the angle between the y_B -axis and the y_W -axis; for the right wing it is defined as positive counterclockwise about the z_B -axis while for the left wing it is defined positive clockwise.

The stroke plane is used to define the flapping and pitching angles. The flapping angle, ϕ_i , is the angle between: (1) the y_W -axis, and (2) the vector connecting the wing pivot point to the

Motion for flapping insect wings includes: articulated rotation about the wing-base, elastic deformation of the membrane, and elastic deformation of veins. There is a problem inherent to the study of insect-like flight: decoupling of active wing-rotation (at the base) and passive wing deformation (throughout the structure). To address this issue the flapping-wing kinematics of a tethered locust were examined. Locust wing kinematics were characterized and then artificially approximated via the design of a flapping transmission and an active pitching-flapping transmission, as described in Section 4.

Locust hindwing kinematics were studied using high-speed video recordings in still air. The tethered locust flapped its wings at 15.8 Hz, which is lower than the 20-27 Hz observed in freely-flying locusts [3.55, 3.56]. For the tethered locust, its stroke plane inclination and retraction angles were 14.6 and 38.7 degrees, respectively.

Video recordings were analyzed for two right-hindwing sections. The first section was located at $0.2R$ outboard of the wing-base, and the second section was located at $0.5R$. Curve-fitting was applied to kinematic data using a three-term Fourier series approximation for flapping angles and a six-term approximation for pitching angles; these representations closely track the kinematic behavior of membrane-batten wings [3.57]. In the present case, 126 data points were used to generate each kinematic curve. The overall average displacement of data points from curve-fits was 2.2 degrees.

Curves for locust flapping and pitching angles are presented in Figs. 9 and 10, respectively. Flapping amplitude at the 20% section is 98 degrees, which is 4 degrees lower than the 50% section. Flapping amplitude is estimated to be 95 degrees at the wing root, based on linear extrapolation using known values. The flapping-wing dihedral angle is five degrees.

Sectional pitching amplitudes at 20 and 50% span differed significantly: 86 and 107 degrees, respectively. Linear extrapolation from these values to the wing base yields an estimated 72 degree pitching amplitude. Pitching angle leads flapping angle by approximately 0.1 period. The

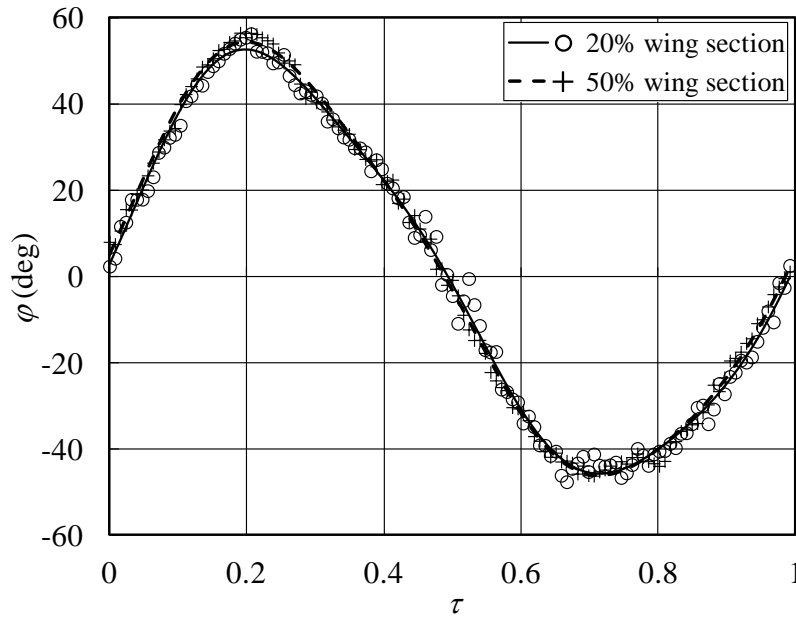


Fig. 9. Locust hindwing flapping angle through one flapping cycle.

(Symbols: data, Lines: approximation)

time-varying pitching angle exhibits a significant second harmonic. The amplitude of the second harmonic is about 0.2 times the amplitude of the first harmonic.

Force-measurement experiments were conducted to investigate the effect of flexibility and active-pitching on the aerodynamic performance of flapping wings. Aerodynamic forces generated by the three artificial wings were measured using a custom-built six component balance, which is depicted in Figure 4. Two transmissions were used to actuate the wings: a flapping transmission and a pitching-flapping transmission, which features active pitching at the wing base ($\pm 30^\circ$); otherwise both transmissions have comparable kinematic parameters. Small carbon wedges were used to change transmission no-load flapping dihedrals to approximately 5

degrees to match locust values. Both transmissions were constructed with a stroke-plane inclination angle of zero degrees, but aerodynamic forces were transformed such that reported forces correspond to an effective inclination angle of 14.6 degrees. The transformation is justified by the fact that all tests were conducted at zero freestream velocity. All artificial wings were attached to the transmission such that their pitching angles were near-zero under no aerodynamic loading. Kinematic angles are summarized in Table 5.

Table 5. Kinematic angle comparisons

All values in degrees and referenced to the wing base	Flapping Transmission (no-load)	Pitching-Flapping Transmission (no-load)	Locust* (loaded)
Flapping amplitude	85	85	95
Flapping dihedral	5	5	5
Pitching amplitude	0	60	72
Inclination angle	14.6	14.6	14.6

*Locust values were obtained experimentally

Unfiltered force results were stroke-averaged over a period of 25 seconds; each test was repeated five times. The following plots include error bars (upper half shown) with a 95% certainty level.

Figure 11 compares the lift performance of the artificial wings on the flapping transmission. All three wings generate greater lift with greater flapping frequency up to approximately 20 Hz; beyond 20 Hz the lift-curve flattens, except for the Rigid wing. Lift measurements for the tethered locust are included in Figure 11, at its 15.8 Hz wing-beat frequency. Its hindwing contribution to aerodynamic force production is assumed to be 75% of the total, as suggested by Ref. 3.22. Locust hindwing lift is 24.8% larger than that of the Semi-Flexible wings.

Figure 12 presents thrust performance for the artificial wings on the flapping transmission. Thrust increases quadratically with increasing frequency over the tested domain. Also, there is a positive trend between thrust and decreasing chordwise flexibility.⁵ Locust hindwings generated 9.7% more thrust than the Semi-Flexible wings; the Semi-Flexible wings outperformed other artificial wings.

The Semi-Flexible wings, which were the best performing wings on the flapping transmission, were also tested on the pitching-flapping transmission. Below 20 Hz the Semi-Flexible wings

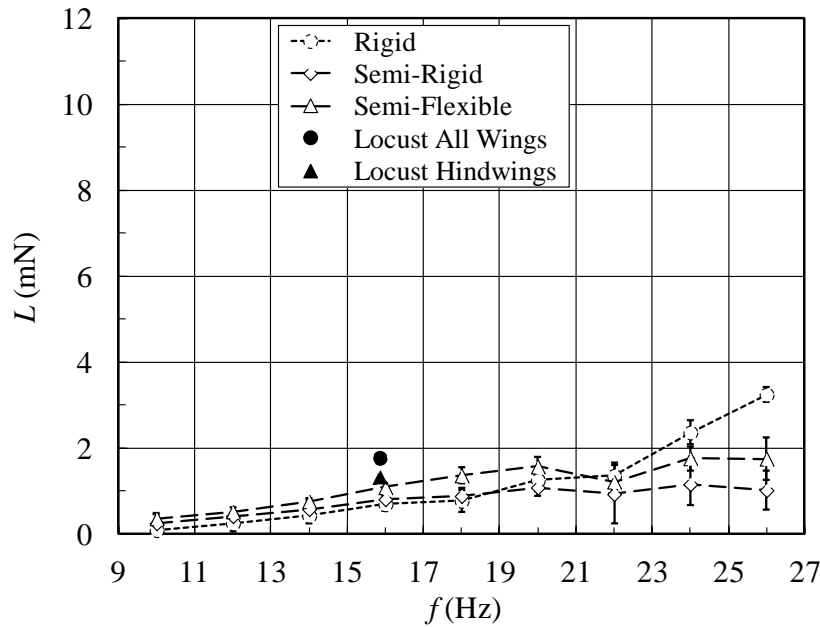


Fig. 11. Wing lift on flapping transmission.

generate greater lift on the flapping transmission than on the pitching-flapping transmission, as seen in Fig. 13.

For the Semi-Flexible wings the pitching-flapping transmission produced more thrust below 20 Hz but at frequencies above 20 Hz the flapping transmission produced greater thrust. With

⁵ The trend between thrust and chordwise flexibility breaks down when wings are excessively flexible, which has been demonstrated for similar wings actuated differently [3.58].

active-pitching at 15.8 Hz the Semi-Flexible wings generate 10.0% greater thrust than locust hindwings (Fig. 14).

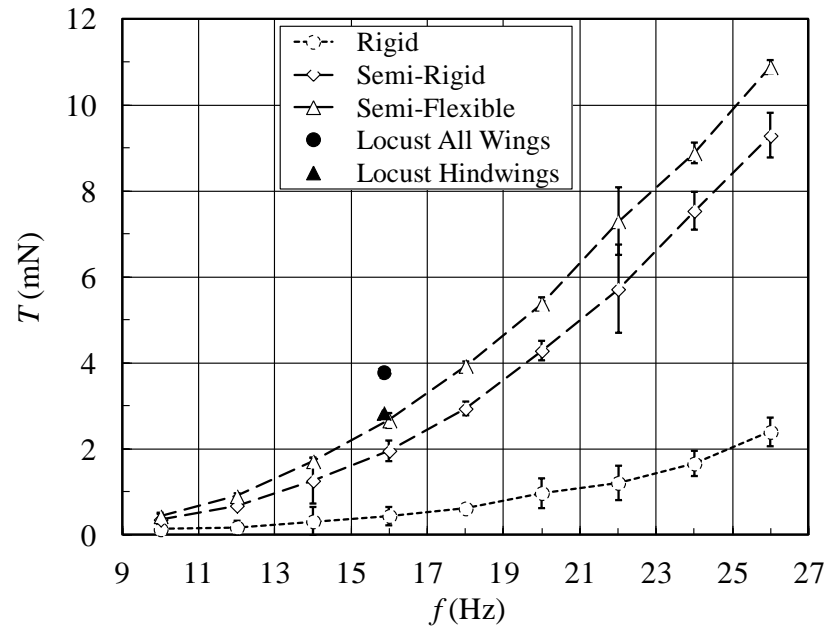


Fig. 12. Wing thrust on flapping transmission.

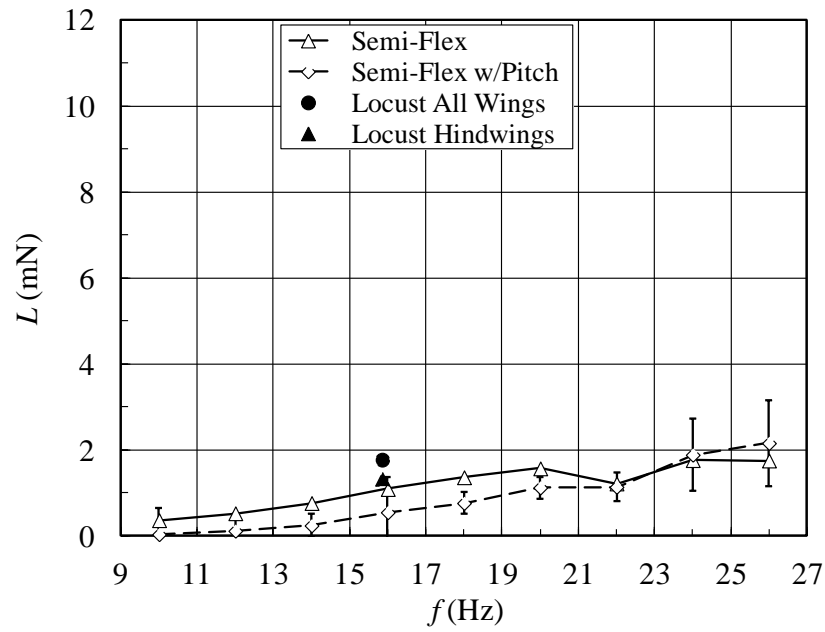


Fig. 13. Wing lift for Semi-Flexible wing on flapping and pitching-flapping transmissions.

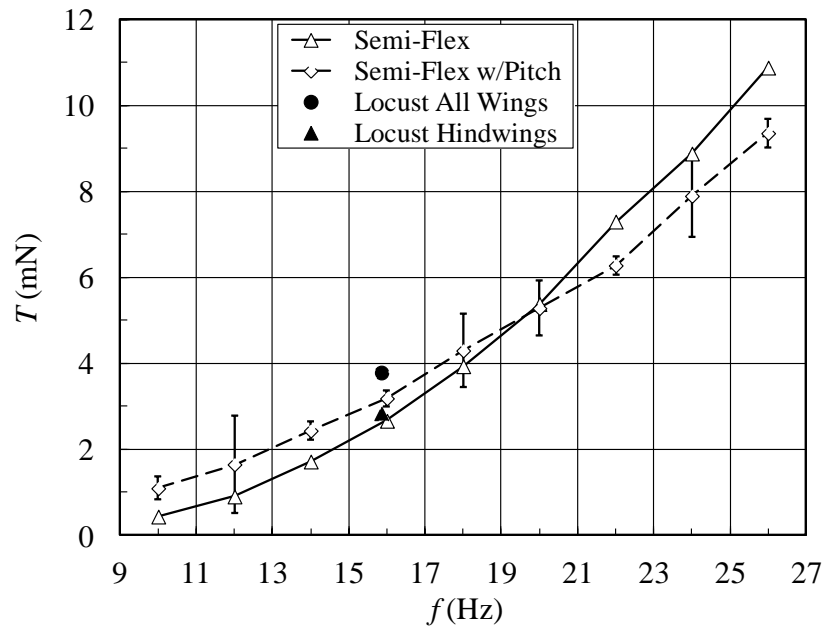


Fig. 14. Wing thrust for Semi-Flexible wing on flapping and pitching-flapping transmissions.

3.3. Ornithopter Design and Specifications

The biological literature review shows nature's preference for membrane-batten wing designs at the 10-15 cm scale. The study of locust hindwing kinematics suggests that wings should be spanwise stiff, chordwise flexible, and capable of large-amplitude pitching near their roots. Stroke-averaged thrust experiments demonstrated that traditionally-constructed artificial wings can be comparable in thrust-performance to natural wings, even on a single-DOF transmission.

A radio-controlled (RC) ornithopter was designed in accordance with these observations; it has a chosen wingspan of 14-cm, an aspect ratio of 3.2 and an active flapping amplitude of 72 degrees. The compact flapping-wing ornithopter is electrically-powered with counter-rotating cranks and a fin located beneath its horizontal stabilizer. Its leading edge spars are swept-forward 15° to allow for greater wing area without increasing span. Figure 15 provides images of the ornithopter; Tables 6 and 7 provide various ornithopter specifications.

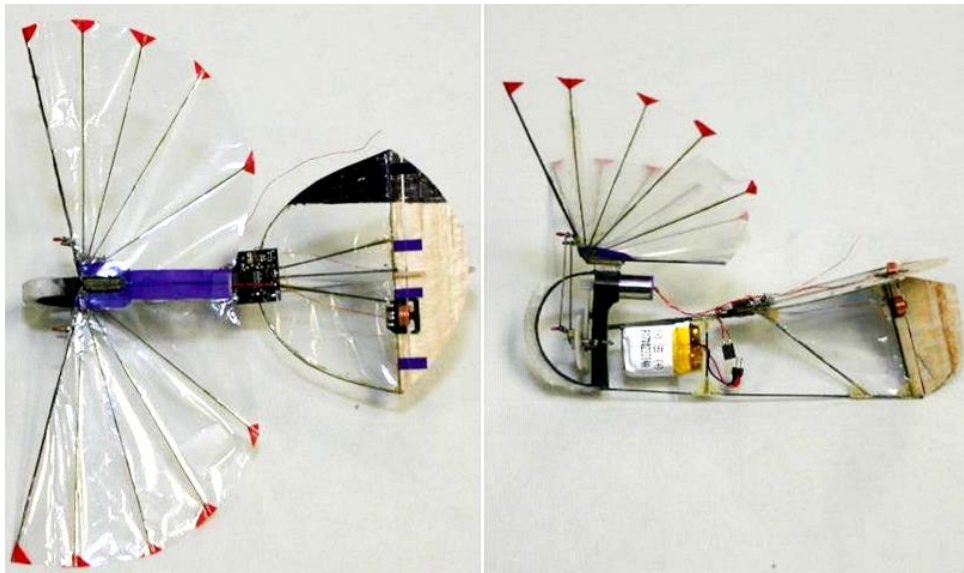


Fig. 15. Top and side views of the 14 cm radio-controlled ornithopter.

Table 6. Ornithopter specifications

Parameter	
Length (nose-to-tail)	14 cm
Height (top-to-bottom)	4.5 cm
Wingspan (tip-to-tip)	14 cm
CG location aft of wing pivot	1.8 cm
Wing Area	62 cm ²
Horizontal Tail Area	25 cm ²
Vertical Tail Area	13 cm ²
Flapping Amplitude	72 deg
Wing Dihedral Angle	~ 20 deg
Cruise Speed	~ 3 m/s
Cruise Flapping Frequency	20-23 Hz

Table 7. Ornithopter Components

Component	Description	Mass, gram
Flapping wing	0.3-0.5mm carbon rods	0.24
Tail assembly	0.3mm carbon rods	0.70
Gearbox	Didel M0.30mm gears	1.27
Electric motor	7mm Super Slick 2.2 Ohm	2.87
Actuators	Plantraco HingeAct	0.50
RC receiver	Deltang RX43	0.28
Battery	80mAh 3.7V Li-Po “Full River”	2.30
Total		8.16

The wing of the ornithopter is essentially a single-piece; its membrane is constructed from one sheet of 2 μm thick Mylar whose area density is 1.8 grams/m². The membrane is supported by various spars that radiate outward from the wing base. A single spar runs longitudinally; it is flexible and it is not fixed to the fuselage. Accordingly, the trailing-edge of the wing is free to oscillate up-and-down, which produces additional thrust. Because the leading-

edge must be relatively stiff its spar diameter is 0.5 mm, whereas all other spars have 0.3 mm diameter.

The flapping transmission of the 14-cm ornithopter utilizes two counter-rotating cranks, as seen in Fig. 17. The left crank is actuated by an electric motor through a two-stage gear box with a gear ratio of 27.7-to-1. The left and right cranks have mutually contacting wheels with the same number of teeth. Thus, the right crank rotates opposite the left crank, which eliminates reaction torque associated with longitudinal/transverse arrangements of a single crankshaft. The ornithopter flapping transmission is powered by a Super Slick 2.2 Ohm coreless electric motor and a 3.7 V, 80 mAh lithium polymer battery.

The fin of the 14-cm ornithopter is installed on the bottom surface of the horizontal stabilizer. The horizontal stabilizer and fin are made of 0.3 mm carbon rods, and covered with 2 μm thick Mylar. The elevator and rudder are made of balsa wood that is 0.3 mm thick. The fuselage is constructed using 0.5 mm carbon rods.

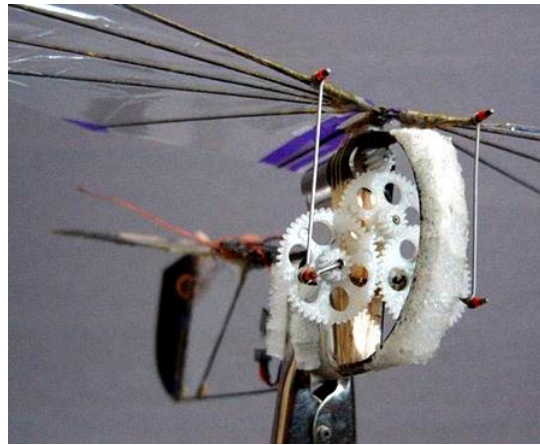


Fig. 17. Flapping transmission of the 14-cm ornithopter.

During its first flight test the 14-cm ornithopter suffered from inefficient pitch-control and near-zero climbing rate. These problems were due to an excessively-forward center of gravity, which was selected based on previous 25-cm designs. After adjusting the center of gravity the

ornithopter flew well. It demonstrated an ability to: withstand winds up to 3 m/sec, perform a series of sharp turns without losing altitude, and maintain a flight duration in excess of 2 min at moderate throttle. Figure 18 depicts the 14-cm ornithopter in-flight.



Fig. 18. The 14-cm ornithopter in flight (photos courtesy of Dr. P. Wu).

With $\rho = 1.1 \text{ kg/m}^3$ Section 3.2 equations predict: $m = 6.4 \text{ grams}$, $S = 61 \text{ cm}^2$, $f = 15.6 \text{ Hz}$, $V_{Pmin} = 1.51 \text{ m/s}$ and, assuming maximum flapping frequency is 50% higher than cruise flapping frequency, $V_{max} = 4.10 \text{ m/s}$. These estimates are in reasonable agreement with known ornithopter values.

3.4. Summary and References to Chapter 3

Locusts were selected as the basis for this study because they are the appropriate size, they fly efficiently, and they migrate long distances. The locust is also amenable to experimentation and there is a large body of existing locust research upon which to draw. A cruising 2.1 gram locust is estimated to consume energy at 0.17 watts and the locust *Schistocerca gregaria* has an average airspeed of 3.8-4.3 m/s, a flight duration of 9-20 hours, and a range of up to 200 km/day. Locust wings feature a membrane-batten design, with a stiff leading edge spar in addition to radially-oriented stiffening elements. Hindwings play a more significant role in aerodynamic force production, so they are of greatest interest with regard to artificial wing design. Flapping wing kinematics include active rotation at the wing base, as well as substantial passive deformation of the wing structure.

The particular locust selected for experimentation in this study was *Schistocerca americana*. High-speed videography was used to kinematically point-track the wings of *Schistocerca americana* while tethered in still air. Simultaneous thrust and lift forces were acquired using a 6-component microbalance. Stroke plane inclination and retraction angles were found to be 14.6 and 38.7 degrees, respectively. Hindwing retraction increases the proximity of the left-and-right hindwings at the top of the upstroke, enabling aerodynamic lift enhancement via the clap and fling mechanism. Flapping amplitude at the 20% section was found to be 98 degrees, which is 4 degrees lower than at the 50% section. Sectional pitching amplitudes at 20 and 50% differed significantly: 86 and 107 degrees, respectively. Linear extrapolation suggests active flapping and pitching amplitudes at the wing base of 95 and 72 degrees, respectively. Hindwings are relatively flexible chordwise and there is significant torsion of the overall wing structure; large sectional pitching amplitudes were observed. Passive deformation is likely

dominant with regard to observed sectional pitching, which is supported by: low extrapolated active-pitching at the wing-base, chordwise flexibility, and force similarity between the Semi-Flexible artificial wing and locust hindwings on the flapping transmission. Kinematic data was taken into account in the design of a flapping transmission for bench-top aerodynamic studies.

The fully-deployed hindwings of *Schistocerca americana* were used as the basis for designing three artificial wings with approximately the same size, sweep, planform shape, and structure. Since chordwise deformation is critical to flapping-only thrust generation the three investigated artificial wings had varying chordwise stiffness and spanwise stiffness kept approximately constant. A relatively stiff leading-edge spar was used for artificial wing construction; minimal spanwise bending of the hindwing was observed.

Two wing-actuating transmissions were designed and constructed in-house. The first transmission is a flapping transmission with a no-load flapping-amplitude of 85 degrees. The second transmission has approximately the same no-load flapping amplitude, but it combines active flapping with active pitching. Its no-load pitching amplitude is 60 degrees.

Aerodynamic forces were measured for three artificial wings using the flapping transmission installed on the microbalance. All wings generate a much smaller amount of lift than thrust, which is similar to what was observed for the live tethered locust. Results confirm that chordwise flexibility has a significant effect on the thrust-generating capability of flapping wings. Thrust performance improves significantly as chordwise-flexibility increases, but excessive chordwise-flexibility may diminish thrust at higher frequencies.

The artificial wings most efficient at generating thrust on the flapping transmission were also tested on the pitching-flapping transmission. Below 19 Hz the Semi-Flexible artificial wings produced greater thrust on the pitching-flapping transmission, whereas above 19 Hz they

produced greater thrust on the flapping transmission. At a pitching-flapping frequency of 15.8 Hz artificial wings generated 10.3% more thrust than is estimated for locust hindwings, but 18% less lift.

Wing-actuation and chordwise-stiffness studies informed the design of a radio-controlled ornithopter with a flapping transmission and a 14 cm wingspan. Specifically, membrane-batten wings were built with a relatively stiff leading-edge spar and radially-oriented membrane-supporting spars. The wings flap at a frequency of 20-23 Hz during sustained flight at moderate throttle settings. The ornithopter has demonstrated an ability to withstand moderate winds; it has a mass of 8 grams, an endurance in excess of two minutes and a cruise speed of approximately 3 m/s. Rough estimates of ornithopter parameters obtained using scaling equations agree reasonably well with actual ornithopter values.

References

- [3.1] R. C. Michelson, Encyclopedia of Aerospace Engineering, (2010).
- [3.2] Science Daily, (2010). <http://www.sciencedaily.com/release/2010/09/100922155112.htm>
- [3.3] DelFly project, TU Delft. <http://www.delfly.nl/?site=DIII&menu=&lang=en>.
- [3.4] J. Yamaleev, M. Jones, 50th AIAA Aerospace Sciences Meeting, Nashville, TN, (Jan. 2012).
- [3.5] M. Keennon, K. Klingebiel, H. Won, 50th AIAA Aerospace Sciences Meeting, Nashville, TN, (Jan. 2012).
- [3.6] J. D. Anderson, A History of Aerodynamics. Cambridge University Press, (1997).
- [3.7] C. P. Ellington, The Journal of Experimental Biology, 202, 3439 (1999).
- [3.8] D. Hansford, National Geographic News. Sep. 14th (2007).
<http://news.nationalgeographic.com/news/2007/09/070913longest-flight.html>
- [3.9] Schnell, Gary, EarthSky. May 31st (2011). <http://earthsky.org/biodiversity/fastest-bird>
- [3.10] A. Bergou, L. Ristroph, J. Guckenheimer, I. Cohen, Z. Wang, Physical Review Letters, The American Physical Society (April 2010).

- [3.11] R. J. Wootton, “Functional morphology of insect wings”, *Annual Review of Entomology*. 37, 113-140. (1992)
- [3.12] C. H. Greenwalt, *Hummingbirds*. Doubleday & Co., Garden City; ISBN 0-486-26431-9 (1960).
- [3.13] P. M. Symmons, K. Cressman, *Food and Agricultural Organization of the United Nations*, Rome (2001). <http://www.fao.org/ag/locusts/oldsite/PDFs/DLG1e.pdf>
- [3.14] Unattributed author, *National Geographic*, (Feb. 2012).
- [3.15] P. Henningsson, and J. Bompfrey, *J. R. Soc. Interface*, (2011).
- [3.16] G. Taylor, R. Zbikowski, *Journal of the Royal Society Interface*, (2005).
- [3.17] S. Walker, A. Thomas, G. Taylor, *Journal of the Royal Society Interface*, (2008).
- [3.18] M. Jensen, *Phil. Trans. R. Soc. Lond.*, B239, 511 (1956).
- [3.19] E. L. Arrese, J. L. Soulages, *Annual review of Entomology*, 55, 207 (2010).
- [3.20] T. Weis-Fogh, *J Exp Biol.*, 41, 257 (1964).
- [3.21] Snelling, E., Symour, R., Matthews, P., and White, C., “Maximum metabolic rate, relative lift, wingbeat frequency, and stroke amplitude during tethered-flight in the adult locust *Locusta migratoria*”, *Journal of Experimental Biology*, 2012
- [3.22] Conference, Austin, TX, Aug. 11-14 (2003). AIAA 2003-5345.
- [3.23] R. J. Wootton, K. E. Evans, R. Herbert and C. W. Smith, *The Journal of Experimental Biology.*, 203, 2921 (2000).
- [3.24] A. M. Mountcastle, T. L. Daniel, *Experimental Fluids* (2009).
- [3.25] S. A. Combes, T. L. Daniel, *The Journal of Experimental Biology.*, 206, 2999 (2003).
- [3.26] D. Raney, E. Slominski, *AIAA Guidance, Navigation and Control Conference*, Austin, TX, Aug. 11-14 (2003). AIAA 2003-5345.
- [3.27] R. Dudley, *The Biomechanics of Insect Flight: Form, Function, Evolution* (Princeton: University Press, 2000).
- [3.28] S. A. Combes, T. L. Daniel., *The Journal of Experimental Biology*. 206., 2979-2987 (2003).
- [3.29] R. C. Herbert, P. G. Young, C. W. Smith, R. J. Wootton, K. E. Evans, *The Journal of Experimental Biology.*, 203, (2000).
- [3.30] C. W. Smith, R. Herbert, R. J. Wootton, and K. E. Evans, *The Journal of Experimental Biology.*, (2000).

- [3.31] N. S. Ha, T. L. Jin, N. S. Goo, H. C. Park, *Bioinspiration and Biomimetics*, 6, No. 4 (2011).
- [3.32] R. C. Michelson, and M. A. Naqvi, *Beyond biologically-inspired insect flight*, von Karman Institute for Fluid Dynamics RTO/AVT Lecture Series on Low Reynolds Number Aerodynamics on Aircraft Including Applications in Emerging UAV Technology, Brussels, Belgium, November 24-28 (2003).
- [3.33] R. Mandangopal, Z. Khan, S. Agrawal, *Journal of Mechanical Design*, 127, 809 (2005).
- [3.34] R. Zbikowski, C. Galinski, C. Pedersen, *Journal of Mechanical Design*, 127, 817 (2005).
- [3.35] Z. Khan, and S. Agrawal, *AIAA Journal*, 49(7), 1354 (2011).
- [3.36] H. Tanaka, J. P. Whitney, R. J. Wood, *Integrative and Comparative Biology*, 51(1), 142 (2011).
- [3.37] K. Frampton, M. Goldfarb, D. Monopoli, D. Cveticanin, in book *Fixed and Flapping Wing Aerodynamics for Micro Air Vehicle Applications*. Vol. 195, Chapter 21, 473 (2001).
- [3.38] G. Maniar, R. Randall, S.V. Shkarayev, Z. Goff, and P. Beran, 50th AIAA Aerospace Sciences Meeting, Nashville, TN, (Jan. 2012).
- [3.39] R. C. Michelson, *The Entomopter, Neurotechnology for Biomimetic Robots* (The MIT Press, 2002). ISBN 0-262-01193-X.
- [3.40] Z. Liu, J. M. Moschetta, *The European MAV Conference*, (Sep. 2009).
- [3.41] Tennekes, H., *The Simple Science of Flight From Insects to Jumbo Jets* (revised and expanded edition), The MIT Press, Cambridge, Massachusetts, 2009.
- [3.42] C. J. Pennycuick, *The Journal of Experimental Biology.*, 150 (1990).
- [3.43] Matweb Material Property Data – Mylar - 48 Gauge (2012).
- [3.44] Homefly.com retailer. <http://www.homefly.com/products.asp?id=31>.
- [3.45] J. G. Fernandez, D. E. Ingber, *Advanced Materials*, (Jan. 24 2012).
- [3.46] Marske Aircraft Corporation, *Graphlite™ Properties* (2012).
- [3.47] Matweb Material Property Data – ASTM A228 (2012).
- [3.48] Dupont, *Technical Guide Kevlar Aramid Fiber*.
- [3.49] C. K. Hsu, J. Evans, S. Vytla, P. G. Huang, 48th AIAA ASM, Orlando, FL, (Jan 2010).
- [3.50] H. Tanaka, R. J. Wood, *Journal of Micromechanics and Microengineering*, 20, (2010).

- [3.51] T. Dargent, X. Bao, S. Grondel, G. Brun, J. Paquet, C. Soyer, E. Cattan, *Journal of Micromechanics and Microengineering*, (July 2009).
- [3.52] X. Bao, A. Bontemps, T. Vanneste, J. Paquet, S. Grondel, and E. Cattan, *International Workshop on Bio-Inspired Robots*, Nantes, France (2011).
- [3.53] United States Depart. of Agricultural - Animal and Plant Health Inspection Service - Insects and Mites (Feb 2012).
- [3.54] G. Lim, S. Shkarayev, Z. Goff, and P. Beran, *Studies of Flight Kinematics of Ornithopters*, *International MAV Conference*, Braunschweig, Germany, July 3-6, 2012.
- [3.55] H. Fischer, and W. Kutsch, *Relationships Between Body Mass, Motor Output and Flight Variables during Free Flight of Juvenile and Mature Adult Locusts, Schistocerca gregaria*, *Journal of Experimental Biology* 203, 2723–2735 (2000).
- [3.56] Riley, J. R., *Radar Observations of Individual Desert*, *Bulletin of Entomological Research*, 64, pp 19-32 (1974). doi:10.1017/S0007485300026948.
- [3.57] S. Shkarayev, G. Maniar, A. Shekhovtsov, *50th AIAA ASM*, Nashville, Tennessee, Jan. 2012.
- [3.58] R. Randall, R. Kumar, S. Shkarayev, “Bio-Inspired Design of Micro Ornithopters”, *International MAV Conference*, Braunschweig, Germany, July 2012.

4. Longitudinal Aerodynamics of Rapidly-Pitching Fixed-Wing Micro Air Vehicles

This chapter is based on results published in the paper entitled “Longitudinal Aerodynamics of Rapidly Fixed-Wing Micro Air Vehicles,” Journal of Aircraft, Vol. 49, pp. 453-471, 2012, by R. Randall, S. Shkarayev, G. Abate, and J. Babcock.

Nomenclature

\bar{c}	=	wing mean aerodynamic chord
C_L	=	wing lift coefficient, $C_L = 2L/(\rho V^2 S)$
C_D	=	wing drag coefficient , $C_D = 2D/(\rho V^2 S)$
C_m	=	wing moment coefficient, $C_m = 2M/(\rho V^2 S \cdot \bar{c})$
C_N	=	single-propeller normal-force coefficient, $C_N = (N/2)/(\rho \cdot n^2 d^4)$
C_T	=	single-propeller coefficient of thrust, $C_T = (T/2)/(\rho \cdot n^2 d^4)$
C_{T0}	=	static coefficient of thrust, $C_{T0} = (T_0/2)/(\rho \cdot n_0^2 d^4)$
d	=	propeller blade diameter
D	=	wing drag
f	=	vortex-shedding frequency
J	=	advance ratio, $J = V/(n \cdot d)$
L	=	wing lift
M	=	wing moment
M_p	=	pitching-moment induced by the propulsion system about a point along its thrust-axis directly between the two propeller discs
n	=	propeller rotation rate in revolutions per second

N	=	propulsive normal force (combined effect of both propellers), directed in the longitudinal plane normal to the propulsive axis
Re	=	Reynolds number, $Re = \rho V \cdot \bar{c} / \mu$
St	=	Strouhal Number, $St = f \cdot \bar{c} \sin \alpha / V$
T	=	thrust generated by propulsion system (combined effect of both propellers)
V	=	freestream velocity (effective wind tunnel flow speed)
α	=	angle of attack (specified as angle between wind tunnel flow direction and instantaneous root chord-line of wing)
δ_e	=	elevator deflection (positive downwards)
δ_t	=	throttle-setting varying between off (0%) and full-throttle (100%)
θ	=	pitch angle of the wing
μ	=	absolute viscosity of local air
ρ	=	local air density
Ω	=	non-dimensional pitching rate, $\Omega = \dot{\theta} \cdot \bar{c} / V$

4.1. Micro Air Vehicles with Vertical Takeoff and Landing Capabilities

The term Micro Air Vehicle (MAV) refers to aircraft that are significantly smaller than conventional aircraft. MAVs typically have a maximum linear dimension between 15 and 30 cm and can be classified according to their mode of flight: fixed-wing, rotary-wing or flapping-wing. Fixed-wing MAVs typically utilize either a single-propeller, contra-rotating propellers or counter-rotating propellers. MAVs can be remotely controlled, fully-autonomous, semi-autonomous or switchable between the three. They are often used as sensor platforms; carrying cameras, chemical sensors or anything that is sufficiently small and light. Unlike their larger cousins (UAVs), many MAVs can operate close to the ground, in cluttered environments and indoors. Some advantages of these small craft include: low visual signatures, high maneuverability and low-cost manufacturing, maintenance, and storage.

Rotary-wing MAVs have the maneuverability and low-speed flight capability necessary to be effective in restrictive operational environments, but they generally lack the range, endurance, payload capacity and dash speed of their fixed-wing cousins. Fixed-wing craft are typically incapable of either hovering or operating effectively in restrictive environments. To combine the desirable features of both classes fixed-wing vertical-takeoff-and-landing (VTOL) MAVs have been developed at the University of Arizona [4.1, 4.2] which includes the Vertigo, Mini-Vertigo, and Mini-Vertigo 2 (MV2).

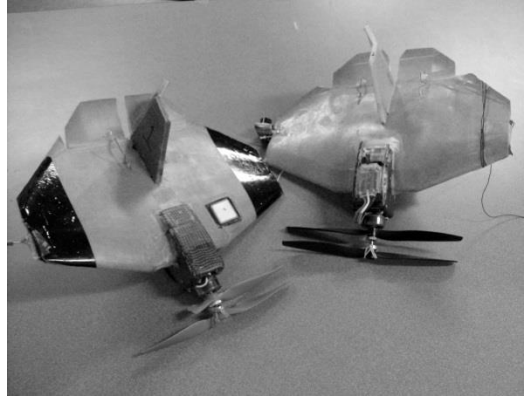


Fig. 1 Mini-Vertigo 2 MAVs

Mini-Vertigo 2 is a very capable vehicle. During horizontal flight the craft is faster and more efficient than typical rotary-wing MAVs. MV2 is capable of hovering and has a cruise speed of 15 m/s; it is also capable of fully-autonomous flight using GPS waypoint navigation. Telemetry data, live video and other information is acquired via a ground station during flight. For non-autonomous flight MV2 can be remotely piloted using a transmitter (with integrated gyros for stabilization).

The aerodynamics of fixed-wing VTOL MAVs, which utilize a Zimmerman wing and contra-rotating propellers, is complex. The flow field around such aircraft is heavily influenced by the freestream, its own tip vortices, and its propeller-induced pulsating slipstream. Craft operate at low Reynolds numbers (LRN), have low aspect ratios (LAR) and function at very high angles of attack (AOA). They are capable of rapid-pitching as they transition between flight modes. Vehicle performance during transition can be improved with data obtained in the present study, after the data is integrated into autopilot control algorithms. Also, acquired data may be helpful toward development of autonomous perching [4.3, 4.4].

Steady aerodynamics of LRN propellers has been studied by Uhlig and Selig [4.5] who compared experimental measurements with theoretical predictions of propeller performance; they found that codes based on Blade Element Momentum Theory do not provide accurate

predictions of propeller performance in the post-stall region, owing to 3D effects. Another study was conducted by OL and Zeune [4.6], which included tests of several off-the-shelf propellers. The study [4.6] found that propeller performance is sensitive to Reynolds number at low advance ratios, efficiency increases with Reynolds number and “square” props have the highest peak efficiency.

There have been several studies related to steady aerodynamics of LAR, LRN wings. One particularly comprehensive project was undertaken by Torres [4.7] who examined the effects of planform, aspect ratio and leading edge shape on wing aerodynamic coefficients. Torres found that the location of the aerodynamic center (AC) for LAR, LRN wings is not necessarily fixed at the quarter-chord (the quarter-chord of each airfoil falls on a straight-line). Data also showed that a tapered approximation to an elliptic wing is equivalent in performance to the elliptic wing itself. Another study was performed by Pelletier and Mueller [4.8] whose results demonstrated the beneficial effect of camber on LRN, LAR wings.

A few studies of steady slipstream/freestream interaction have been conducted [4.9, 4.10]. Kuhn developed a semi-empirical model for VTOL propeller-wing-flap configurations for high Reynolds numbers at low AOA [4.9]. A paper was authored by Kuhn and Draper [4.10] which explored the same configuration, but up to 90 degrees AOA. The papers quantified: augmentation of wing lift due to propeller-slipstream, the effect of lift augmentation on wing drag and AOA effects on propulsion. Hoffman [4.1] conducted a LAR, LRN study of wing aerodynamics that characterized contra-rotating propulsive-slipstream effects (the velocity profile behind propellers was also studied). A paper written by Shkarayev et al. [4.2] summarized fixed-wing VTOL MAV aerodynamics and design. It was stated that a contra-rotating propulsive

slipstream causes the laminar-to-turbulent transition point to move toward the leading edge of a wing, causing a significant increase in drag.

A study by Randall et al. [4.11] characterized the steady aerodynamics of MV2-configuration fliers and their propulsion systems. The study addressed issues associated with non-dimensional coefficients applied to VTOL MAVs, and proposed new coefficient formulations.

A lot of work has been done on pitching-and-plunging airfoils, which may offer insight into the present study. Much pitching-plunging airfoil research has been conducted for application to flapping-wing vehicles [4.12-4.14]. Oscillatory motion, rather than transitory motion, was of utmost concern. Non-dimensional numbers like reduced frequency and Strouhal number were used to characterize the flow. Computer simulations, theoretical models, and experimental results have been compared and discussed.

Transitory-pitching airfoil research was conducted by Visbal and Shang [4.15]. They varied pitch-axis location and noted a strong quantitative dependence of flow features on both pitching rate and pitch-axis location. In another paper [4.16], Visbal used the difference between a constant and a decaying exponential function of time to describe the acceleration of an airfoil to constant pitching-rate for numerical investigation. The effect of varying the period of acceleration to constant pitching-rate was found to be limited to the early stages of airfoil motion.

The objective of this study is to investigate the effect of rapid-pitching on the aerodynamics of fixed-wing VTOL MAVs utilizing a Zimmerman wing and contra-rotating propellers. Acquired data should be useful for improving autopilot performance during rapid-pitching maneuvers, including transition between flight modes.

4.2. Models and Experimental Apparatus

The experimental model consists of a wing and a propulsion system. The fixed-wing has a Zimmerman planform and uses a thin reflexed-airfoil. The propulsion system features contra-rotating motors and propellers in a tractor configuration. The model has been tested under steady conditions at different facilities: the University of Arizona (UA) low-speed wind tunnel [4.1, 4.2], the Institut Supérieur de l'Aéronautique et de l'Espace (ISAE) in France and currently the University of Florida's Research Engineering and Education Facility (REEF). Presented in Figure 2 is a picture of the model. Technical data is presented in Table 1.

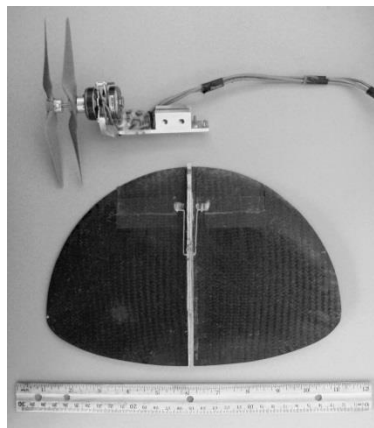


Fig. 2 Experimental Model

Table 1 Model Information

Planform Shape	Zimmerman
Wingspan	252.0 mm
Root Chord Length	168.0 mm
Mean Aerodynamic Chord	142.6 mm
Wing Area	332.5 cm ²
Aspect Ratio	1.91
Elevon Area	41.0 cm ²
Airfoil	S5010-TOP24C-REF
Contra-Rotating Motors	MP Jet AC 22/4-60D
Propellers (2)	APC 5.5 x 4.5
Wing Material	Carbon Fiber
Rib Material	Plywood
Motor Mount Material	Aluminum

The wind tunnel at REEF is an open-loop, open-section tunnel that is capable of airspeeds up to 20 m/s. Installed in the test section is a pitching-plunging mechanism to actuate model motion. The mechanism is driven by two vertically-moving DC motors with DMC controller software. The controller for the actuating motors accepts discretely prescribed motor positions at constant time-steps. The wind tunnel inlet is depicted in Figure 3 and a picture of the model mounted in test section is provided in Figure 4.



Fig. 3 REEF wind tunnel inlet

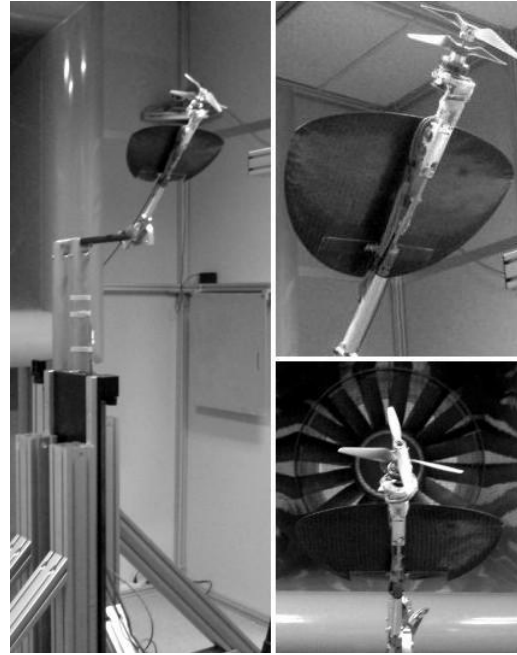


Fig. 4 Model mounted in test section

A detailed description of the experimental facility can be found in a paper by Albertani and Babcock [4.17].

Table 2 Specifications of Pitching-Plunging Mechanism

Carriage Travel Distance	0.8 m
Max Linear Motor Speed	5 m/s
Motor Position Resolution	5 μ m
Motor Continuous Force	664 N
Motor Peak Force	2970 N
Nominal Angular Test Range	60 degrees

Steady wind tunnel experimentation is generally well-understood, so procedural details are not provided. Unsteady testing is more complex and less-routinely undertaken. Therefore, procedural details will be provided for unsteady tests.

4.3. Steady Results

Propulsion system aerodynamics is of some interest. Forces on the propulsion system are studied separately from those on the wing so that results can be applied to different combinations of wings and propulsion systems. The propulsion system was powered using an off-board power supply set to 11.0 volts. Steady thrust data has been previously presented for the same propulsion system at the same voltage and throttle-settings [4.11]. Presented data included thrust variation with freestream velocity, angle of attack and throttle-setting. For the present study thrust is proportional to throttle-setting throughout the test domain [4.11]. An empirical model of thrust variation has been previously presented [4.18].

The variation of propeller rotation-rate was investigated under steady conditions, at REEF. Figure 5 shows approximately linear variation of propeller rotation rate, in the investigated AOA range, and at the experimental Reynolds number used (86K). AOA spans 20-70 degrees to cover the transition region. Throttle-setting was fixed during tests, but propeller rotation-rate and freestream velocity varied. As a result, advance ratio varies, as shown in Figure 6.

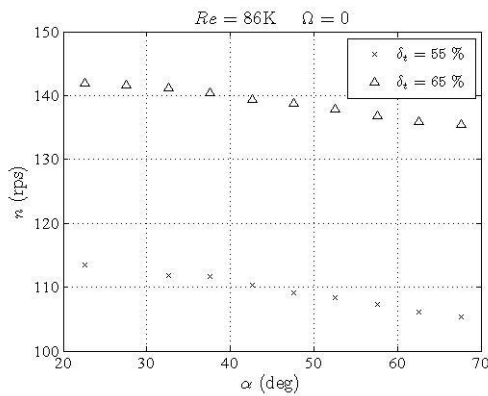


Fig. 5 Propeller rotation rate

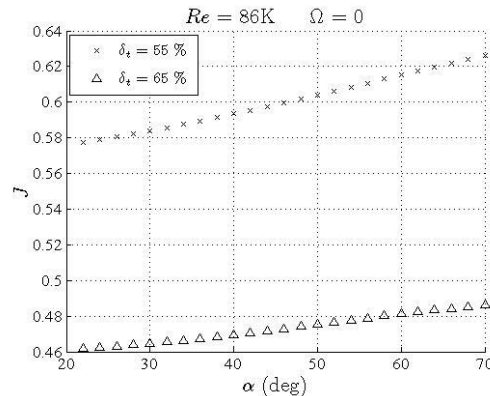


Fig. 6 Advance ratio variation

Under the experimental conditions thrust coefficient increases linearly with angle of attack, as seen in Figure 7. Throttle-setting curves begin to converge near 70 degrees and linear curve-

fitting applied to Figure 7 suggests that curves will intersect at 90 degrees. Because advance ratio is different at the different throttle-settings, such convergence suggests that thrust-coefficient may be independent of advance ratio at 90 degrees. Figure 8 indicates that propulsive normal force coefficient increases with AOA.

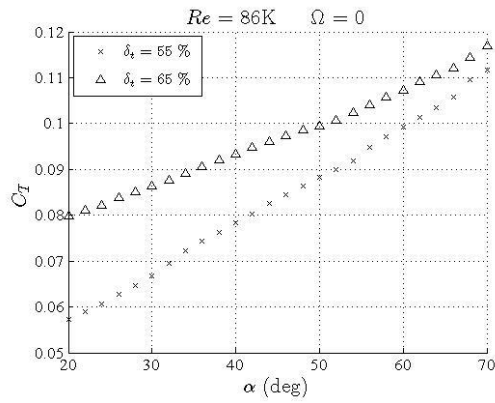


Fig. 7 Steady thrust coefficient

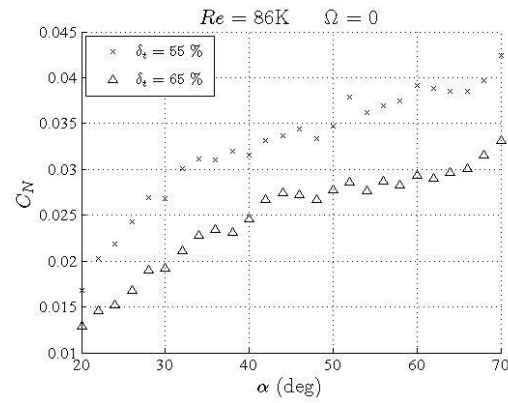


Fig. 8 Steady normal force coefficient

Figure 9 describes the steady aerodynamics of the wing. Increasing throttle-setting delays stall and increases maximum lift coefficient. As throttle-setting increases, lift and drag coefficients increase throughout the tested AOA domain. From 30-70 degrees AOA, wing aerodynamic efficiency is approximately independent of both elevator deflection and throttle-setting.

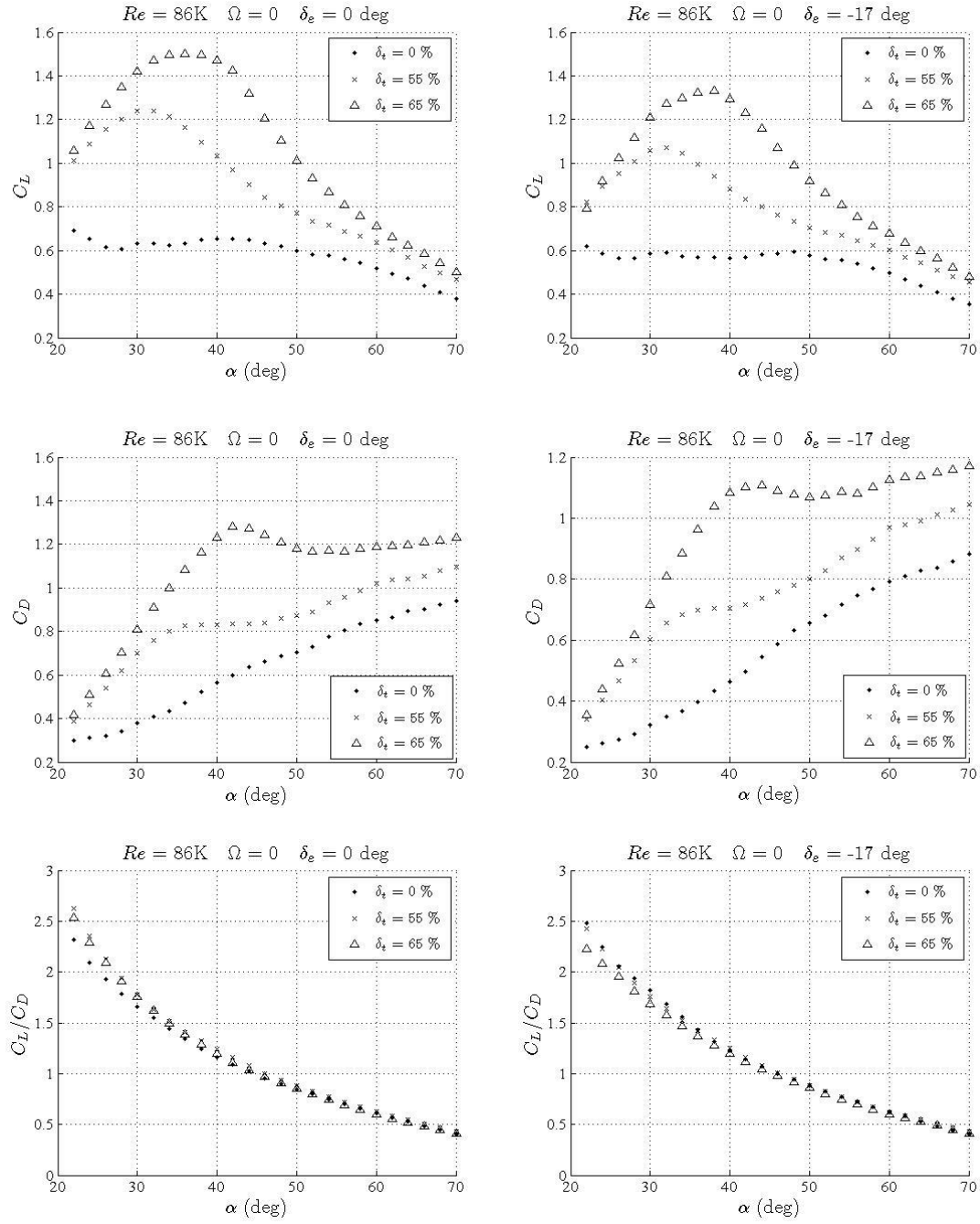


Fig. 9 Steady wing coefficient data

4.4. Unsteady Procedure and Processing

An ideal flight mode transition might be described by constant-rate pitching without gain or loss of altitude (except for short periods of angular acceleration to-and-from the constant rate). When specifying altitude a logical reference point is center-of-mass. For Mini Vertigo 2 (MV2), and similarly-designed vehicles, center of mass is extremely close to wing aerodynamic center (AC). In the present study the test subject pitches at constant rates about its AC.

Other test parameters included elevator deflection and throttle-setting. A -17 degree elevator deflection was selected based on the horizontal-to-vertical transition of MV2 in free-flight. Throttle-settings of 55% and 65% were similarly chosen. Experimental pitching rates as high as ± 2 radians per second were selected based on MV2 pitching-rate data presented in a paper by Chu et al. [4.18]. Dimensional pitching rates correspond to non-dimensional rates of $\Omega = \pm 0.031$.

Before a test matrix was fully-developed limitations of the system were considered including maximum permissible balance-loading. Sting balance loads were estimated based on expected inertial and aerodynamic forces prior to testing. Before executing final motions, different acceleration profiles were investigated using lower-rate pre-test motions. As a result of the investigation, actuating motors were accelerated at constant rates to minimize inertial stresses on the balance. Another method was employed to minimize inertial stresses and to increase system stiffness. A portion of the plywood rib running along the root-chord of the wing (Figure 2, Figure 4) was cut away to allow the connection between the aircraft and the balance to be made closer toward the aircraft's heavy motor.

Although the desired AOA range was from 0-90 degrees, the testing system was mechanically limited to a maximum angular displacement of 60 degrees. Test subject angular acceleration was

necessary to reach the desired constant pitching-rates (CPR). Afterward, test subject angular deceleration was necessary to return the test subject to rest. Acceleration/deceleration magnitude was limited by balance strength. Five degrees of angular displacement were required for acceleration and another five degrees were required for deceleration, leaving 50 degrees available for CPR motion. Accordingly, CPR tests span 20 to 70 degrees AOA, with periods of angular acceleration/deceleration occurring at lower and higher angles. Acceleration and deceleration each span 80 ms.

Another limitation was the range of allowable positions for the linear actuating motors, which controlled movement of the experimental model. This was not a true limitation in practice, because it only affected motor starting positions. Since particular *model* motions were desired, corresponding *motor* motions had to be determined. A custom MATLAB program was written for that purpose, based on system kinematics. The program utilizes a Forward-Euler numerical scheme. Figure 10 shows the height of the actuating motors, Motor A and Motor B, from their lowest allowable position (0 m) for the -2 radian per second pitching motion.

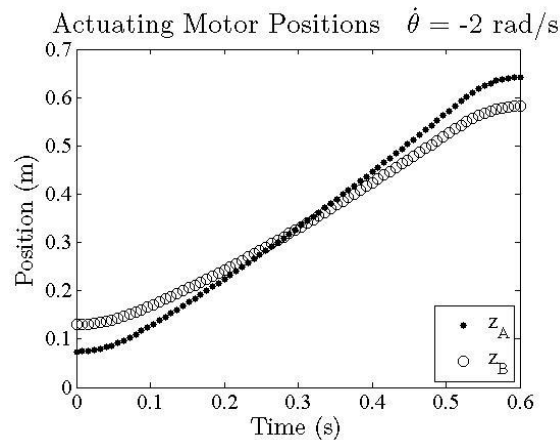


Fig. 10 Position of actuating motors vs. time for $\dot{\theta} = -2 \text{ rad/s}$

The motor motion depicted in Figure 10 involves different stages, which correspond to three stages of model motion: acceleration, CPR and deceleration. Motions were expanded to include five stages: trigger, pause, acceleration, CPR, deceleration and pause. The expanded motion is depicted in Figure 11. Data acquisition is initiated when one of the actuating motors reaches a pre-defined position. A brief initial movement was added to motor motions to trigger data acquisition from the balance. After the triggering movement, there is a one second pause-period. Similarly, there is a period without motion following deceleration. Periods of no-motion are used to verify that aerodynamic forces agree with steady values before the motion and that they approach steady values after the motion. Fully-specified motor position points are presented in Figure 11 for the -2 rad/s pitching motion. Of primary interest are the acceleration and CPR parts, so subsequent figures will omit trigger and no-motion periods.

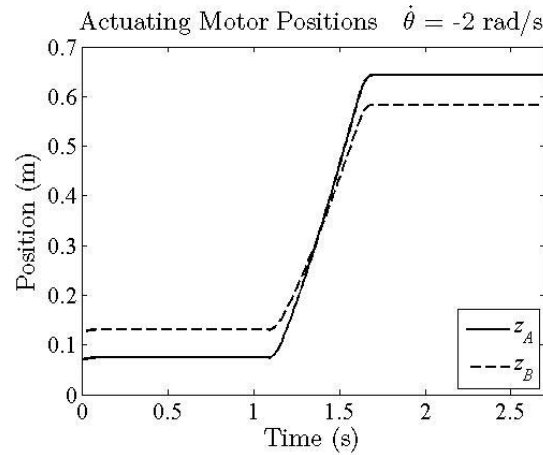


Fig. 11 Extended position of actuating motors vs. time for $\dot{\theta} = -2$ rad/s

The model-motion depicted in Figure 12 corresponds to a pitching-rate of -2 rad/s. The end of each line coming from “Tracked Point” touches the location of the wing’s AC, when the wing is present. The vertical position of the AC is constant; its horizontal position changes. Figure 13 charts wing AC location for the same motion, as predicted by a MATLAB motion-generation

file. In Figure 13, x is the horizontal position of the AC, which is positive toward the oncoming wind tunnel flow. The vertical position of the AC is denoted by z , which is positive upwards. Figures 12 and 13 are in qualitative agreement; wing AC remains at a fixed vertical position and its horizontal position changes during motions.

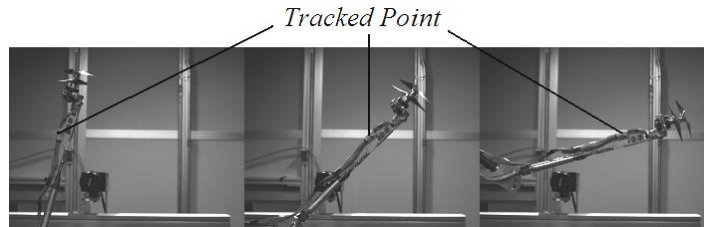


Fig. 12 Motion images for $\dot{\theta} = -2$ rad/s

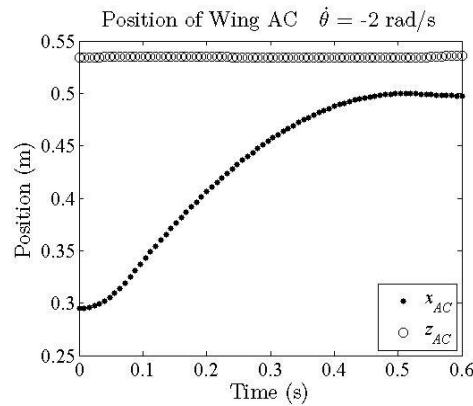


Fig. 13 Predicted AC position vs. time for $\dot{\theta} = -2$ rad/s

In pitching-plunging airfoil research, and flapping-wing research, wind tunnel flow velocity (often considered to be freestream velocity) is commonly used as a reference velocity. For consistency, wind tunnel flow velocity is used as a reference velocity in the present study with one minor adjustment. Motion of wing-AC toward the flow increases the *effective* wind tunnel flow velocity and vice versa when the AC moves away from the flow. Effective wind tunnel flow velocity, V , is used as a reference velocity and will henceforth be referred to as

freestream velocity. In this study, freestream velocity is always directed parallel to the ground. It has an average magnitude of 9.2 m/s for all tests, with maximum deviation of up to 0.43 m/s (4.7%).

To improve understanding of unsteady effects it is helpful to compare unsteady data to steady data. Steady data is often presented in terms of AOA, so it is helpful to define AOA during pitching-motions. Accordingly, AOA is defined (for our purposes) as the angle between the wind tunnel flow direction and the instantaneous root chord-line of the wing. In this study AOA is always equal to pitch angle, which follows from the definition (rates of change are also equal). Figure 14 is included to clarify AOA during pitching, where the S-shaped line is the wing's root airfoil and the dashed-line is its instantaneous root chord-line. Wind tunnel flow direction is represented by V .

Figure 15 confirms that AOA rate of change is equal to pitching-rate ($-2 \text{ rad/s} = -114.6 \text{ deg/s}$). In Figure 15, AOA starts at 70 degrees and *decreases* with time down to 20 degrees because the pitching rate is *negative*.

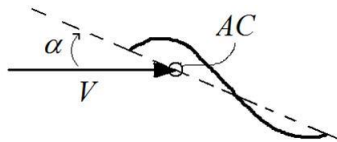


Fig. 14 Unsteady angle of attack

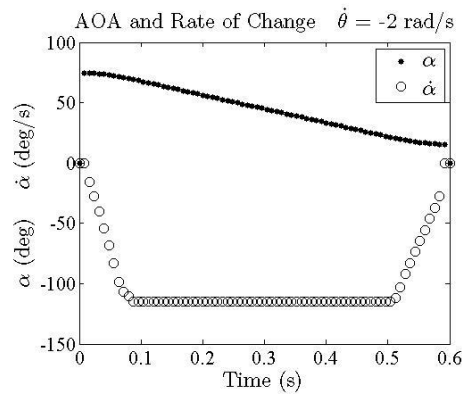


Fig. 15 Angle of attack & rate-of-change vs. time

High-speed videography was used to verify accurate production of desired motions. The position of the “Tracked Point” in Figure 16 was observed at each pitching-rate with the wind

and propulsion system turned off. If the wing were present, its AC would be coincident with the “Tracked Point”. Images were acquired at 100 Hz and compiled into videos using Windows Movie MakerTM. Videos were analyzed using software developed by Hedrick [4.19], which output AC position coordinates at each frame. For positive pitching-rates *observed* position was within a few millimeters of *desired* position, as seen in Figure 17.

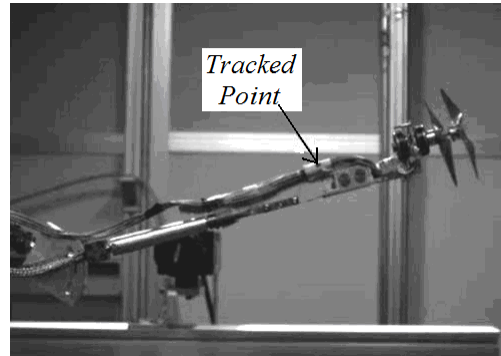


Fig. 16 Aerodynamic center point-tracking

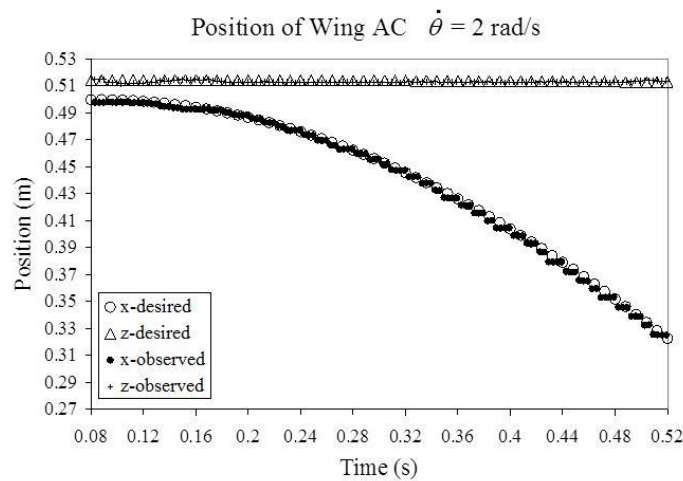


Fig. 17 Desired vs. observed position of wing AC for $\dot{\theta} = 2$ rad/s

Dynamic tests were performed according to the matrix given in Table 3. The uppermost column headings in Table 3 list the objects whose applied loads were measured by the sting balance during testing. *Wing+Propulsion+Other* tests were performed with everything shown in

Figure 4. The wing was removed for *Propulsion+Other* tests, which include everything shown in Figure 16. For *Other* tests the sting balance, propulsion-system wires and plywood rib were retained while the wing, propellers, motor and motor mount were removed. The furthest-right column in each category is broken up into cells. Each cell represents a unique testing condition described by that cell and the cells to its left.

Table 3 Unsteady test matrix

Other		Propulsion+Other			Wing+Propulsion+Other			
$\dot{\theta}$ (rad/s)	Re (K)	$\dot{\theta}$ (rad/s)	Re (K)	δ_t (%)	$\dot{\theta}$ (rad/s)	δ_e (deg)	Re (K)	δ_t (%)
-2	0	-2	0	0	-2	0	0	0
		-2	86	0	-2	0	86	0
		-2	86	55	-2	-17	0	0
		-2	86	65	-2	-17	86	0
-2	86	-2	86	55	-2	-17	86	55
		-2	86	65	-2	-17	86	65
		-1	0	0	-1	0	0	0
		-1	86	0	-1	0	86	55
-1	0	-1	86	0	-1	0	86	65
		-1	86	55	-1	-17	0	0
		-1	86	65	-1	-17	86	0
		-1	86	65	-1	-17	86	55
-1	86	-1	86	65	-1	-17	86	65
		0	0	0	0	0	0	0
		0	86	0	0	0	86	0
		0	86	55	0	-17	0	0
0	0	0	86	55	0	-17	86	0
		0	86	65	0	-17	86	55
		0	86	65	0	-17	86	65
		0	86	65	0	-17	86	65
0	86	0	86	65	0	-17	86	65
		1	0	0	1	0	0	0
		1	86	0	1	0	86	0
		1	86	55	1	-17	0	0
1	0	1	86	55	1	-17	86	0
		1	86	65	1	-17	86	55
		1	86	65	1	-17	86	65
		1	86	65	1	-17	86	65
1	86	1	86	65	1	-17	86	65
		2	0	0	2	0	0	0
		2	86	0	2	0	86	0
		2	86	0	2	0	86	55
2	0	2	86	0	2	0	86	65
		2	86	55	2	-17	0	0
		2	86	55	2	-17	86	0
		2	86	55	2	-17	86	0

2	86	65	2	-17	86	55
			2	-17	86	65

Aerodynamic loads on the wing itself are isolated. When a wind-on test is run the signal being read from the balance includes aerodynamic forces, and also inertial forces because the system is accelerated through its desired motion. An inertial tare is performed for each motion to isolate aerodynamic forces. Inertial tares correspond to zero Reynolds number and zero-percent throttle-setting tests shown in Table 3. Because inertial tares are not performed in a vacuum there are aerodynamic influences present. For inertial tares, aerodynamic influences are disregarded because no point on the wing attains a groundspeed greater than 0.85 m/s during any part of any motion.

There is one additional consideration when isolating aerodynamic forces. Propellers and motors do not rotate during inertial tares, but they do rotate during most tests. As the model pitches its rotating propellers and motors also pitch, causing the propulsive axis of rotation to tilt. Consequently, there appears to be an inertial test-tare difference that Equation 1 does not account for. In reality, forces related to spinning-propeller rotational inertia are minor due to contra-rotation. Negligible forces remain because there is a slight difference in moment-arm from the wing's AC to each motor and propeller.

$$F_{aero} = F - F_{inertial} \quad (1)$$

F_{aero} is *aerodynamic* force exerted during a wind-on test, F is total force measured during a wind-on test and $F_{inertial}$ is total force measured during an inertial tare.

Equation 2 describes how aerodynamic forces on the propulsion system (motor, motor mount and propellers) are isolated from aerodynamic forces on “Other” (the wire, plywood rib and sting

balance). Aerodynamic force terms on the right-hand side of Equation 2 are calculated according to Equation 1. See Table 3 and its preceding discussion for details.

$$(F_{prop})_{aero} = (F_{prop+other})_{aero} - (F_{other})_{aero} \quad (2)$$

$(F_{prop})_{aero}$ is aerodynamic force exerted on the propulsion system, $(F_{prop+other})_{aero}$ is aerodynamic force exerted on “Propulsion+Other”, and $(F_{other})_{aero}$ is the aerodynamic force exerted on “Other”.

Aerodynamic forces on the wing are determined by Equation 3. The difference in moment-arm from the wing’s AC to each motor and propeller is inconsequential because test-tare differences are present in both terms on the right-hand side of Equation 3 and cancel. Potential interference effects are neglected, including the influence of the wing on propulsion system aerodynamics. Term definitions follow from Equation 2 discussion.

$$(F_{wing})_{aero} = (F_{wing+prop+other})_{aero} - (F_{prop+other})_{aero} \quad (3)$$

Generally speaking, static tests record data from a balance at a high-frequency for several seconds at each model position. Consequently, a large set of data is obtained for each steady test at each position. The data may be averaged and standard deviations can be reliably estimated. In dynamic tests a model is only at a particular position for an instant in time, so each motion must be repeated multiple times to gather a *set* of data at each position. To determine how many times a test should be repeated to obtain a reliable average, one motion was run 30 times and its data was analyzed. The number of runs used to average the data was varied: the first run only, the first 5 runs, the first 10 runs, the first 15 runs.

4.5. Unsteady results

This study investigates aerodynamic effects of constant-rate pitching. The aerodynamic center of a wing is chosen as the point of rotation. Unsteady data is compared against steady data via AOA, which is specified as the angle between freestream velocity and wing instantaneous root chord (as depicted in Figure 14). If desired, coefficient time-dependency may be extrapolated from presented data [4.6].

The effect of pitching-rate on aerodynamic coefficients depends on more than just advance ratio, AOA, and Reynolds number. Plots are also distinguished by non-dimensional pitching rate, Ω (text omitted). Non-dimensional pitching rate is the inverse of the Rossby number and has been applied to pure-pitching airfoil research by Visbal and Shang [4.22]. Table 7 relates non-dimensional pitching-rate, dimensional pitching-rate and AOA rate-of-change using row-equivalency. Because there is freestream velocity variation during pitching maneuvers, mean values with less than 5% deviation from the mean are presented for Ω (worst-case velocity variation depicted in Figure 19).

Table 7 Relationship between pitching parameters

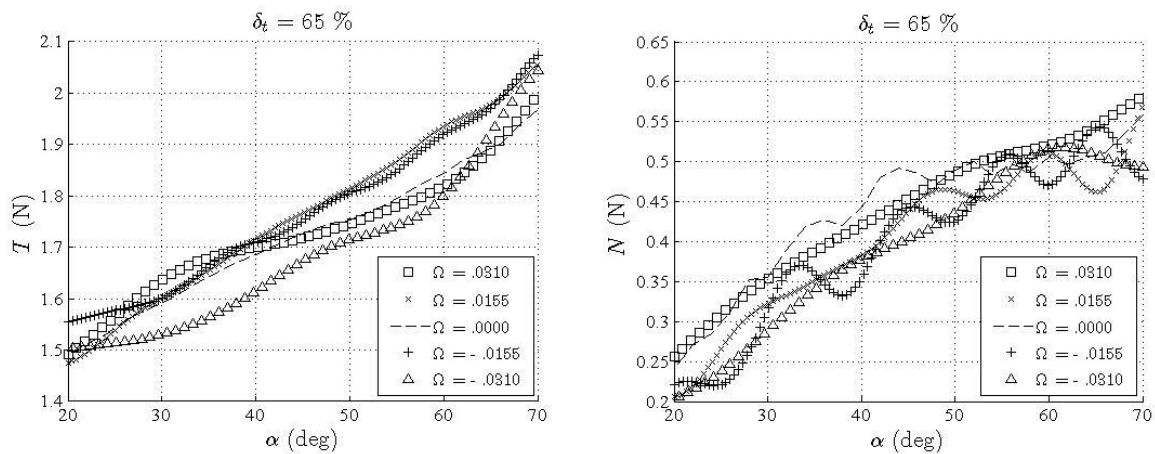
Ω	$\dot{\theta}$ (rad/s)	$\dot{\alpha}$ (rad/s)
-.0310	-2	-2
-.0155	-1	-1
.0000	0	0
.0155	1	1
.0310	2	2

Table 8 relates mean values for advance ratio, throttle-setting and propeller rotation-rate. Propeller rotation-rate varies with both AOA and freestream velocity, and may vary with pitching-rate. For the no-pitching case, propeller rotation rate does not deviate more than 5% from its mean value at a particular throttle-setting (see Figure 5).

Table 8 Relationship between propulsive parameters

J	δ_i (%)	n (rps)
<i>undef</i>	0	0
0.60	55	110
0.47	65	139

Propulsive motors did not include encoders. During dynamic tests propeller rotation-rates were not experimentally determined. Approximation of unsteady propeller rotation-rates by steady ones may be reasonable as unsteady effects on propulsive forces and moments can be reasonably neglected for the autopilot design purposes (Figures 18 and 19). Nevertheless, unsteady propulsive data is presented in dimensional form. Neglecting insufficiently-damped oscillation for power-on conditions thrust was within 10% of its steady value throughout the testing domain and propulsion-system normal-force was within 0.1 N of its steady value. Oscillations are observed in the normal force data (Figure 18). The source of the oscillations has not been determined, but a future study may shed light on this experimental result.

**Fig. 18 Propulsive forces vs. α itemized by Ω for $\delta_i = 65\%$, $V = 9.2$ m/s**

Because the propulsion system and wing are studied separately, propulsive moment is defined in terms of a point fixed to the propulsion system. The point is defined, somewhat arbitrarily, as being located on the thrust-axis directly between the propeller discs. Unfortunately, propulsive moment was not determined for zero pitching-rate due to a mis-measurement of AC position for the static setup. For now, it is assumed that the steady propulsive moment curve lies between the curves for $\Omega = .0155$ and $\Omega = -.0155$. The closeness of the curves in Figure 19 suggests that propulsive moment is not sensitive to pitching-rate.

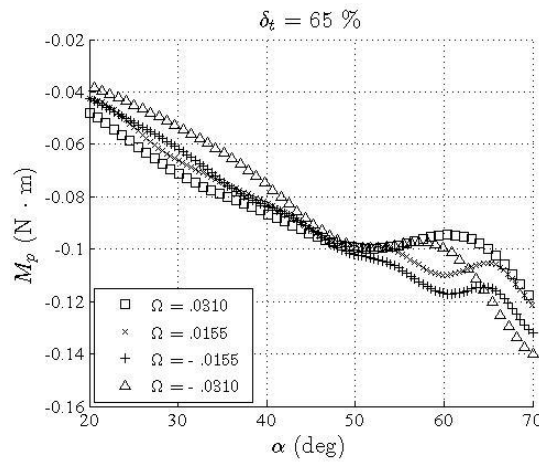


Fig. 19 Propulsive moment vs. α itemized by Ω for $\delta_t = 65\%$, $V = 9.2$ m/s

4.5.1. Wing Lift and Drag Coefficients

Observations can be made from Figure 20. Higher throttle-settings lead to greater stall delay regardless of pitching-rate (which is consistent with Figure 9). For positive pitching-rates, stall is delayed and higher maximum lift coefficients are obtained, while the opposite is true for negative pitching-rates. As Ω decreases in magnitude, so too does its relative effect. It should be noted that in subplots (1,1) and (1,2) the slipstream is absent, but the propulsion system is present. The stationary propulsion system spoils flow over the leading edge of the wing, which is expected to significantly affect wing aerodynamics.

Detailed examination of individual curves can lead to additional insight. Two curves are conspicuously absent: $\Omega = 0.0310$ in subplot (2,1) and $\Omega = 0.0310$ in subplot (3,1). The curves were omitted due to considerable lift coefficient disagreement between QS and ST values at 75 degrees AOA (Table 6). For the cases presented in subplots (2,1) and (3,1) one may observe that in Table 6 at 75 degrees AOA there is significant disagreement between QS and ST lift data for the $\Omega = 0.0310$ curve. Those curves are, therefore, not presented in Figure 31.

Pitching-rate curves noticeably oscillate in subplots (1,1) (1,2) (2,1) and (2,2), especially at high AOA. Oscillations may be due to inadequate filtering, vortex-shedding or some other phenomenon. More conclusive results are expected from a future study.

As the slipstream is strengthened, oscillation amplitudes reduce, as seen in subplots (3,1) and (3,2). If minor data oscillation is neglected, it can be concluded that higher pitching-rate generally results in higher lift coefficient throughout the tested AOA domain while lower pitching rate generally results in lower lift coefficients.

The variation of lift coefficient with pitching-rate is extremely important. The relationship between lift coefficient and pitching-rate in subplots (3,1) and (3,2) seems as if it could be modeled with relative ease using polynomial curve-fitting. Interestingly, those two subplots are the ones that correspond to the strongest slipstream setting. It would seem that rapid-pitching lift-behavior is quite regular when the throttle-setting is high. Fortunately, throttle-setting is always high during real-world transition. Because subplot (3,2) features both a high throttle-setting and a negative elevator deflection it most accurately describes a real-world horizontal-to-vertical transition.

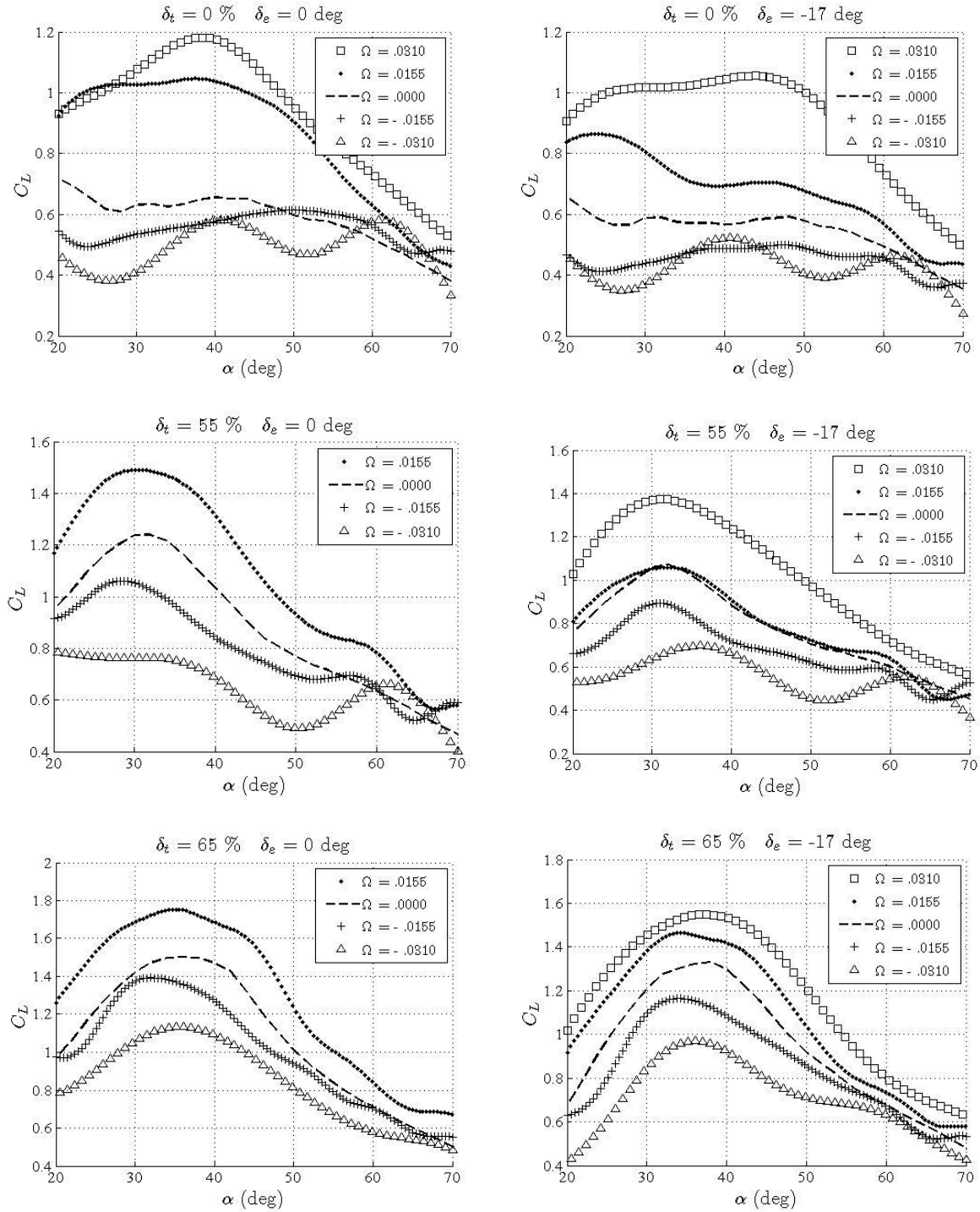


Fig. 20 Wing lift coefficient versus α itemized by Ω δ_t and δ_e for $Re = 86K$

Non-dimensional pitching rate is varied in Figure 32, which shows drag coefficient results for the wing. Comparisons in Table 6 suggest that drag data was accurately obtained for all cases.

For subplots (1,1) and (1,2) stationary propellers spoil airflow over the wing, producing results that may be quite different from those obtained for the wing without the propulsion system. It would seem (based on Figure 32) that a model of drag coefficient could be developed with relative ease when the slipstream is present. Steady and unsteady aerodynamic modeling that considers alternative non-dimensional coefficient definitions will be explored in a future study.

Higher pitching-rate generally results in higher drag over the tested AOA-domain. Drag seems to increase with both pitching-rate and throttle-setting. Subplots (3,1) and (3,2) correspond to a strong slipstream. In those subplots, positive pitching-rate curves have local maximums between 40 and 50 degrees AOA and local maximums occur at higher AOA for higher pitching-rates (positive). Comparison of local drag maximums (Figure 21) and global lift maximums (Figure 20) leads to the observation that local drag maximum occurs at slightly higher AOA than global lift maximum.

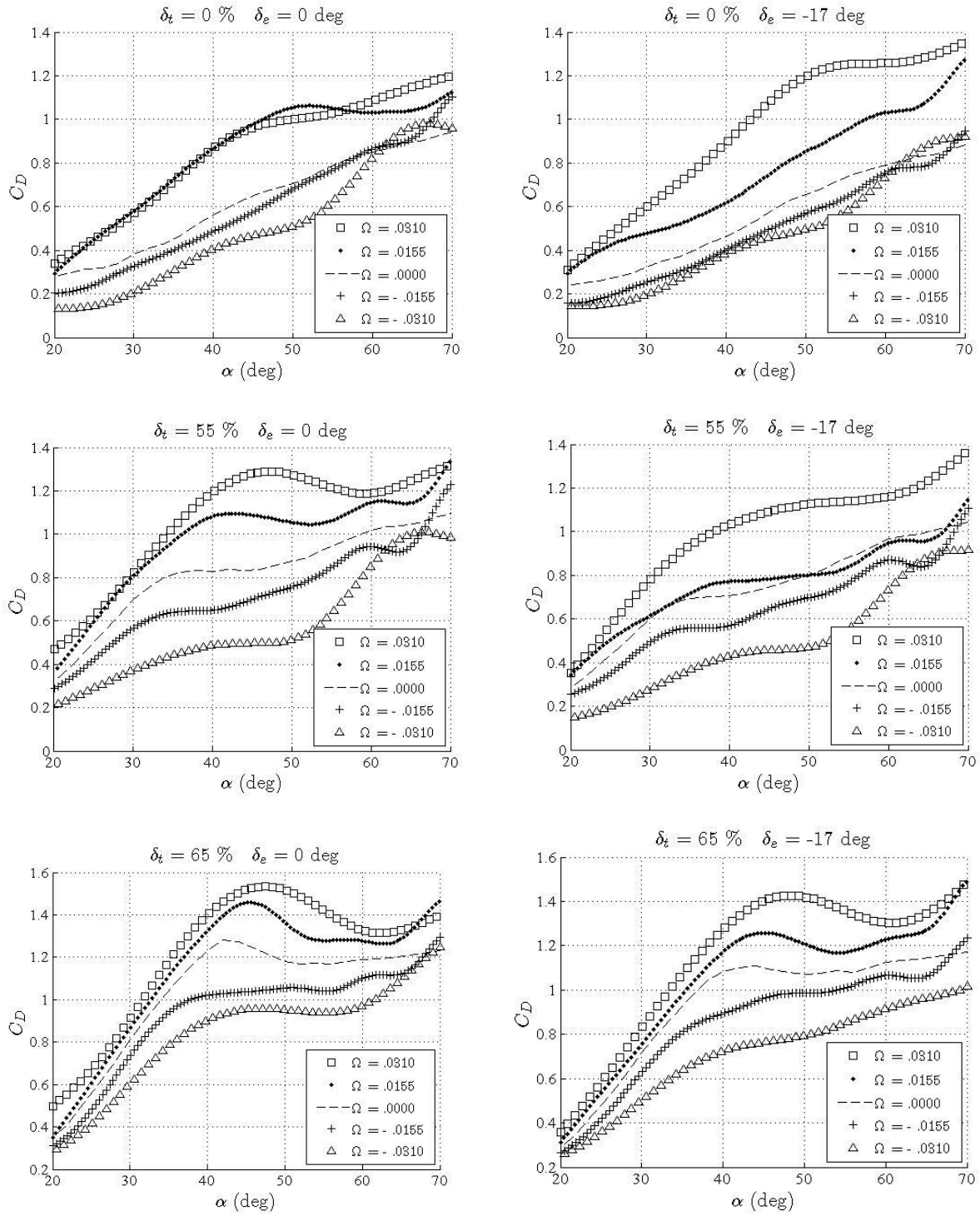


Fig. 21 Wing drag coefficient versus α itemized by Ω δ_t and δ_e for $Re = 86K$

Wing aerodynamic efficiency, C_L/C_D , may be used to establish useful relationships between lift and drag coefficients. Such relationships may be used, for instance, to describe drag as a function of lift. Figure 22 presents aerodynamic efficiency data for different non-dimensional pitching rates. Pitching-rate curves converge for AOA greater than 30 degrees, with one exception: $\Omega = -0.0310$ in subplot (2,2). The exception may be erroneous. In the 30-70 degree AOA region, for $Re = 86K$, efficiency is approximately independent of pitching-rate, throttle-setting and elevator deflection. Efficiency curves diverge in the 20-30 degree AOA region, which is most apparent in subplot (3,2), where positive pitching clearly increases efficiency. $\Omega = 0.0310$ curves in subplots (2,1) and (3,1) are not presented due to lift inaccuracy suggested by Table 6. Efficiency convergence over the specified AOA range will be further investigated in a future study.

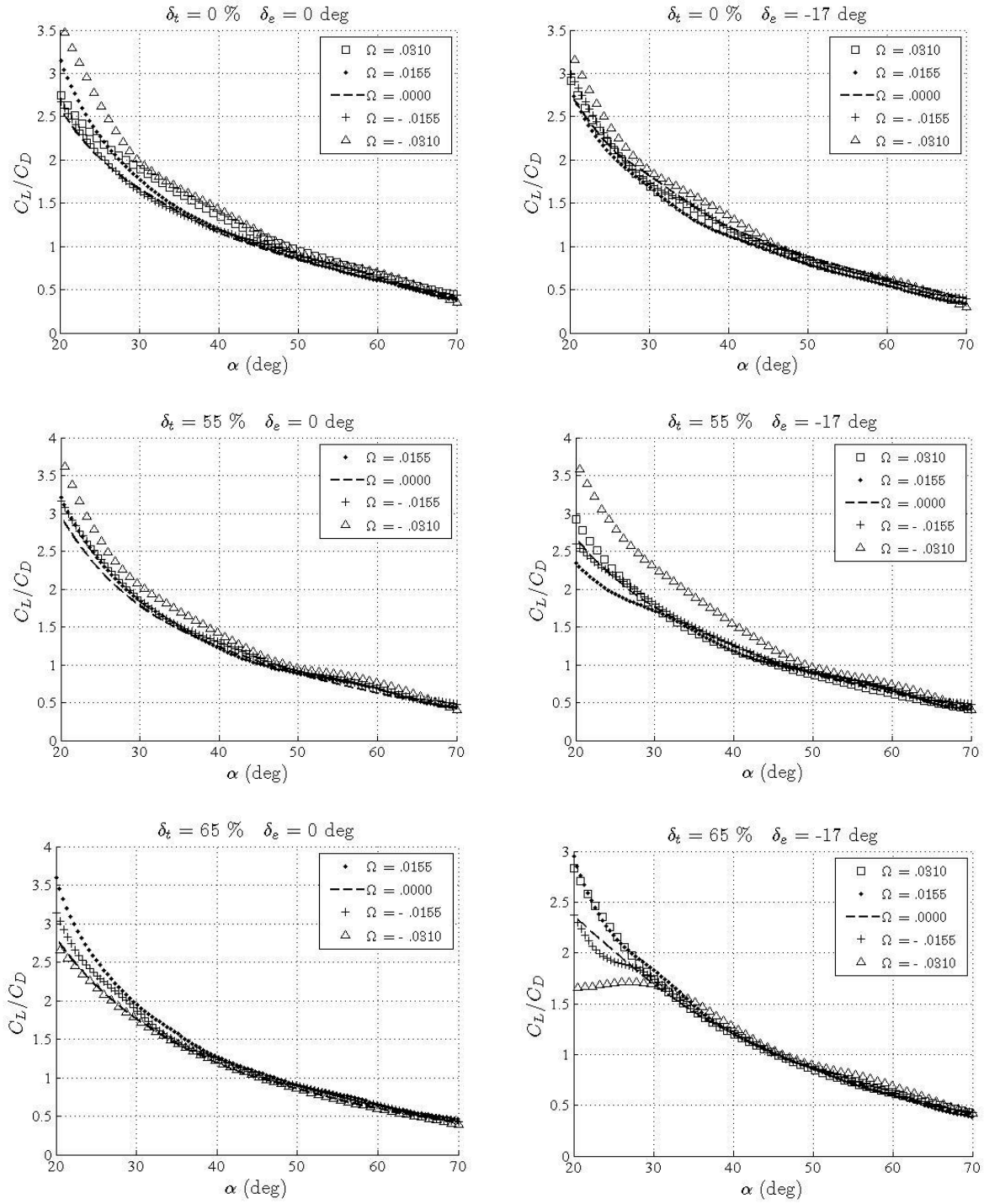


Fig. 22 Wing aerodynamic efficiency versus α itemized by Ω , δ_t and δ_e for $Re = 86K$

4.5.2. Wing Moment Coefficients

Figure 23 presents moment coefficient data about the AC of the test subject's wing. Unsteady curve outliers are not presented, and zero pitching-rate moment data were not accurately obtained, due to mis-measurement of AC position for the static setup. Although zero pitching-rate curves are not shown, it may be reasonable to assume that zero-rate curves lie between positive and negative pitching-rate curves. With that assumption, additional observations may be made. The most complete data is presented in subplot (2,1), where steady moment can be expected to lie between $\Omega = -0.0155$ and $\Omega = 0.0155$. Negative elevator deflection increases moment coefficient (nose-up) throughout the tested AOA domain. Figure 23 infers that the test subject's wing could be effectively used in a free-flying model.

Static longitudinal stability for an aircraft requires that:

- (a) pitch-stiffness be positive (negative change in moment with AOA about vehicle CG), and
- (b) pitching-moment, about vehicle CG, be balanced (equal to zero).

Aircraft-CG is nearly coincident with wing-AC for many fixed-wing VTOL MAV designs. For many designs, the weight of an aircraft does not induce significant moment about its AC, which is presently assumed for discussion. The experimental AOA domain covers near-stall through post-stall. Regardless of pitching rate, throttle-setting or elevator deflection, REEF experimental data shows that wing moment generally decreases as AOA increases with a few narrow regions of exception that arise from oscillation of undetermined cause. Positive-stiffness is generally achieved throughout the domain, ignoring aerodynamic forces on other components as well as narrow regions of exception.

Subplot (3,1) suggests balanced pitch-stable flight at approximately 20 degrees AOA and subplots (2,2) and (3,2) suggest pitch-stable flight at approximately 25 and 28 degrees,

respectively. When the wing alone is considered balanced flight is not achievable beyond 28 degrees AOA for the presented conditions, as freestream velocity is relatively high (9.2 m/s). Neglecting the potentially de-stabilizing influences of other aircraft parts, a free-flight aircraft with a flying-wing design can successfully utilize the tested wing.

Unsteady aerodynamics is also considered. For a constant-altitude case of vehicle flight both pitching-rate and AOA rate-of-change are equal. Over the tested domain, the change in moment coefficient with pitching-rate is generally negative. Therefore, more rapid nose-up pitching generally results in greater loss of nose-up moment, and vice-versa for negative pitching. It follows that, in the stall and post-stall region, irrespective of angle of attack, pitching is generally aerodynamically resisted.

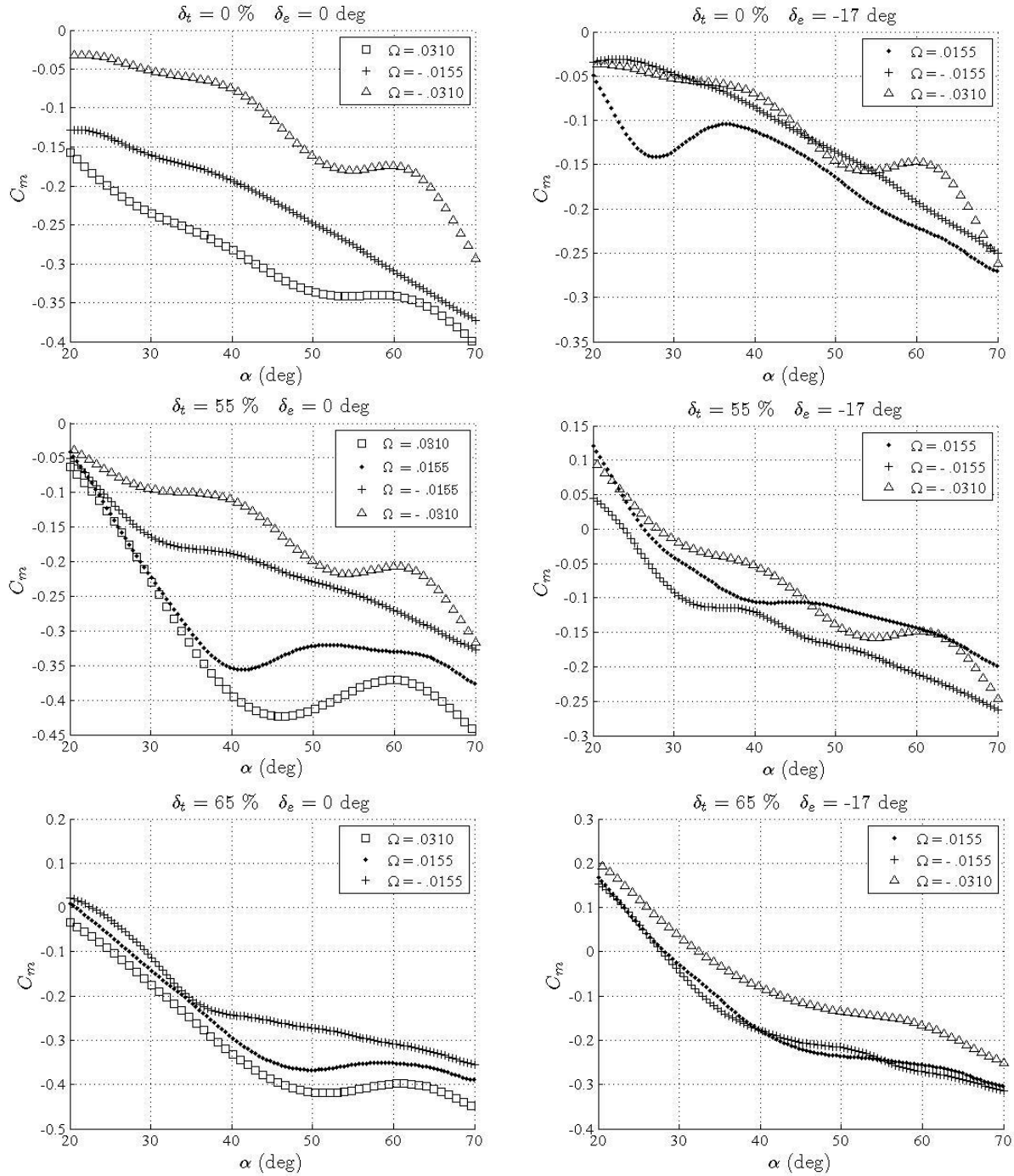


Fig. 23 Wing moment coefficient versus α itemized by Ω , δ_t and δ_e for $Re = 86K$

4.6. Summary and References to Chapter 4

Conclusions related to the steady aerodynamics of fixed-wing VTOL MAVs, with a Zimmerman wing and contra-rotating propellers, have been drawn from presented data. At $Re = 86K$, with an AOA range of 20-70 degrees, thrust coefficient increases linearly with angle of attack, and normal force coefficient increases nonlinearly. Increasing throttle-setting delays stall and increases maximum lift coefficient. As throttle-setting increases, lift and drag coefficients increase throughout the tested AOA domain. Efficiency curves converge in the stall region (around 30 degrees AOA) and remained converged thereafter, up to at least 70 degrees.

Conclusions related to rapid-pitching aerodynamics were also drawn. Nose-up pitching delays stall and increases maximum lift coefficient, while nose-down pitching hastens stall and reduces maximum lift coefficient. The relationship between lift and pitching-rate seems simpler to empirical model when the slipstream is present. Generally, positive pitching seems to increase lift coefficient throughout the transition maneuver, while negative pitching reduces it. Both stall and lift-coefficient are affected by pitching regardless of throttle-setting or elevator deflection, but pitching effects are most salient when the throttle-setting is low (weak slipstream) and the pitching-rate is high (rapid-pitching). The slipstream also seems to simplify empirical aerodynamic modeling for drag curves. It can be generally stated that higher pitching-rate (positive) results in higher drag over the tested domain. The response of lift and drag to rapid-pitching produces very interesting wing efficiency behavior. Rapid-pitching efficiency curves converge on steady efficiency curves near 30 degrees AOA. From 30-70 degrees (at $Re = 86K$) efficiency is virtually independent of pitching-rate, throttle-setting and elevator deflection. At lower AOA (near 20 degrees) efficiency curves diverge.

Propulsion system aerodynamics are not sensitive to pitching-rate. Neglecting oscillation, under power-on conditions thrust was within 10% of its steady value throughout the test domain and propeller normal force was within 0.1 N. Propulsive moment was also little-affected by pitching.

References

- [4.1] Hoffman, C., “Design, Construction, and Study of Flight Dynamics of Fixed-Wing MAV with Hovering Capabilities”, Diploma Thesis, 2008.
- [4.2] Shkarayev, S., Moschetta, J.-M., and Bataille, B., “Aerodynamic Design of Micro Air Vehicle for Vertical Flight, *J. Aircraft*”, 45, pp. 1715-1724, 2008.
- [4.3] Cory, R., Tedrake, R., “Experiments in Fixed-Wing UAV Perching,” AIAA Guidance Navigation and Control Conference, Honolulu, Hawaii, August 18-21, 2008, AIAA-2008-7256.
- [4.4] Wickenheiser, A., Garcia, E., “Longitudinal Dynamics of a Perching Aircraft,” *Journal of Aircraft*, Vol. 43, No. 5, September-October 2006.
- [4.5] Uhlig, D., and Selig, M., “Post Stall Behavior at Low Reynolds Numbers”, 46th AIAA Aerospace Sciences Meeting and Exhibit, 2008-407.
- [4.6] OL, M., Zeune, C., “Analytical-Experimental Comparison for Small Electric Unmanned Air Vehicle Propellers,” 26th AIAA Applied Aerodynamics Conference, 18-21 August 2008, Honolulu, Hawaii, AIAA 2008-7345.
- [4.7] Torres, G. E., “Aerodynamics of Low Aspect Ratio Wings at Low Reynolds Numbers With Applications to Micro Air Vehicle Design,” Ph.D. Dissertation, Department of Aerospace and Mechanical Engineering, University of Notre Dame, South Bend, Indiana, 2002.

- [4.8] Pellettier, A., Mueller, T. "Low Reynolds Number Aerodynamics of Low-Aspect Ratio, Thin/Flat/Cambered-Plate Wings," *Journal of Aircraft*, Vol. 37, No. 5, pp 825-832, 2000.
- [4.9] Kuhn, R., "Semi-Empirical Procedure For Estimating Lift and Drag Characteristics of Propeller-Wing-Flap Configurations for Vertical and Short-Take-Off-and-Landing Airplanes", NASA MEMO 1-16-59L, Feb. 1959.
- [4.10] Kuhn, R., Draper, J., "Investigation of the Aerodynamic Characteristics of a Model Wing-Propeller Combination and of the Wing and Propeller Separately at Angles of Attack up to 90° ", NASA MEMO 1-16-59L, Feb. 1959.
- [4.11] Randall, R., Hoffman, C., Shkarayev, S., "Longitudinal Aerodynamics of a Vertical Takeoff and Landing Micro Air Vehicle," *Journal of Aircraft*, Vol. 48, No. 1, Jan - Feb 2011.
- [4.12] Kang, C., Baik, Y., "Fluid Dynamics of Pitching and Plunging Airfoils of Reynolds Number between 1×10^4 and 6×10^6 ," 47th AIAA Aerospace Sciences Meeting, 5-8 January 2008, Orlando, Florida, AIAA 2009-563.
- [4.13] Lian, Y., OL, M., "Comparative Study of Pitch-Plunge Airfoil Aerodynamics at Transitional Reynolds Number," 46th AIAA Aerospace Sciences Meeting, 7-10 January 2008, Reno, Nevada, AIAA 2009-652.
- [4.14] McGowan, G., Gopalarathnam, A., "Analytical, Computational, and Experimental Investigations of Equivalence Between Pitch and Plunge Motions for Airfoils at Low Reynolds Numbers," 47th AIAA Aerospace Sciences Meeting, 5-8 January 2009, Orlando, Florida, AIAA 2009-535.
- [4.15] Visbal, M., and Shang, J.S., "Investigation of the Flow Structure Around a Rapidly Pitching Airfoil," *AIAA J.*, Vol 27, No.8, 1989, pp. 1044-1051

- [4.16] Visbal, M., "Evaluation of An Implicit Navier-Stokes Solver for some Unsteady Separated Flows," AIAA Paper 86-1053, 1986
- [4.17] Albertani, R., Babcock, J., "Analysis of Wind Tunnel Unsteady Aerodynamic Data of Flexible Micro Air Vehicle Wings," 26th AIAA Applied Aerodynamics Conference, 18-21 August 2008, Honolulu, Hawaii, AIAA 2008-6249.
- [4.18] D. Chu, J. Sprinkle, R. Randall, and S. Shkarayev, "Automatic Control of VTOL Micro Air Vehicle During Transition Maneuver," *AIAA Guidance, Navigation and Control Conference*, Chicago, Illinois, August 10-13, 2009, AIAA 2009-5875.
- [4.19] Hedrick, T., "Software techniques for two- and three-dimensional kinematic measurements of biological and biomimetic systems", IOP Publishing, 1 July 2008.
- [4.20] Lam, K., Wei, C., "Numerical Simulation of Vortex Shedding from an Inclined Flat Plate," *Engineering Applications of Computational Fluid Mechanics*, Vol. 4, No. 4, pp. 569-579, (2010)
- [4.21] Hambley, Allan. Electrical Engineering Principles and Applications (third edition). Pearson Education Inc. 2005
- [4.22] Visbal, M., Shang, J., "Numerical Investigation of the Flow Structure around a Rapidly Pitching Airfoil," *AIAA Guidance, Navigation and Control Conference*, Chicago, Illinois, August 10-13, 2009, AIAA 2009-5875.